CONVECTIVE INTRACELLULAR MACROMOLECULE DELIVERY FOR CELL ENGINEERING APPLICATIONS

A Dissertation
Presented to
The Academic Faculty

by

Anna Liu

In Partial Fulfillment
of the Requirements for the Degree
Doctor of Philosophy in
Bioengineering

School of Biomedical Engineering
Georgia Institute of Technology
May 2020

CONVECTIVE INTRACELLULAR MACROMOLECULE DELIVERY FOR CELL ENGINEERING APPLICATIONS

Approved by:

Dr. Todd Sulchek, Advisor
School of Mechanical Engineering
Georgia Institute of Technology

Dr. Krishnendu Roy, Co-Advisor
School of Biomedical Engineering
Georgia Institute of Technology

Dr. Edmund K. Waller
Department of Hematology and Oncology
Emory University School of Medicine

Dr. Alexander Alexeev
School of Mechanical Engineering
Georgia Institute of Technology

Dr. Mark Prausnitz
School of Chemical & Biomolecular
Engineering
Georgia Institute of Technology

Date Approved: [March 13, 2020]

I dedicate my dissertation to the memory of my mother, Tracy Wu, and to my family. My mother spent her life working and sacrificing to help her children succeed. It was always her dream for me to earn my PhD. My brother Gary, sister Janet, and father Kefeng were always happy to listen and lend advice. My fiancé Derek was my constant support through all the highs and lows of graduate school.

ACKNOWLEDGEMENTS

TABLE OF CONTENTS

LIST OF FIGURES

LIST OF TABLES

LIST OF SYMBOLS AND ABBREVIATIONS

VECT	Volume exchange for convective transfer
AFM	Atomic force microscopy
μ	Dynamic viscosity
kDa, MDa	Kilodaltons, Megadaltons
CAR	Chimeric antigen receptor
TCR	T-cell receptor
TRAC	T-cell receptor alpha constant
CD5	Cluster of differentiation 5
Er	Ericksen number
T_c	Cell compression time
T_v	Cell viscous time constant
E	Young's Modulus
ρ	Density
EP	Electroporation
ROI	Return on input
PDMS	Polydimethylsiloxane

SUMMARY

Efficient intracellular delivery of target macromolecules remains a major obstacle in cell engineering, cell labeling, and other biomedical applications. Current standard methods of intracellular delivery, such as viral transduction and electroporation, do not meet the growing needs in the cell engineering field for cost-effective, scalable, and efficient delivery that maintains cell viability. This thesis work has discovered the cell biophysical phenomenon of convective intracellular macromolecule delivery using mechanically-induced, transient cell volume exchange. Ultrafast microfluidic cell compressions (<1 ms) are used to cause brief, deformation-induced cell volume loss followed by volume recovery through uptake of extracellular fluid. Macromolecules suspended in the surrounding fluid enter the cell on convective fluid currents. Convective delivery is shown to bypass endosomal transport and is capable of achieving high intracellular delivery for a broad range of molecule types and sizes. Cell volume exchange is shown to be dependent on strain rate, magnitude of compression, and cell physical properties. The results of this thesis have informed the design and optimization of a high-throughput microfluidic technology capable of efficiently delivering a wide variety of macromolecule payloads to various cell types while maintaining viability and proliferation. We harness this cell volume exchange behavior for convective intracellular delivery of large macromolecules of interest, including plasmids (>2 MDa) and particles (>30 nm), while maintaining high cell viability (>95%). Successful experiments in CRISPR-Cas9 gene editing and intracellular gene expression analysis demonstrate potential to overcome the most prohibitive challenges in intracellular delivery for cell engineering.

CHAPTER 1.   INTRODUCTION AND BACKGROUND

1.1   Overview of Cell Deformation Mechanics

Cells respond to mechanical forces by undergoing deformation behavior that is similar to that of a viscoelastic solid. Studies of the deformation of various cell types have demonstrated that cell mechanical behavior can be characterized by both elastic and viscous behavior, and that cells are able to change and recover shape in response to mechanical deformations [1-9].

1.1.1   Regimes of Cell Deformation Behavior

Cell deformation behavior has been characterized by micropipette aspiration, rheometers, and atomic force microscopy (AFM). These studies have shown that the viscoelastic mechanical response of cells to deformations depends on the time scale of deformation onset. At slower deformation onset time scales (>0.01 s), cells have been observed to have elastic behavior governed by soft-glass rheology dynamics [1-5]. In soft-glass rheology dynamics, cells undergo gradual deformation that is not dependent on deformation time scale [1,3,4]. At faster deformation onset time scales (<0.01 s), cells demonstrate viscoelastic behavior in which apparent cell modulus increases with a faster deformation time scale. This regime of cell mechanical behavior appears to be governed by actin network rheology (Figure 1.1) [2,5,6]. Therefore, the time scale at which cells transition from an undeformed state to a fully deformed state affects the biomechanical behavior that governs the cell deformation response. With slower deformation, the cell

follows soft-glass rheology behavior. During faster deformations, the cell behaves as a viscoelastic material.
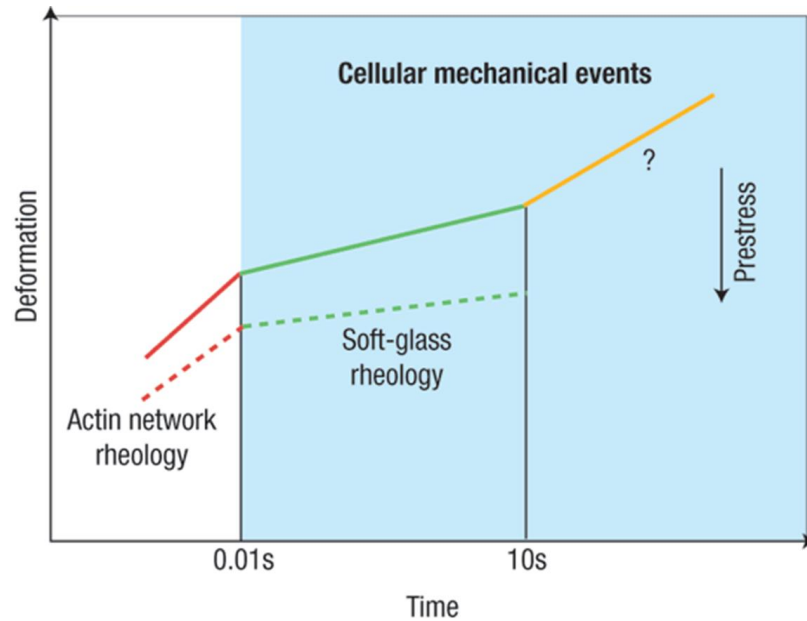
Figure 1.1: Cell viscoelastic behavior in different deformation regimes. Cells deformed at time scales >0.01 s demonstrate soft-glass rheology, or mechanical behavior dominated by elastic material properties. Cells deformed at faster time scales <0.01 s exhibit actin network rheology, or viscoelastic behavior governed by the properties of the actin network. There is potential for a third regime of slow creep to exist at time scales >10 s, but the mechanisms that govern this regime are still unknown. Figure reproduced with permission from reference [5].

Over the duration of compression at a constant strain, cells exhibit creep expansion in a direction orthogonal to the compression. This expansion is characterized by an initial elastic deformation response followed by a slower viscoelastic creep [7-9]. Studies in which cells are fully aspirated into a micropipette were conducted to observe cell deformation behavior in these regimes (Figure 1.2A,B). Micropipette studies have shown that a cell undergoing compression exhibits an initial phase of elastic, rapid expansion in the direction orthogonal to the applied force, followed by a slower viscoelastic creep phase until equilibrium is reached (Figure 1.2C) [7,9]. Biophysical studies of slower, gradual

deformations show that cells exhibit viscous deformation behavior without changing in volume [10-13]. Rapid cell compression by micropipette aspiration can cause cells to lose some intracellular volume [7,9]. The magnitude of volume loss is shown to be dependent on the ratio of the cell diameter to the micropipette diameter (Figure 1.2D) [7,9]. While the time scale at which this cell volume loss occurs is described as being on the same order of the aspiration time, the compression time scale required for cell volume loss was not precisely quantified. The question of the time scale at which cells transition from the regime of volume conservation to the regime of volume loss during compression is a major motivator for this thesis work.
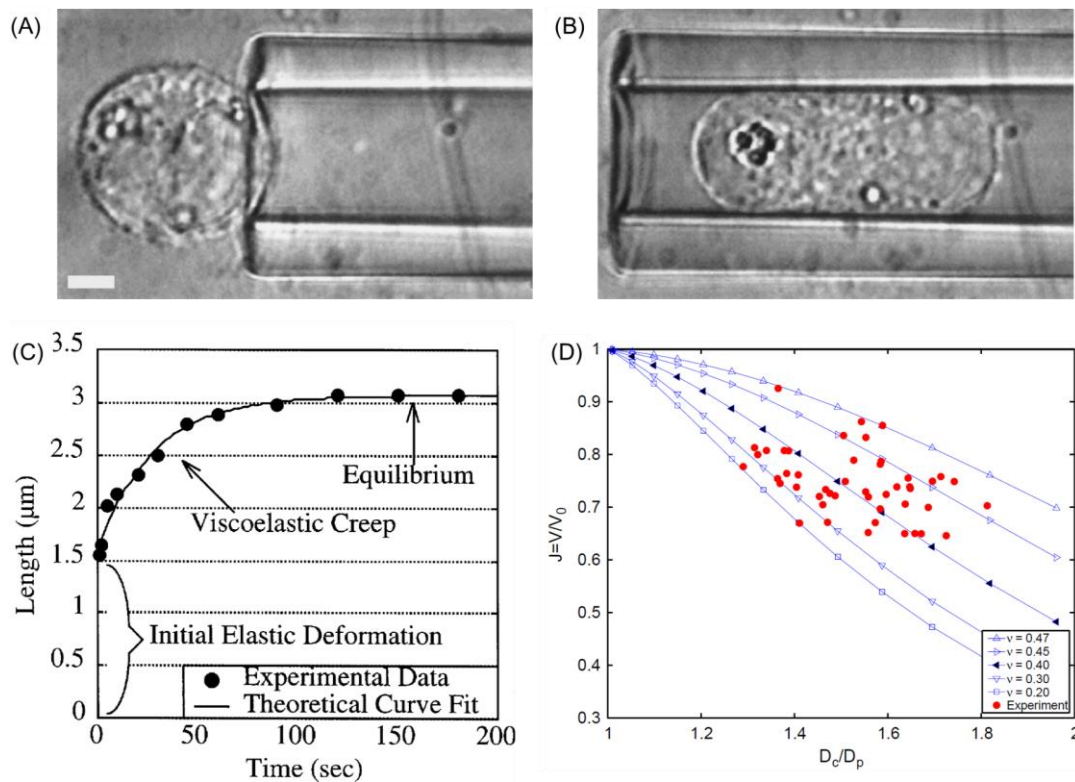
Figure 1.2: Cell deformation and volume change in micropipette study. (A) A human chondrocyte before aspiration into a micropipette. (B) The same cell after aspiration into a micropipette. Cell volume measurements can be extracted from this image. (C) A deformed cell exhibits initial elastic expansion orthogonal to the applied force, followed by slower viscoelastic creep before reaching equilibrium. Figures reproduced with permission from

3

reference [7]. (D) Measurement of cell volume change during micropipette aspiration. As cell diameter (D_c) gets increasingly larger than micropipette diameter (D_p), the volume ratio ($J = V/V_o$) decreases. Therefore, cells that are much larger than the micropipette diameter lose more volume. Figure reproduced with permission from reference [9].

1.1.2   Cell Recovery after Deformation

After deformation, cells recover to their pre-deformation shape [12,14,15]. The time scale of cell recovery is shown to be dependent on the time scale of duration of the deformation. Cells that experience a compression that is short in duration will relax on a faster time scale, whereas cells that experience a longer compression will relax slower [15]. Following a brief compression, cells exhibit fast cell shape recovery that is consistent with rapid, poroelastic recovery behavior of the cytoplasm at short time scales (<0.5 s) after brief compression [15,16].

Cells that lose volume during compression must return to their pre-compression volume as they recover shape after deformation. We hypothesize this volume recovery would require cell uptake of surrounding fluid volume, including solvent and any molecules suspended therein. However, studies of rapid cell mechanical compression have not characterized the phenomenon of cell volume recovery after mechanically-induced volume loss. The mechanism and nature of this cell volume recovery behavior is another major motivation for this thesis work. This cell volume recovery behavior is of interest not only to broaden our understanding of cell deformation mechanics, but also as a potential mechanism for intracellular delivery of target molecules suspended in the surrounding buffer.

4

1.2 Intracellular Delivery Mechanisms

The efficient delivery of molecules into cells to change or analyze their physiological state is an indispensable need for a wide range of biomedical uses, ranging from diagnostics to cell therapy manufacturing. The demand for engineered cells is increasing rapidly with the emergence of life-saving clinical applications in regenerative medicine, gene editing, and cell immunotherapies. However, cell manufacturing is drastically hindered by the cost and inefficiency of current techniques for intracellular delivery of macromolecules. Cell therapies require cell engineering methods that can efficiently process therapeutic doses on the order of 1 billion cells at low cost. The resulting cell therapeutic product should also be high in viability, since low viability in therapeutic cells can adversely affect treatment outcomes [17-19]. Therefore, the FDA recommends that therapeutic cell infusions have viability of at least 85% [20,21]. Furthermore, there are several cargo types of interest for intracellular delivery, so an ideal delivery method should be capable of delivering molecules with diverse material properties [22]. However, existing techniques for intracellular delivery of macromolecule and particle reagents do not adequately meet the growing demands in the cell therapy industry for scalability, high cell viability, and broad applicability for many cell and molecule types.

1.2.1 Viral Transduction

Viral transduction is one of the earliest developed gene editing methods and remains one of the most widely used cell engineering techniques in both clinical and research settings. However, viral transduction is restricted in clinical applications by high costs, scale-up limitations, and long-standing safety concerns associated with random

insertional mutagenesis [23-29]. Furthermore, viral capsids have packing limits that restrict their applications in the delivery of large genetic constructs. The two most commonly used viral vectors, adeno-associated virus and lentivirus, exhibited significantly reduced viral titers when packaging vector genomes larger than 5 kb and 9 kb, respectively [30,31]. Limitations in genetic cargo size is a major drawback, as the cell therapy industry increasingly demands multiple gene edits and larger genetic constructs to prevent disease relapse and improve the safety and efficacy of cell therapies [32,33].

1.2.2   Endocytic Particles

Non-viral endocytic mechanisms for delivering cargo into cells include lipid-based particles, cationic particles, cell-penetrating peptides, and polymer particles. These methods use chemical or particle carriers attached to the target delivery molecule to induce cells to endocytose the cargo. Once internalized by the cell, the cargo must escape the endosome before degradation occurs in order to perform their intended functions [25,34-36]. These particles are significantly lower in cost than viral vectors and have been increasingly utilized in research laboratory settings. However endocytic particles can cause lasting damage to the cell membrane, have a significant tradeoff between delivery efficiency and cell viability, and the endosomal delivery mechanism causes the majority of delivered molecules to be detained and degraded in lysosomes [25,34-36]. Furthermore, the use of chemical transfection agents can impact cell function and requires more rigorous study in order to be approved by the United States Food and Drug Administration (FDA) for use in patients, which limits the clinical applications of these methods.

1.2.3 Electroporation

Electroporation is a physical method of intracellular delivery that uses electrical currents to form pores in the cell membrane coupled with electrophoresis to drive charged target molecules through these pores. Electroporation is a rapid cell engineering method that is effective for many cell types. However the electrophoretic driving mechanism is only ideally suited for charged molecules and can result in inconsistent delivery with low cell viability [25,37,38]. Many intracellular delivery cargoes of interest, such as proteins and nanoparticles, do not have charge properties that are favorable for electroporation delivery. The inconsistent and cytotoxic nature of electroporation makes it difficult to scale up to clinical doses of engineered cells with high viability. Furthermore, electroporation has been shown to accelerate cell exhaustion, which complicates the expansion step of the cell manufacturing process and limits the persistence and effectiveness of the resulting cell therapies [39].

1.2.4 Mechanoporation for diffusive delivery

Mechanical methods, such as mechanoporation, are a promising approach to deliver molecules directly to the cytoplasm with high cell viability. Mechanoporation has been shown to be effective in delivering various target molecules into a variety of human cell types [40-45]. A microfluidic implementation of these mechanisms results in high throughput processing, up to 10^6 cells/s. Existing microfluidic mechanoporation methods impart shear stress on cells to open pores in the cell membrane. Shear stress can be applied as fluid shear by rapidly flowing cells through a narrow microchannel that is larger than the cell diameter [40]. Ultrasonic pressure waves focused through a narrow microchannel

can also be used to permeabilize cell membranes through acoustic shear poration [25,46]. Microfluidic devices can exert frictional shear on cells using microchannels that are smaller than the cell diameter; gradual constrictions are used to impart shear stress on cells without clogging the single-cell channels [41-44,47-51]. After these methods of microfluidic cell shear open pores in the cell membrane, intracellular molecule delivery occurs by diffusion down a concentration gradient through the resulting cell membrane pores. While diffusion is a universal driving force, it is governed by the Stokes-Einstein Law for diffusion in solution (Equation 1.1) [52].

$$\textbf{\textit{Stokes} − \textit{Einstein diffusivity } D = \frac{k_B\,T}{6\,\pi\,\mu\,r}} \qquad\qquad (1.1)$$

Where D is the diffusion constant, k_B is Boltzmann's constant, T is temperature, μ is the dynamic viscosity, and r is the radius of the diffusing particle. For non-spherical, linear macromolecules such as DNA and RNA, diffusivity (D) has the following inverse relation with polymer length: $D \sim L^{-v}$, where $v \cong 0.588$ and L is the polymer length [53]. Therefore diffusion is constrained by the inverse relationship between diffusivity and molecule size or length. We note existing approaches to microfluidic mechanoporation have shown limited efficiency in the delivery of large macromolecules [40,42,44,47,49,51]. While mechanoporation has many desirable properties for intracellular delivery, the reliance on diffusion as the sole driving mechanism of molecule transport into the cell is a major limitation on the applications of this method for delivery of large macromolecules that are of therapeutic interest, such as DNA (>1 MDa). This limitation has motivated this thesis work to investigate the cell deformation regime of cell volume loss and recovery as a potential new driving mechanism for intracellular delivery.

1.2.5 *Mechanoporation for convective delivery*

Most physical approaches for delivering exogenous materials into single cells are based upon the creation of pores and then using electric charge (electrophoresis) and/or concentration gradient (passive diffusion) to drive them in. We provide a new driving force of convection through the controlled, transient exchange of cell volume. Convection is broadly considered to be a type of mass transfer that occurs due to bulk fluid motion. More specifically, mass transfer due to convection occurs due to contributions from both diffusion, wherein particles travel down a concentration gradient, and advection, wherein particles are directionally transported due to bulk fluid flow [54,55].

This thesis aims to study the intracellular delivery capabilities of a convective driving mechanism. Methods that use diffusion alone as an intracellular delivery driving mechanism have been shown to be limited in the size of the molecules that can efficiently be delivered [40,42,44,47,49,51]. Our objective is to study a mechanical method of causing cells to exchange volume and macromolecules with the surrounding fluid. This method utilizes the inherent ability of cells to rapidly deform and then recover shape in response to mechanical compression [12,14,15]. In regimes of cell compression in which cells lose intracellular volume, we hypothesize that cells must uptake surrounding volume in order to recover from deformation and return to pre-compression shape and volume [7,9]. The intracellular uptake of external fluid volume would necessitate a bulk fluid flow from the cell exterior to the cell interior, and any molecules suspended in that fluid would be carried into the cell in an advection-dominated intracellular delivery mechanism. We call this convective intracellular delivery phenomenon cell VECT, or cell volume exchange for convective transfer.

In this thesis, we develop and characterize a microfluidic technology that uses purely mechanical interactions to cause cell volume exchange for convective intracellular delivery of large macromolecules. The microfluidic device uses rectangular ridges within a microchannel to exert abrupt compressions on the cell, resulting in a sudden viscoelastic response that results in a change in shape and temporary reduction in volume [14,15,56,57]. The compacted cell state creates potential for the cell to uptake surrounding molecules as it rapidly recuperates lost volume, causing an influx of surrounding volume and molecules that is driven by advection and therefore not subject to the molecule size limitations of diffusive delivery.

The results of this thesis have informed the development and optimization of the cell VECT device design for useful applications in intracellular delivery. We experimentally determined that intracellular delivery can be improved by increasing the magnitude and velocity of cell compressions [58,59]. Our findings show that convective delivery occurs at a rapid time scale during cell volume exchange inside the device [58]. We found that convective delivery can be repeated and maintained for multiple compressions to maximize volume exchange and intracellular molecule delivery [58,59]. Effective multiplexing of the cell processing microchannels enables high throughput processing (up to 10^6 cells/s). Successful delivery of large macromolecules and plasmids (>2 MDa) demonstrate utility for cell engineering techniques that require the delivery of large reagents [58,59]. Cells processed using cell VECT maintain high proliferation and viability (>95%) [58,59]. This unique combination of features, including high throughput, maintained viability, and efficient delivery of large macromolecules, position cell VECT for various useful applications for intracellular delivery.

1.3 Motivations for Intracellular Delivery

There exist a wide variety of useful applications for intracellular delivery of various macromolecules in both research and clinical settings. Intracellular delivery of several types of molecules, including contrast agents and gene expression probes, allow for cell labeling, tracking, and analysis of intracellular gene expression. Delivery of cell transfection or gene editing reagents allow for temporary or permanent modification of gene expression for research and therapeutic applications. In this thesis we will explore potential applications for intracellular delivery for cell labeling and analysis and modification of cell gene expression.

1.3.1 Intracellular labeling and analysis

The growing field of cell engineering requires assays to characterize the cell state in order to monitor gene expression and elucidate gene interaction and signaling pathways. To fully understand cell behavior, these assays must be able to provide information on both external and internal cell activity. The vast majority of cell proteins are expressed in the cell interior. However, current gene expression assays that do not compromise cell viability are typically limited to analysis of genes expressed on the cell surface. Current standard intracellular gene expression assays analyze DNA, RNA, or proteins extracted from a lysed cell. Therefore, these methods are unable to provide information on temporal trends in gene expression, since the analysis only takes a snapshot of the cell gene expression profile at the moment in time when it was lysed. Furthermore, this method does not provide information on the intracellular localization of the gene expression [60,61]. Intracellular staining and imaging methods do provide information on intracellular localization of gene

expression. However, intracellular staining requires cells to be fixed and permeabilized, which prevents tracking of gene expression over time [60,61]. Therefore, the field of cell engineering would greatly benefit from gene expression assays that can be performed on viable cells, allowing for real-time analysis of intracellular gene expression in living cells [60,61].

While characterization of gene expression levels and protein localization is an important capability, a complete understanding of intracellular activities and signaling pathways requires the ability to analyze intracellular molecular interactions and modifications. The field of in-cell nuclear magnetic resonance (NMR) spectroscopy seeks to characterize the molecular structure and interactions of biological molecules in their native environment, at physiological conditions in the living cell [62,63]. Analysis of intracellular protein interactions and modifications facilitates the study of intracellular protein signaling mechanisms and pathways. Detection and analysis of a target protein using in-cell NMR requires the target signal to be distinguishable from the background signal of other intracellular proteins. Therefore, the target protein concentration usually must exceed typical physiological levels in order to be detectable [62,63]. Therefore, in-cell NMR methods for the study of protein structure and modifications requires methods for intracellular delivery of the target proteins above physiological levels.

Intracellular analysis of gene expression and protein interactions are both valuable research tools for the field of cell engineering. In a clinical setting, there are also useful applications for intracellular delivery that would potentially integrate into and enhance the effectiveness of existing cell therapy methodologies. Current methods in stem cell transplant therapies for regenerative medicine typically harvest autologous stem cells and

12

transplant them into a disease site in a single surgical procedure [64,65]. This procedure does not allow for cells to be labeled before transplantation, which makes tracking cell localization and therapeutic progression difficult. Therefore, clinicians have a very limited ability to monitor treatment progression and intervene in the case of complications [66-68].

Current methods for labeling of therapeutic stem cells for *in vivo* tracking require the cells to be processed in a lab environment, often exposing them to transfection agents for several hours. This lengthy processing time does not allow for cells to be harvested, labeled, and transplanted in a single surgery, which would require the patient to undergo a second surgical procedure, which drives up costs and risks for complications and infections. Furthermore, the cells are required to leave the operating room to undergo chemical processing, which exposes the cells to potential contamination risks [69] and can potentially impact stem cell physiology and potency [70-72]. Therefore, a rapid method of intracellular labeling would facilitate a single surgical procedure in which cells can be harvested, labeled, and transplanted without leaving the operating room.

1.3.2 *Modification of cell gene expression*

Cell engineering has been applied to great effect in the treatment of cancer through cell-based immunotherapies. The field of cell-based immunotherapies, or cell therapies, utilizes genetically modified immune cells, typically cytotoxic T-cells, to target and eliminate cancer cells. A preponderance of successes in clinical trials has led to the FDA approval of chimeric antigen receptor (CAR) T-cells for the treatment of multiple indications of B cell lymphoma and B cell lymphoblastic leukemia [73-77]. CAR T-cells are a promising cancer therapy wherein patient T-cells are transfected to express an

artificial antigen receptor on the cell surface that causes them to target cancer cells for externally-induced apoptosis. However, current CAR T-cell manufacturing practices must overcome many challenges before they are suitable for large-scale, affordable treatments. There are long-standing safety concerns with permanent viral genetic modification of T-cells [37,78]. Additionally, manufacturing requires 10-14 days of *ex vivo* T-cell expansion and viral transfection. This lengthy and costly process has resulted in newly approved CAR T therapies from Kite and Novartis costing several hundreds of thousands of dollars for a single treatment. Furthermore, the use of multiple edits in manufacturing CAR T-cell therapies has been shown to improve treatment efficacy [32,33]. Targeted insertion of the CAR gene at the TRAC locus, rather than a random insertion location, has been shown to improve tumor rejection in CAR T therapies [79].

While CAR T-cells have been approved by the FDA, their effectiveness has mainly been limited to blood-based cancers. In the field of solid tumor treatment, T-cell receptor (TCR) therapies have shown promising results. However, the field of TCR therapies often requires multiple gene edits. In addition to introducing an exogenous, modified TCR gene, edits to permanently silence the endogenous TCR gene are used to prevent dangerous and unpredictable interactions with the exogenous, edited TCR [80]. Therefore, both CAR T-cells and TCR therapies would greatly benefit from efficient gene editing techniques that facilitate multiple gene edits without prohibitively impacting cell viability or manufacturing cost. Overall, the next generation of cell-based therapies would greatly benefit from nonviral intracellular delivery methods capable delivering large constructs for multiple edits and targeted gene editing.

14

1.4 References

[1]   Bursac, P. *et al.* Cytoskeletal remodelling and slow dynamics in the living cell. *Nat. Mater.* **4**, 557-561, doi:10.1038/nmat1404 (2005).

[2]   Deng, L. *et al.* Fast and slow dynamics of the cytoskeleton. *Nat. Mater.* **5**, 636-640, doi:10.1038/nmat1685 (2006).

[3]   Fabry, B. *et al.* Scaling the microrheology of living cells. *Phys. Rev. Lett.* **87**, 148102, doi:10.1103/PhysRevLett.87.148102 (2001).

[4]   Lenormand, G. & Fredberg, J. J. Deformability, dynamics, and remodeling of cytoskeleton of the adherent living cell. *Biorheology.* **43**, 1-30 (2006).

[5]   Stamenovic, D. Cell mechanics: two regimes, maybe three? *Nat. Mater.* **5**, 597-598, doi:10.1038/nmat1700 (2006).

[6]   Gardel, M. L. *et al.* Scaling of F-actin network rheology to probe single filament elasticity and dynamics. *Phys. Rev. Lett.* **93**, 188102, doi:10.1103/PhysRevLett.93.188102 (2004).

[7]   Jones, W. R. *et al.* Alterations in the Young's modulus and volumetric properties of chondrocytes isolated from normal and osteoarthritic human cartilage. *J. Biomech.* **32**, 119-127, doi:Doi 10.1016/S0021-9290(98)00166-3 (1999).

[8]   Thoumine, O. & Ott, A. Time scale dependent viscoelastic and contractile regimes in fibroblasts probed by microplate manipulation. *J. Cell Sci.* **110 (Pt 17)**, 2109-2116 (1997).

[9]   Trickey, W. R., Baaijens, F. P. T., Laursen, T. A., Alexopoulos, L. G. & Guilak, F. Determination of the Poisson's ratio of the cell: recovery properties of chondrocytes after release from complete micropipette aspiration. *J. Biomech.* **39**, 78-87, doi:10.1016/j.jbiomech.2004.11.006 (2006).

[10]   Mokbel, M. *et al.* Numerical Simulation of Real-Time Deformability Cytometry To Extract Cell Mechanical Properties. *ACS Biomater. Sci. Eng.*, doi:10.1021/acsbiomaterials.6b00558 (2017).

[11]   Guo, Q., Park, S. & Ma, H. Microfluidic micropipette aspiration for measuring the deformability of single cells. *Lab Chip.* **12**, 2687-2695, doi:10.1039/c2lc40205j (2012).

[12]   Needham, D. & Hochmuth, R. M. Rapid flow of passive neutrophils into a 4 microns pipet and measurement of cytoplasmic viscosity. *J. Biomech. Eng.* **112**, 269-276 (1990).

[13]   Zheng, Y., Nguyen, J., Wei, Y. & Sun, Y. Recent advances in microfluidic techniques for single-cell biophysical characterization. *Lab Chip.* **13**, 2464-2483, doi:10.1039/c3lc50355k (2013).

[14]   Evans, E. A. Structural model for passive granulocyte behaviour based on mechanical deformation and recovery after deformation tests. *Kroc Found. Ser.* **16**, 53-71 (1984).

[15]   Tran-Son-Tay, R., Needham, D., Yeung, A. & Hochmuth, R. M. Time-dependent recovery of passive neutrophils after large deformation. *Biophys. J.* **60**, 856-866, doi:10.1016/S0006-3495(91)82119-1 (1991).

[16]   Moeendarbary, E. *et al.* The cytoplasm of living cells behaves as a poroelastic material. *Nat. Mater.* **12**, 253-261, doi:http://www.nature.com/nmat/journal/v12/n3/abs/nmat3517.html#supplementary-information (2013).

[17]   Allan, D. S. *et al.* Number of viable CD34(+) cells reinfused predicts engraftment in autologous hematopoietic stem cell transplantation. *Bone Marrow Transplant.* **29**, 967-972, doi:10.1038/sj.bmt.1703575 (2002).

[18]   Lee, S. *et al.* Post-thaw viable CD34+ cell count is a valuable predictor of haematopoietic stem cell engraftment in autologous peripheral blood stem cell transplantation. *Vox Sanguinis.* **94**, 146-152, doi:10.1111/j.1423-0410.2007.01009.x (2008).

[19]   Yang, H. *et al.* Association of post-thaw viable CD34+ cells and CFU-GM with time to hematopoietic engraftment. *Bone Marrow Transplant.* **35**, 881-887, doi:10.1038/sj.bmt.1704926 (2005).

[20]   Fenske, T. S. *et al.* Autologous or reduced-intensity conditioning allogeneic hematopoietic cell transplantation for chemotherapy-sensitive mantle-cell lymphoma: analysis of transplantation timing and modality. *J Clin Oncol.* **32**, 273-281, doi:10.1200/JCO.2013.49.2454 (2014).

[21]   Wirk, B. *et al.* Outcomes of hematopoietic cell transplantation for diffuse large B cell lymphoma transformed from follicular lymphoma. *Biol Blood Marrow Transplant.* **20**, 951-959, doi:10.1016/j.bbmt.2014.03.014 (2014).

[22]   Stewart, M. P. *et al.* In vitro and ex vivo strategies for intracellular delivery. *Nature.* **538**, 183-192, doi:10.1038/nature19764 (2016).

[23]   Osumi, N. & Inoue, T. Gene Transfer into Cultured Mammalian Embryos by Electroporation. *Methods.* **24**, 35-42, doi:http://dx.doi.org/10.1006/meth.2001.1154 (2001).

[24]   Glover, D. J., Lipps, H. J. & Jans, D. A. Towards safe, non-viral therapeutic gene expression in humans. *Nat. Rev. Genet.* **6**, 299-310 (2005).

[25]   Meacham, J. M., Durvasula, K., Degertekin, F. L. & Fedorov, A. G. Physical methods for intracellular delivery: practical aspects from laboratory use to industrial-scale processing. *J. Lab Autom.* **19**, 1-18, doi:10.1177/2211068213494388 (2014).

[26]   Kim, T. K. & Eberwine, J. H. Mammalian cell transfection: the present and the future. *Anal. Bioanal. Chem.* **397**, 3173-3178, doi:10.1007/s00216-010-3821-6 (2010).

[27]   Yang, S., Rosenberg, S. A. & Morgan, R. A. Clinical-scale lentiviral vector transduction of PBL for TCR gene therapy and potential for expression in less-differentiated cells. *J. Immunother.* **31**, 830-839, doi:10.1097/CJI.0b013e31818817c5 (2008).

[28]   Dodo, K. *et al.* An efficient large-scale retroviral transduction method involving preloading the vector into a RetroNectin-coated bag with low-temperature shaking. *PLoS One.* **9**, e86275, doi:10.1371/journal.pone.0086275 (2014).

[29]   Zhao, Y. *et al.* Multiple injections of electroporated autologous T cells expressing a chimeric antigen receptor mediate regression of human disseminated tumor. *Cancer Res.* **70**, 9053-9061, doi:10.1158/0008-5472.CAN-10-2880 (2010).

[30]   Wu, Z., Yang, H. & Colosi, P. Effect of genome size on AAV vector packaging. *Mol Ther.* **18**, 80-86, doi:10.1038/mt.2009.255 (2010).

[31]   Kumar, M., Keller, B., Makalou, N. & Sutton, R. E. Systematic determination of the packaging limit of lentiviral vectors. *Hum Gene Ther.* **12**, 1893-1905, doi:10.1089/104303401753153947 (2001).

[32]   Rupp, L. J. *et al.* CRISPR/Cas9-mediated PD-1 disruption enhances anti-tumor efficacy of human chimeric antigen receptor T cells. *Sci. Rep.* **7**, 737, doi:10.1038/s41598-017-00462-8 (2017).

[33]   Schultz, L. & Mackall, C. Driving CAR T cell translation forward. *Sci Transl Med.* **11**, doi:10.1126/scitranslmed.aaw2127 (2019).

[34]   Zorko, M. & Langel, Ü. Cell-penetrating peptides: mechanism and kinetics of cargo delivery. *Adv. Drug Delivery Rev.* **57**, 529-545, doi:http://dx.doi.org/10.1016/j.addr.2004.10.010 (2005).

[35]   Joliot, A. & Prochiantz, A. Transduction peptides: from technology to physiology. *Nat. Cell Biol.* **6**, 189-196 (2004).

[36]   Bechara, C. & Sagan, S. Cell-penetrating peptides: 20 years later, where do we stand? *FEBS Letters.* **587**, 1693-1702, doi:10.1016/j.febslet.2013.04.031 (2013).

[37]   Boissel, L., Betancur, M., Wels, W. S., Tuncer, H. & Klingemann, H. Transfection with mRNA for CD19 specific chimeric antigen receptor restores NK cell mediated

killing of CLL cells. *Leuk. Res.* **33**, 1255-1259, doi:10.1016/j.leukres.2008.11.024 (2009).

[38]   Yarmush, M. L., Golberg, A., Sersa, G., Kotnik, T. & Miklavcic, D. Electroporation-Based Technologies for Medicine: Principles, Applications, and Challenges. *Annu. Rev. Biomed. Eng.* **16**, 295-320, doi:10.1146/annurev-bioeng-071813-104622 (2014).

[39]   DiTommaso, T. *et al.* Cell engineering with microfluidic squeezing preserves functionality of primary immune cells in vivo. *Proc. Natl. Acad. Sci. U. S. A.* **115**, E10907-E10914, doi:10.1073/pnas.1809671115 (2018).

[40]   Hallow, D. M. *et al.* Shear-induced intracellular loading of cells with molecules by controlled microfluidics. *Biotechnol. Bioeng.* **99**, 846-854, doi:10.1002/bit.21651 (2008).

[41]   Han, X. *et al.* CRISPR-Cas9 delivery to hard-to-transfect cells via membrane deformation. *Sci. Adv.* **1**, e1500454, doi:10.1126/sciadv.1500454 (2015).

[42]   Saung, M. T. *et al.* A Size-Selective Intracellular Delivery Platform. *Small.* doi:10.1002/smll.201601155 (2016).

[43]   Sharei, A. *et al.* Cell squeezing as a robust, microfluidic intracellular delivery platform. *J. Visualized Exp.*, e50980, doi:10.3791/50980 (2013).

[44]   Sharei, A. *et al.* Ex vivo cytosolic delivery of functional macromolecules to immune cells. *PLoS One.* **10**, e0118803, doi:10.1371/journal.pone.0118803 (2015).

[45]   Zarnitsyn, V. G. *et al.* Electrosonic ejector microarray for drug and gene delivery. *Biomed. Microdevices.* **10**, 299-308, doi:10.1007/s10544-007-9137-4 (2008).

[46]   Meacham, J. M., Durvasula, K., Degertekin, F. L. & Fedorov, A. G. Enhanced intracellular delivery via coordinated acoustically driven shear mechanoporation and electrophoretic insertion. *Sci. Rep.* **8**, 3727, doi:10.1038/s41598-018-22042-0 (2018).

[47]   Ding, X. *et al.* High-throughput nuclear delivery and rapid expression of DNA via mechanical and electrical cell-membrane disruption. *Nat. Biomed. Eng.* **1**, 0039, doi:10.1038/s41551-017-0039.   http://www.nature.com/articles/s41551-017-0039#supplementary-information (2017).

[48]   Kollmannsperger, A. *et al.* Live-cell protein labelling with nanometre precision by cell squeezing. *Nat. Commun.* **7**, 10372, doi:10.1038/ncomms10372 (2016).

[49]   Szeto, G. L. *et al.* Microfluidic squeezing for intracellular antigen loading in polyclonal B-cells as cellular vaccines. *Sci. Rep.* **5**, 10276, doi:10.1038/srep10276 (2015).

[50]   Lee, J. *et al.* Nonendocytic delivery of functional engineered nanoparticles into the cytoplasm of live cells using a novel, high-throughput microfluidic device. *Nano Lett.* **12**, 6322-6327, doi:10.1021/nl303421h (2012).

[51]   Sharei, A. *et al.* Plasma membrane recovery kinetics of a microfluidic intracellular delivery platform. *Integr. Biol.* **6**, 470-475, doi:10.1039/c3ib40215k (2014).

[52]   Tuteja, A., Mackay, M. E., Narayanan, S., Asokan, S. & Wong, M. S. Breakdown of the continuum stokes-einstein relation for nanoparticle diffusion. *Nano Lett.* **7**, 1276-1281, doi:10.1021/nl070192x (2007).

[53]   Robertson, R. M., Laib, S. & Smith, D. E. Diffusion of isolated DNA molecules: dependence on length and topology. *Proc. Natl. Acad. Sci. U. S. A.* **103**, 7310-7314, doi:10.1073/pnas.0601903103 (2006).

[54]   Ramaswamy, B. Finite element solution for advection and natural convection flows. *Computers & Fluids.* **16**, 349-388, doi:https://doi.org/10.1016/0045-7930(88)90023-0 (1988).

[55]   Manzini, G. & Russo, A. A finite volume method for advection–diffusion problems in convection-dominated regimes. *Computer Methods in Applied Mechanics and Engineering.* **197**, 1242-1261, doi:https://doi.org/10.1016/j.cma.2007.11.014 (2008).

[56]   Lokhandwalla, M. & Sturtevant, B. Mechanical haemolysis in shock wave lithotripsy (SWL): I. Analysis of cell deformation due to SWL flow-fields. *Phys. Med. Biol.* **46**, 413-437 (2001).

[57]   Chien, S., Schmid-Schonbein, G. W., Sung, K. L., Schmalzer, E. A. & Skalak, R. Viscoelastic properties of leukocytes. *Kroc Found. Ser.* **16**, 19-51 (1984).

[58]   Liu, A. *et al.* Microfluidic generation of transient cell volume exchange for convectively driven intracellular delivery of large macromolecules. *Mater. Today.* **21**, 703-712, doi:10.1016/j.mattod.2018.03.002 (2018).

[59]   Liu, A. *et al.* Cell Mechanical and Physiological Behavior in the Regime of Rapid Mechanical Compressions that Lead to Cell Volume Change. *Small.* e1903857, doi:10.1002/smll.201903857 (2019).

[60]   Santangelo, P. J., Alonas, E., Jung, J., Lifland, A. W. & Zurla, C. Probes for intracellular RNA imaging in live cells. *Methods Enzymol.* **505**, 383-399, doi:10.1016/B978-0-12-388448-0.00028-0 (2012).

[61]   Lahm, H. *et al.* Detection of Intracellular Gene Expression in Live Cells of Murine, Human and Porcine Origin Using Fluorescence-labeled Nanoparticles. *J. Visualized Exp.*, 53268, doi:10.3791/53268 (2015).

[62] Sciolino, N., Burz, D. S. & Shekhtman, A. In-Cell NMR Spectroscopy of Intrinsically Disordered Proteins. *PROTEOMICS.* **19**, 1800055, doi:10.1002/pmic.201800055 (2019).

[63] Breindel, L., Burz, D. S. & Shekhtman, A. Interaction proteomics by using in-cell NMR spectroscopy. *Journal of Proteomics.* **191**, 202-211, doi:https://doi.org/10.1016/j.jprot.2018.02.006 (2019).

[64] Squillaro, T., Peluso, G. & Galderisi, U. Clinical Trials With Mesenchymal Stem Cells: An Update. *Cell Transplant.* **25**, 829-848, doi:10.3727/096368915X689622 (2016).

[65] Coughlin, R. P., Oldweiler, A., Mickelson, D. T. & Moorman, C. T., 3rd. Adipose-Derived Stem Cell Transplant Technique for Degenerative Joint Disease. *Arthrosc Tech.* **6**, e1761-e1766, doi:10.1016/j.eats.2017.06.048 (2017).

[66] Khurana, A. *et al.* Iron administration before stem cell harvest enables MR imaging tracking after transplantation. *Radiology.* **269**, 186-197, doi:10.1148/radiol.13130858 (2013).

[67] Henning, T. D. *et al.* Magnetic Resonance Imaging of Ferumoxide-Labeled Mesenchymal Stem Cells in Cartilage Defects: In Vitro and In Vivo Investigations. *Molecular imaging.* doi:10.2310/7290.2011.00040 (2011).

[68] Theruvath, A. J. *et al.* Tracking Stem Cell Implants in Cartilage Defects of Minipigs by Using Ferumoxytol-enhanced MRI. *Radiology.* 182176, doi:10.1148/radiol.2019182176 (2019).

[69] FDA. Inspection of Human Cells, Tissues, and Cellular and Tissue-Based Products (HCT/Ps). (2012).

[70] Kuroda, T., Yasuda, S. & Sato, Y. Tumorigenicity studies for human pluripotent stem cell-derived products. *Biol Pharm Bull.* **36**, 189-192 (2013).

[71] Motaln, H., Schichor, C. & Lah, T. T. Human mesenchymal stem cells and their use in cell-based therapies. *Cancer.* **116**, 2519-2530, doi:10.1002/cncr.25056 (2010).

[72] Soenen, S. J. & De Cuyper, M. Assessing cytotoxicity of (iron oxide-based) nanoparticles: an overview of different methods exemplified with cationic magnetoliposomes. *Contrast Media Mol Imaging.* **4**, 207-219, doi:10.1002/cmmi.282 (2009).

[73] Maude, S. L. *et al.* Chimeric antigen receptor T cells for sustained remissions in leukemia. *N Engl J Med.* **371**, 1507-1517, doi:10.1056/NEJMoa1407222 (2014).

[74] Davila, M. L. *et al.* Efficacy and toxicity management of 19-28z CAR T cell therapy in B cell acute lymphoblastic leukemia. *Sci Transl Med.* **6**, 224ra225, doi:10.1126/scitranslmed.3008226 (2014).

[75] Lee, D. W. *et al.* T cells expressing CD19 chimeric antigen receptors for acute lymphoblastic leukaemia in children and young adults: a phase 1 dose-escalation trial. *Lancet.* **385**, 517-528, doi:10.1016/S0140-6736(14)61403-3 (2015).

[76] Schubert, M. L. *et al.* Chimeric Antigen Receptor T Cell Therapy Targeting CD19-Positive Leukemia and Lymphoma in the Context of Stem Cell Transplantation. *Hum Gene Ther.* doi:10.1089/hum.2016.097 (2016).

[77] Lim, W. A. & June, C. H. The Principles of Engineering Immune Cells to Treat Cancer. *Cell.* **168**, 724-740, doi:10.1016/j.cell.2017.01.016 (2017).

[78] Turtle, C. J. *et al.* CD19 CAR-T cells of defined CD4(+): CD8(+) composition in adult B cell ALL patients. *J Clin Invest.* **126**, 2123-2138, doi:10.1172/Jci85309 (2016).

[79] Eyquem, J. *et al.* Targeting a CAR to the TRAC locus with CRISPR/Cas9 enhances tumour rejection. *Nature.* **543**, 113-117, doi:10.1038/nature21405 (2017).

[80] Roth, T. L. *et al.* Reprogramming human T cell function and specificity with non-viral genome targeting. *Nature.* **559**, 405-409, doi:10.1038/s41586-018-0326-5 (2018).

CHAPTER 2.   THESIS OVERVIEW

2.1   Introduction to Cell VECT

In this thesis, we will characterize the newly discovered behavior of cell volume exchange caused by rapid mechanical compression and recovery and apply this phenomenon for convective intracellular macromolecule delivery. Rapid cell deformation is caused by flowing cells through a microfluidic channel with ridges with rectangular cross-sections that were repeated within a microchannel to precisely exert abrupt and brief compressions upon cells. Hydrodynamic forces maintain high cell velocity throughout multiple constrictions, while the angled ridges remove dead cells and clusters of cells which could cause occlusions [1-3].

We determined through high-speed microscopy experiments that volume change is increased at higher velocity and magnitude of compression, and that cells were partially able to recover their volume on the time scale of ~1 ms after each compressive event. Characterization of cell integrity, viability, and related gene expression demonstrated no detrimental effects, even for volume changes of up to 30%.

This surprising ability of cells to rapidly exchange fluid with their surroundings in response to ultrafast mechanical compressions presents a potent new way to deliver large extracellular molecules and particles into cells that solves limitations imposed by simple diffusive transport through mechanically-induced pores. We utilized this method of cell volume exchange for convective transfer (VECT) to intracellularly deliver molecules and particles suspended in surrounding extracellular buffer. The ability of cell VECT to

efficiently deliver large molecules contrasts with currently described delivery methods that rely on diffusion, which drastically decreases in delivery with larger macromolecules [4-10]. We demonstrate rapid delivery into multiple cell types of a variety of molecule types and sizes, including dextran (4-2000 kDa), plasmids, mRNA, nanoparticles, and even 100 nm beads. Thus, this new phenomenon of cell volume exchange under ultrafast mechanical deformation enables a multitude of highly valuable cell engineering processes.

In brief, this thesis will begin by experimentally determining the governing parameters of cell VECT. Then we will investigate the intracellular delivery capabilities and physiological impacts on the cell caused by cell VECT. Finally we will apply this intracellular delivery technique to multiple applications of interest in both research and clinical settings. The ultimate goal of the proposed thesis is to gain an understanding of the mechanisms behind cell VECT, characterize its delivery capabilities and physiological effects on cells, and investigate and optimize the microfluidic device design and operating conditions for intracellular delivery in a number of clinical and research use cases. Using our cell deformation mechanics and intracellular delivery studies, we will explore the mechanisms of cell VECT and its effectiveness for useful applications, including intracellular analysis and gene engineering. These objectives will be carried out in the following aims.

2.2   Aim 1: Governing Parameters of Cell VECT

We hypothesize that rapid onset and duration of mechanical compressions of cells can cause a transient cell volume loss, followed by volume recovery. This phenomenon of

cell volume exchange can be utilized for convective transfer of large macromolecules to the cell interior. This aim seeks to characterize the mechanisms and governing parameters of the cell volume loss and recovery phenomenon during cell VECT. Specifically, we will study cell physical properties, including size and viscoelastic properties; device characteristics, such as the magnitude and number of compressions; and experiment parameters like flow rate and cargo concentration. We aim to determine the effects of these parameters on cell volume exchange and intracellular delivery.

2.3   Aim 2: Delivery Capabilities and Cell Physiological Effects

We hypothesize that the volume exchange phenomenon during cell VECT results in intracellular delivery mechanism that is convective and therefore not governed by diffusive limitations on transport of large molecules. This purely mechanical intracellular delivery method would also be independent of endocytic pathways. This aim seeks to experimentally determine the intracellular delivery capabilities and the physiological impacts on the cell due to cell VECT. In particular, we will investigate the size and amount of target molecules that can be delivered. We will study the intracellular localization of delivered molecules, and specifically examine whether delivery is endosomal. We will also determine the effects of rapid compressions on cell nuclear envelop integrity, viability, and protein loss.

2.4   Aim 3: Applications for Cell Engineering

We hypothesize that the convective nature of cell VECT delivery enables this method to be used to deliver a wide variety of target molecules to virtually any human cell type of interest for useful applications in cell engineering and analysis. Therefore, we direct our intracellular delivery studies to the specific applications of intracellular gene expression analysis, temporary cell transfection, and gene editing. The primary goal of this aim is to present proof-of-concept validation to demonstrate the utility of cell VECT for multiple applications that are useful in clinical and research settings.

2.5   References

[1]   Wang, G. *et al.* Microfluidic cellular enrichment and separation through differences in viscoelastic deformation. *Lab Chip.* **15**, 532-540, doi:10.1039/c4lc01150c (2015).

[2]   Wang, G. *et al.* Stiffness dependent separation of cells in a microfluidic device. *PLoS One.* **8**, e75901, doi:10.1371/journal.pone.0075901 (2013).

[3]   Wang, G., Turbyfield, C., Crawford, K., Alexeev, A. & Sulchek, T. Cellular enrichment through microfluidic fractionation based on cell biomechanical properties. *Microfluid. Nanofluid.* **19**, 987-993, doi:10.1007/s10404-015-1608-y (2015).

[4]   Sharei, A. *et al.* Cell squeezing as a robust, microfluidic intracellular delivery platform. *J. Visualized Exp.*, e50980, doi:10.3791/50980 (2013).

[5]   Sharei, A. *et al.* Plasma membrane recovery kinetics of a microfluidic intracellular delivery platform. *Integr. Biol.* **6**, 470-475, doi:10.1039/c3ib40215k (2014).

[6]   Hallow, D. M. *et al.* Shear-induced intracellular loading of cells with molecules by controlled microfluidics. *Biotechnol. Bioeng.* **99**, 846-854, doi:10.1002/bit.21651 (2008).

[7]   Sharei, A. *et al.* Ex vivo cytosolic delivery of functional macromolecules to immune cells. *PLoS One.* **10**, e0118803, doi:10.1371/journal.pone.0118803 (2015).

[8]   Szeto, G. L. *et al.* Microfluidic squeezing for intracellular antigen loading in polyclonal B-cells as cellular vaccines. *Sci. Rep.* **5**, 10276, doi:10.1038/srep10276 (2015).

[9]   Ding, X. *et al.* High-throughput nuclear delivery and rapid expression of DNA via mechanical and electrical cell-membrane disruption. *Nat. Biomed. Eng.* **1**, 0039, doi:10.1038/s41551-017-0039

[10]   Saung, M. T. *et al.* A Size-Selective Intracellular Delivery Platform. *Small.* doi:10.1002/smll.201601155 (2016).

CHAPTER 3.   GOVERNING PARAMETERS OF CELL VECT

3.1   Introduction

Studies of the physical response of cells to deformation using micropipettes, microcantilevers, and microfluidic manipulations have shown that cells subjected to significant deformations of up to 85% strain applied across a range of timescales from ~10 µs to >1 s have the ability to recover to their pre-deformation shape [1-10]. Studies of cells compressed by micropipette aspiration have reported cell volume loss, but have not quantified the time scale at which volume loss occurs or characterized the phenomenon of cell volume recovery to return to pre-compression volume [9,10].

High speed imaging of flow-through microfluidics observe large strain deformations and recovery from compressions at time scales <1 ms [1,11,12]. Cells were observed to recover to their previous volume and shape as cells relax upon leaving the compression. We studied whether this phenomenon can deliver extracellular liquid and target molecules into the cell on convective fluid currents. We will investigate the conditions and parameters of compressions that cause a transient exchange of fluid and macromolecules between the cell interior and its surroundings for intracellular macromolecule delivery [13-15]. We find the transition of timescales from slow compression to fast compression that leads to the volume change phenomenon, the subsequent cell volume recovery behavior, and the dependence on compression parameters and cell biomechanical properties. We characterize the biomechanical mechanisms of cell volume exchange, specifically investigating the dependence of cell volume exchange on compression parameters, cell relaxation, and cell physical properties.

3.2   Investigation of Cell VECT Mechanism

We investigate the governing parameters of transient and significant (up to 30%) cell volume change in response to large magnitude deformations with ultrafast timescales (~10 μs). We attained fast deformations by rapidly flowing cells through microfluidic constrictions with an abrupt, stepwise compression profile. To characterize this new behavior, we employed high speed video microscopy and quantitative fluorescent marker delivery to investigate cell deformation, volume loss, and recovery.

3.2.1   *Microfluidic Cell Deformation Causes Cell Volume Loss*

Cell deformation was caused by flowing cells through a microfluidic channel containing a multitude of ridges with rectangular cross-sectional profiles to precisely and repeatedly exert abrupt and brief compressions upon the cells. Hydrodynamic forces maintained high cell velocity throughout multiple constrictions, while the angled ridges cleared dead cells and clusters of cells which could cause occlusions [16-18]. As cells encountered the rectangular ridges, abrupt shape change was observed as cells compress under the ridges to conform to a gap that is smaller than their relaxed diameter (Figure 3.1A). Cell compression time is the measurement of the amount of time the cell takes to traverse the steep edge of the ridge (<1 μm as determined by optical profilometry) at the measured cell velocity (~100 mm/s). During this time, cells were observed to deform vertically, perpendicular to the direction of flow, by up to 50% of the cell diameter, for a vertical deformation velocity on the order of 1 m/s. In contrast, diffusive mechanoporation methods use gradual constrictions that deform cells over the course of approximately 50 μm (as opposed to the <1 μm steep edge of our rectangular ridges), which results in a

vertical deformation velocity at least an order of magnitude slower, or <0.1 m/s vertical deformation velocity [19]. The sudden shape change caused by the abrupt deformation structure of the rectangular ridge was quantitatively characterized by high speed video microscopy and analysis (Figure 3.1B).
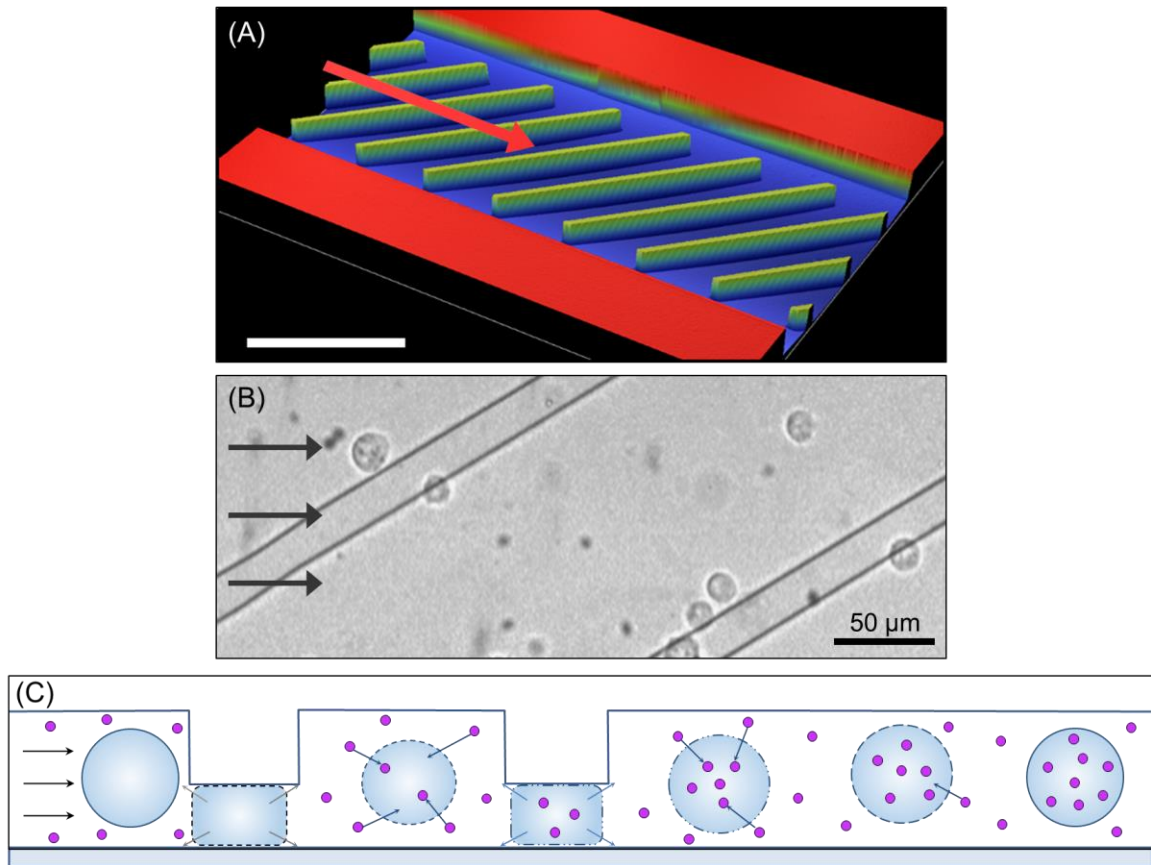
Figure 3.1: Overview of microfluidic device and volume exchange. (A) Profilometric image of the microfluidic channel layout with diagonal ridges. The arrow indicates cell flow direction. (B) Light microscopy image with overhead view of K562 cells flowing through the microchannel and passing under ridges. (C) Cross-sectional view of a cell undergoing compression under the ridges and relaxation, illustrating volume exchange and molecule uptake.

The volume reduction of compressed cells indicated that a portion of cytosol was expelled from the cell interior through a mechanically compromised cell membrane. Cell volume recovery, on the other hand, requires extracellular fluid to enter the cell. Since the video analysis does not allow us to evaluate cell volume recovery in between the ridges, we characterized the dynamics of volume exchange and fluid transfer through the compromised cell membrane using fluorescently labeled dextran (Sigma-Aldrich) as a tracker molecule. Dextran of various sizes was added to the cell suspension immediately before compression experiments. We hypothesized that cell relaxations after each compression will cause the extracellular fluid to enter the cell interior transporting suspended fluorescent molecules, and that the molecules will partially remain in the cell interior after consecutive compressions and cell recovery, serving as an indicator of volume exchange (Figure 3.1C). Shortly after compression, the cell membrane undergoes repair to reestablish membrane integrity at a rapid time scale, seconds to minutes, after permeabilization [19].

Using a computational cell deformation model [17] combined with area analysis of high speed videos of individual cells in the microfluidic channel, we evaluated the change in cell volume at several points in the channel (Figure 3.2A). Measurements were taken of K562 myelogenous leukemia cell area before compression, and then when entirely constrained under each ridge (Figure 3.2Bi). Before compression, each cell was approximated as an ellipsoid, while the cell shape under each ridge was approximated to a truncated ellipsoid, as determined by a cell deformation model [17] (Figure 3.2Bii,iii). The compressed cell height was equal to the ridge gap, which was independently measured by

profilometry. Due to the uncertainty of cell shape and orientation between ridges, the cell volume between ridges cannot be deduced from its area measurement.
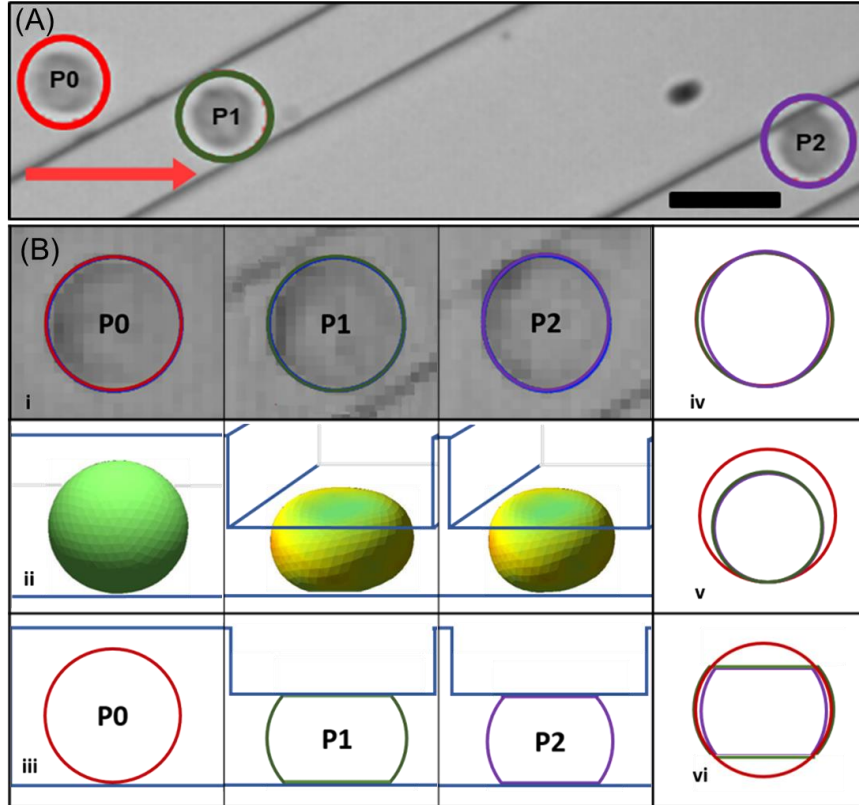
Figure 3.2: Overview of cell volume change measurement. (A) Overlay of the same K562 cell (outlined) at multiple positions passing through the ridges. (B) Image analysis of the area of a single cell inside the device. The schematic diagram of a cell at (i) the captured top view at each respective position; (ii) three dimensional schematic representation of the cell at positions before and during compression under first two ridges (iii) approximation of the side view of the cell based on channel height at the corresponding positions; overlaid view of the cell at different positions (iv) top view; (v) spherical projection of cells with same volume as uncompressed and compressed conditions and (vi) side view.

Assuming a known gap and modeled cell shape, we determined the cell volume before and during compressions. An overlay of cell area measurements at the various

positions shows subtle area change, suggesting that the vertical constraint from the ridge mainly accounts for the volume change (Figure 3.2Biv). A view of spherical cells with the same volume as the compressed cells visualizes the volume change when projected on the pre-compression cell (Figure 3.2Bv). Cells exhibited the most significant volume decrease at the first ridge due to the sudden change in shape from ellipsoid to truncated ellipsoid (Figure 3.2Bvi).

Using the described methods to measure cell volume , we were able to determine the effects of different compression parameters on cell volume loss. Decreasing the ridge gap size of the microfluidic device, that is the space between the ridge and the bottom of the microfluidic channel through which the cells must compress, led to a greater volume decrease between the pre-compression cell and the cell compressed under the first ridge (Figure 3.3A). The cell volume proceeded to slightly decrease with each subsequent compression to a plateau volume after approximately 8 ridges (Figure 3.3B). We experimentally observed that increased compression strain from smaller ridge gaps resulted in higher delivery of fluorescent molecules (Figure 3.3C). The measured delivery to cells with smaller ridge gap size (5.6 μm) was confounded at the conditions tested due to cells flowing around the ridges rather than passing through the smaller gap underneath the ridges. Ridges with gaps larger than the K562 cell diameter (14.5 ± 1.5 μm) did not cause volume change, and showed lower delivery of 2000 kDa FITC-dextran macromolecules (Figure 3.3C) in a manner consistent with existing studies that used fluid shear mechanoporation to induce membrane pores, allowing diffusive delivery of molecules [17,20]. Increasing ridge gap size from 16 μm to 20 μm resulted in low amounts of dextran delivery, but ridge gaps smaller than the cell diameter significantly increase delivery in a

manner that increased with smaller ridge gap sizes. Therefore, a ridge gap smaller than the

relaxed cell diameter can be identified as a threshold at which delivery behavior changes.
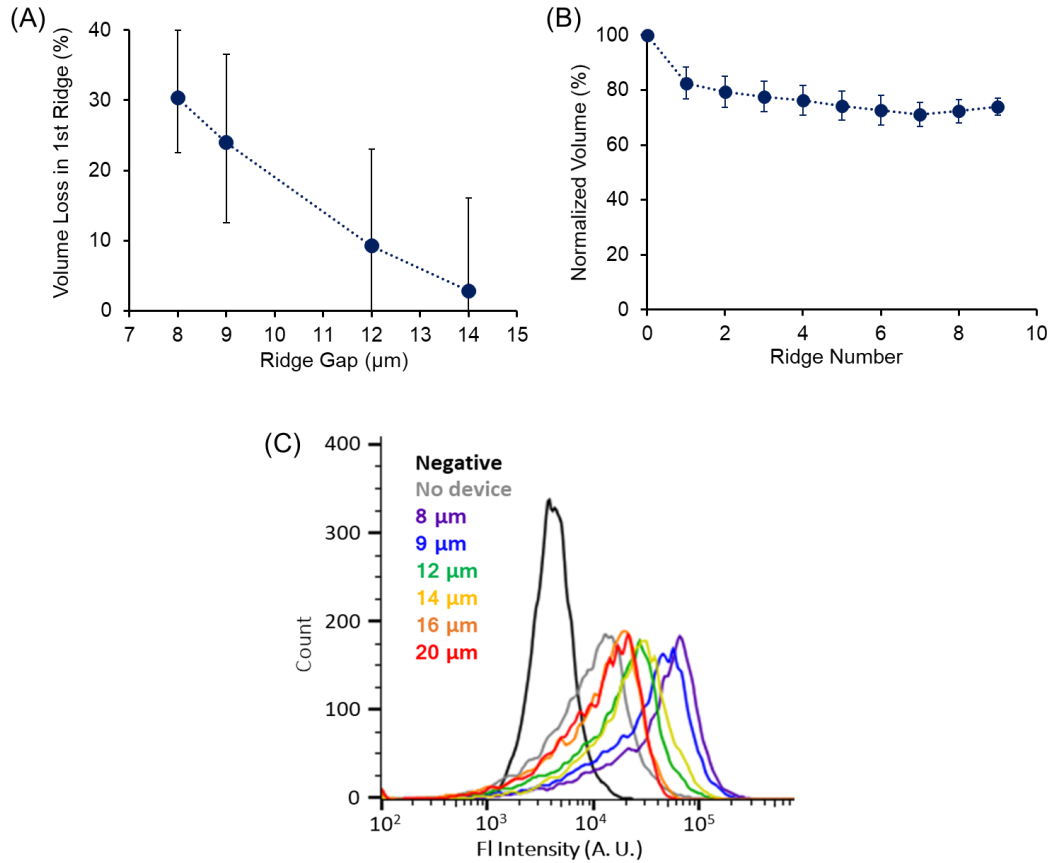
Figure 3.3: Impact of compression strain on volume loss and intracellular delivery.
(A) Percent of cell volume lost under the first ridge increased with smaller device ridge
gap, n>250, bars are interquartile range. (B) Normalized volume of cells at different ridge
positions in the channel, n≥45, bars are standard deviation. (C) Intracellular delivery of
2000 kDa FITC-dextran (0.3 mg/mL) increased with smaller size of ridge gap through
which cells pass. K562 cells were used for this study.

3.2.2   Faster Compression Time Scale Causes Greater Volume Loss

Cells were flowed through the ridged microchannel at varying flow rates to observe

the effects of compression rate on cell volume change. Flow rate through the microchannel

33

was varied from 3.5 mm/s to 275 mm/s with high speed video recording to observe cell responses during mechanical compression. A compression ridge gap of 9 μm, previously characterized to cause volume change in K562 myelogenous leukemia cells, was used for this study [14]. Using a cell deformation model combined with area analysis of high-speed videos of individual cells in the microfluidic channel, we calculated the compressed cell volume under the first ridge compared to the volume of the ellipsoid cell before compression [17].

At low flow rates, cells were observed to expand in area perpendicular to compression when deformed underneath the ridge (Figure 3.4A,B). At higher flow rates, cells did not exhibit area expansion under the ridge (Figure 3.4C,D) yet were substantially slowed down by the ridges. As flow rate increases, the cell area expansion decreases, eventually approaching no area change compared to the uncompressed cell (Figure 3.4E). This cell area expansion results in overall conservation of cell volume at slow flow rates, but high flow rates cause cell volume loss (Figure 3.4F). This behavior suggests that, as cells undergo more rapid compressions, they are unable to expand under the ridge, resulting in increased volume loss. This trend plateaued at the highest flow rates we tested, wherein the cells appeared to maintain the same area under the compression compared to before compression, indicating a maximized volume change for that compression ridge gap size of 9 μm.

We characterized the effects of compression rate on overall cell volume exchange by using 2000 kDa FITC-dextran (Sigma-Aldrich) as a molecular tracer. Flow cytometry results from these experiments indicated that intracellular delivery of FITC-dextran

increased with faster compression rate (Figure 3.4G). Therefore, increased cell volume loss due to faster compression results in greater intracellular delivery.
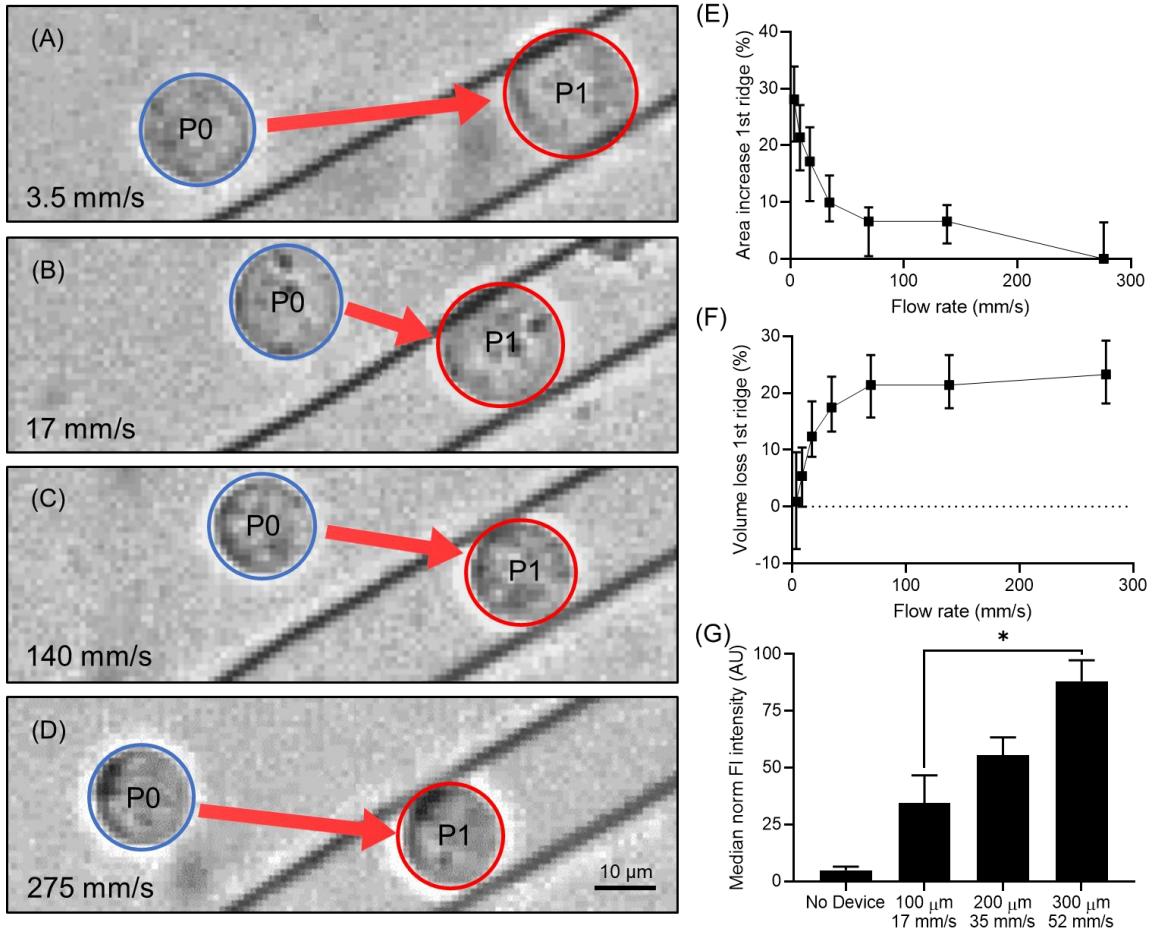
Figure 3.4: Analysis of cell response to compression time scale. K562 cells in 9 μm ridge gap device. (A) Cells at the slowest flow rate, 3.5 mm/s, exhibit visible area expansion between P0 (before the first compression) and P1 (under the first compression). (B) Area expansion is diminished but still visible at 17 mm/s. (C) As flow moves faster, 140 mm/s, cell area expansion decreases until (D) at 275 mm/s the area under the ridge remains the same compared to before the ridge. (E) Plot of cell area increase percentage compared to before the cells enter the ridge as a function of fluid flow rate. $N \approx 150$ cells, bars represent interquartile range. (F) Plot of cell volume loss percentage under the first ridge as a function of fluid flow rate. $N \approx 150$ cells, bars represent interquartile range. (G) Intracellular delivery of 2000 kDa FITC-dextran increased with compression rate. Cell recovery time between ridges is kept constant by scaling inter-ridge spacing with flow rate. *$P < 0.05$, $N = 3$ experiments, bars represent standard deviation. Devices with 7 ridges were used to avoid saturation or maximization of delivery that would otherwise obscure the effects of compression rate. No Device controls were exposed to the FITC-dextran without being processed by the device.

In order to understand the physical basis of the time scales of cell responses, it is intriguing to note that the T_c at which the cell is unable to expand transverse to applied force is of the same order of magnitude (~2 ms) as the time scale of mechanical signal transmission in the viscoelastic cytoskeleton (~1 ms) [21]. It is possible that when the cell is compressed with T_c approaching the time scale of mechanical stimulus transmission in the cytoskeleton but slower than that of the cytoplasm, the internal fluid pressure increases rapidly. Since the membrane is assumed to be held by the cytoskeleton, which cannot respond to deformation, the result of the increased pressure is fluid going through the membrane. On the other hand, for lower deformation speeds, both fluid and cytoskeleton can respond, and the cell volume is conserved. We therefore hypothesize that rapid deformation necessitates that the cell loses some of its volume to accommodate the compression time scale.

3.2.3   *Relation Between Volume Loss and Cell Physical Properties*

To better understand the physical mechanisms that govern cell VECT, we investigated the effect of cell physical properties, including cell size, elasticity, and viscosity, on volume change. At constant compression ridge gap size, we observed that larger cells exhibited increased volume loss at every flow rate tested. At slower flow rates we observed a broader distribution of cell volume change behavior based on cell diameter (Figure 3.5A). At faster flow rates the cell volume change shows a stronger correlation with size (Figure 3.5B). These observations suggest that cell volume change is highly dependent on cell size at faster flow rates. However, at slower flow rates, other cell physical properties, like cell viscosity or elasticity, could dominate.

To test the impact of cell elasticity on volume change, high speed video analysis was performed on K562 cells treated using a cytochalasin-D (CD) protocol previously characterized to lower the cell Young's Modulus from 0.40 ± 0.22 kPa to 0.21 ± 0.061 kPa.[17] However, CD treatment did not exhibit a statistically significant impact on cell volume loss at two different flow rates and concentrations of CD (Figure 3.5C,D). Similarly, a study of cells treated with 20 μM blebbistatin to reduce Young's modulus also did not show a statistically significant change in cell volume loss at multiple flow rates (Figure 3.5E) [22,23]. Therefore we conclude that these changes in cell Young's modulus using CD and blebbistatin did not significantly impact volume loss.
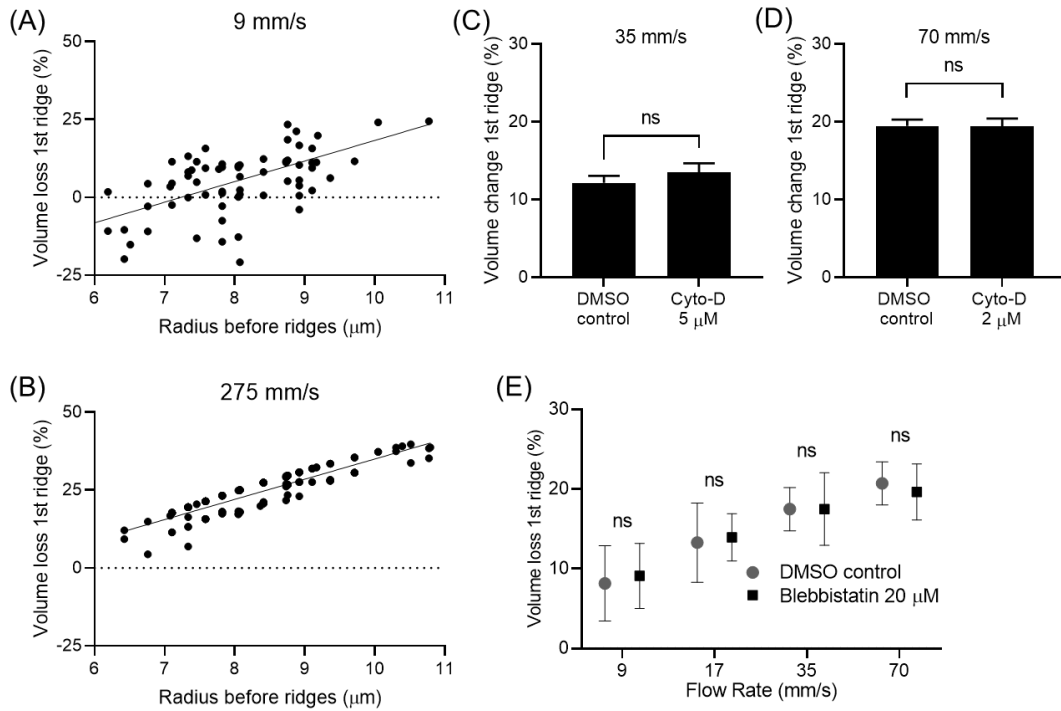
Figure 3.5: Investigation of effects of Young's Modulus changes on cell volume change. K562 cells in 9 μm gap device. (A) At slow flow rate, cell volume change has a broad distribution in relation to cell area. $N \approx 150$ cells, linear regression $R^2 = 0.319$ (B) At fast flow rate, volume change shows strong correlation with cell size. $N \approx 150$ cells, linear regression $R^2 = 0.819$ (C,D) Treatment of K562 cells with CD to decrease cell Young's modulus did not have a significant impact on cell volume change. $N = 50$, bars

37

represent SD, P > 0.34. (E) K562 cells were treated with 20 μM blebbistatin to decrease cell Young's modulus. 9 μm gap devices used. Bleb inhibition was observed after the 1 hour treatment. Blebbistatin treatedment did not have a significant impact on cell volume loss at multiple flow rates. N = 25, bars represent SD, P > 0.22.

The cell viscoelastic creep response has been shown to play an important role in transducing in-plane stresses to out-of-plane stresses and deformations [9,10,24]. Therefore we explored viscosity as a governing factor of cell volume change response by comparing HL-60 promyelocytic leukemia cells to K562 cells. HL-60 cells were characterized by AFM to have higher viscosity and Young's modulus than K562 cells (Figure 3.6, Table 3.1) [16].
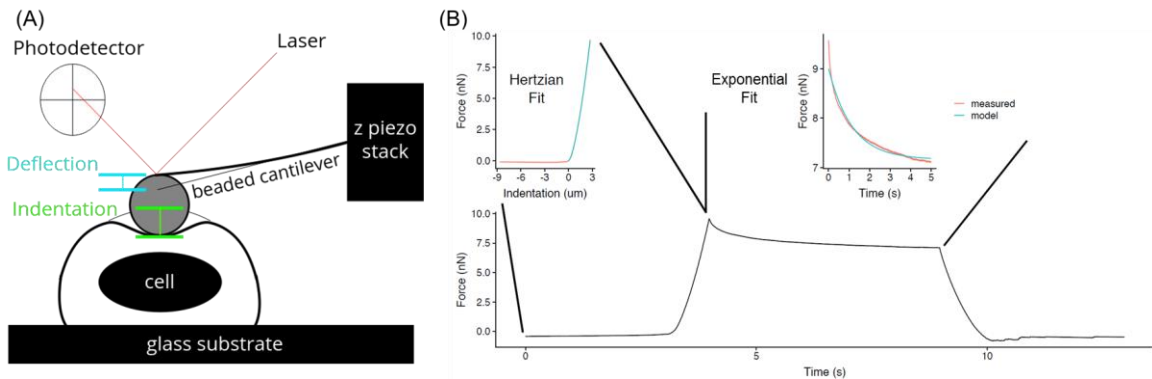
Figure 3.6: AFM measurement of cell mechanical properties. (A) Schematic of AFM detection of a laser reflected off a deflected cantilever. The cantilever bends when brought in contact with a sample, causing the laser spot on the photodetector to move. Cell indentation can be extracted by subtracting the amount of deflection by the position of the back of the cantilever. (B) The initial aproach portion of the force curve was fit to the Hertzian contact model to calculate cell Young's modulus. The dwell portion of the force curve was fit to an exponential decay curve to extract the viscous rate constant.

	K562	K562F	HL-60	HEY	OVCAR
Mean viscous rate constant T_v^{-1} [s^{-1}]	17.7	47.5	8.91	0.99	0.77
Viscous rate constant SD [s^{-1}]	13.7	27.9	4.6	0.11	0.11
Number of cells measured	69	42	63	100	90
Mean viscous time constant T_v [s]	0.056	0.021	0.112	1.01	1.3
Mean Young's modulus [kPa]	0.40	23	0.86	0.38	0.60
Young's modulus SD [kPa]	0.22	13	0.22	0.20	0.31

Table 3.1: Table of AFM measurements of cell mechanical properties. Measurements were obtained using the methods outlined in Figure 3.6. Values for K562, K562F and HL-60 cells were taken from published AFM data [16,17].

Studies have shown that cells increasingly behave as a viscous material at faster deformation rates [25,26]. Video analysis of cells deforming under the first microfluidic ridge determined that both K562 and HL-60 cells decrease in translational velocity relative to the surrounding fluid flow when under the ridge (Figure 3.7A). The K562 and HL-60 cell experiments were controlled for flow rate and cell size to subject the cells to the same magnitude and rate of compression. Yet the two cell types demonstrated different volume change behavior. We found that at slow flow rates, more viscous HL-60 cells did not expand in area perpendicular to the compression as much as K562 cells, and therefore showed higher volume change (Figure 3.7B). As flow rate increases, the volume change of the two cell types converge, suggesting cells of comparable size lose similar volume at faster flow rates.

To further test the hypothesis that cell viscoelastic properties govern cell area expansion and volume loss during compression, we characterized the deformation response of K562 cells crosslinked with formaldehyde. Treatment of K562 cells with 4% formaldehyde for 30 mins at room temperature has been shown to significantly increase

Young's modulus and decrease viscosity [16,17]. Therefore, formaldehyde-treated K562 cells (K562F) exhibit more elastic and less viscous behavior. We observed that K562F cells exhibited more area expansion and less volume change than untreated K562 cells at the same fluid flow rates (Figure 3.7C). Modifications to viscoelastic properties in K562F cells also shift the time scale at which volume change occurs. K562F cells required a faster compression time scale than untreated K562s in order to achieve the same volume change (Figure 3.7D). For example, in order to reach 50% of maximum cell volume exchange, untreated K562 cells must be compressed at compression time $T_c \approx 0.0035$ sec, while K562F cells require $T_c \approx 0.0016$ sec, about twice the compression speed. Therefore, K562F cells exhibited more elastic behavior, expanding more under the ridge and therefore losing less volume than untreated K562s at the same compression rates.

More viscous cells exhibit slower out-of-plane expansion during both the onset and duration of deformation, while elastic cell behavior is characterized by rapid expansion.[7,9,10,27-29] These observations suggest that cells with higher viscosity exhibit less expansion in the initial elastic phase and slower expansion during the viscoelastic creep phase. Studies have shown that cells behave as more viscoelastic materials during fast deformation [30-32]. With slower deformation, cells behave as more elastic materials [30,32-35]. This results in cells at high flow rates exhibiting more viscous behavior with less expansion orthogonal to compression, while cells at slower flow rates would behave as an elastic material with increased expansion.
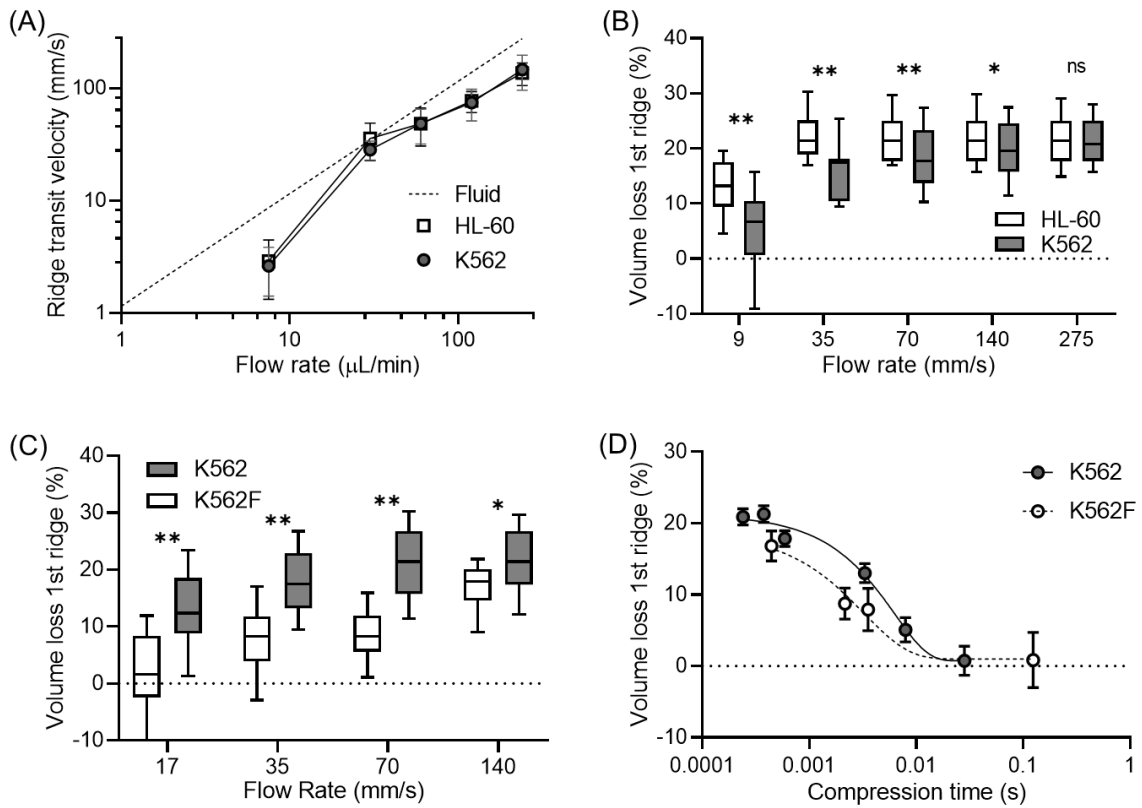
Figure 3.7: Effects of cell viscosity on cell volume change. 9 µm gap devices used. (A) Both K562 and HL-60 cells slow down relative to the surrounding fluid flow when they interact with the first ridge. (B) Highly viscous HL-60 cells show more volume loss at slow flow rates compared to K562 cells. As flow rate increases the volume change converges. **$P < 0.0001$, *$P < 0.005$, $N \approx 100$ cells, whiskers represent 10-90 percentile, 9 µm gap devices used. (C) K562 cells were treated with 4% formaldehyde for 30 mins at room temperature to increase cell Young's modulus and decrease cell viscosity. Formaldehyde-treated K562 cells (K562F) exhibited a statistically significant decrease in volume loss compared to untreated cells at the same fluid flow rates. **$P < 0.00001$, *$P < 0.01$. $N \geq 25$, whiskers represent 10-90 percentile. (D) K562F cells required a faster compression time scale than untreated K562s in order for the same volume loss to occur. $N \geq 25$, lines represent best fit to a sigmoidal function.

We visualize this behavior in an illustration (Figure 3.8A,B) and qualitative plot of out-of-plane expansion for a more viscous and less viscous cell, based on a model of the cell as a viscoelastic solid consisting of an elastic cortical shell surrounding a viscous fluid (Figure 3.8C) [10,29]. Therefore, at faster compression due to high flow rate, cells exhibit

41

more viscous behavior. At slower compression due to low flow rate, cells exhibit elastic behavior. A more viscous cell would be expected to exhibit less expansion and therefore more volume loss than a less viscous cell.
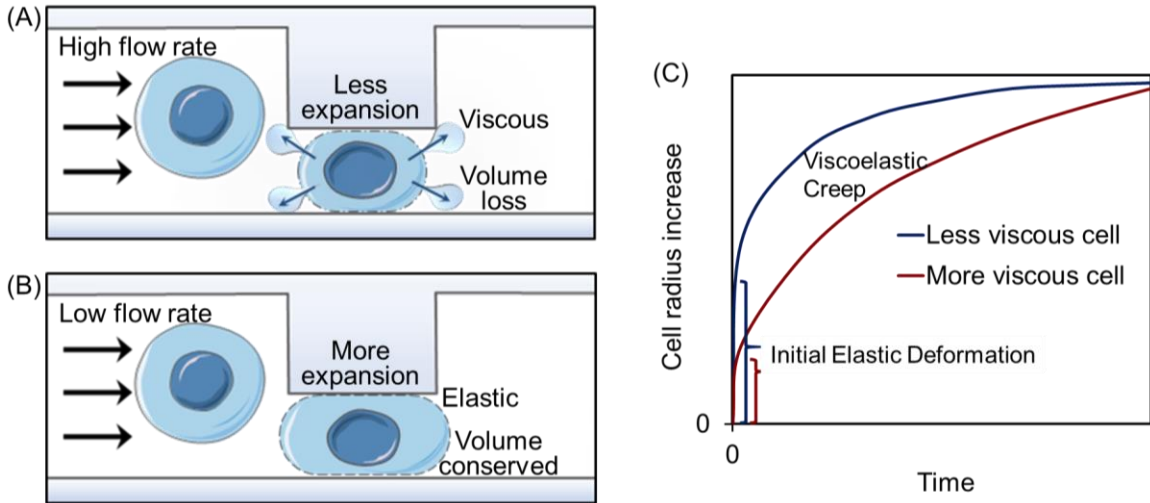
Figure 3.8: Cell viscoelastic behavior changes with compression rate and impacts volume loss. (A) Cells at high flow rate faster onset and duration of deformation, resulting in more viscous behavior, reduced expansion, and therefore more volume loss. (B) Cells at low flow rate compress slower with longer duration of compression, allowing for elastic expansion behavior and volume conservation. (C) Qualitative plot of cell out-of-plane expansion behavior during deformation. Cells undergo an initial, fast elastic deformation phase followed by a slower, viscoelastic creep phase. More viscous cells exhibit less initial elastic expansion and slower viscoelastic creep than less viscous cells.

A dimensionless parameterization of the forces involved in the cell compression behavior will allow us to contextualize the interactions between external forces and cell mechanical properties that result in cell volume loss. To parameterize inertial force divided by viscous force, we calculate a Reynolds number (*Re*) for the vertical compression of multiple cell types with mechanical properties measured by AFM using the following definition: $Re = \frac{F_I}{F_V} = \frac{\rho V L}{\mu}$. However, a plot of *Re* did not produce a single trend of

correlation between Re and volume change among multiple cell types (Figure 3.9A). A dimensionless ratio of inertial force to elastic force was also calculated using the following definition: $\frac{F_I}{F_E} = \frac{\rho V^2 L^2}{E\,A}$, where ρ = density, V = vertical cell compression velocity, L = cell diameter, μ = cell viscosity, E = Young's modulus, A = cell area, but this dimensionless number also did not converge to a single trend for multiple cell types. (Figure 3.9B). Therefore, it appears that the volume change behavior of multiple cell types over different compression rates is not well explained by considering viscous and elastic forces individually.
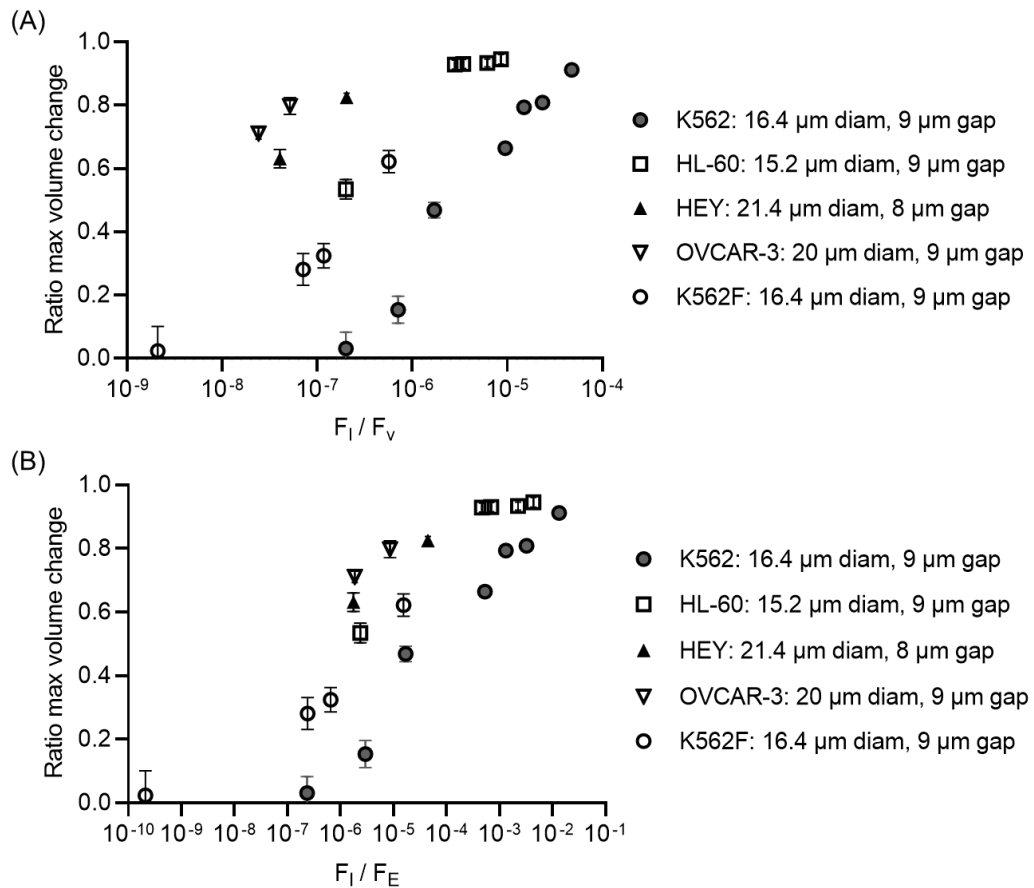
Figure 3.9: Dimensionless ratios of inertial force to viscous and elastic force. (A) Reynold's number (ratio of inertial force to viscous force) was calculated for multiple cell types and compression rates. A plot of Re did not show a consensus trend for volume

43

change for multiple cell types at various flow rates. (B) The ratio of inertial force to elastic force was calculated for multiple cell types and compression rates. A plot of F_I/F_E similarly did not exhibit a single trend of correlation with volume change. Variables are defined as ρ = density, V = vertical cell compression velocity, L = cell diameter, μ = cell viscosity, E = Young's modulus, A = cell area. N $\geq$ 25, bars represent standard error.

We next evaluated the observed cell behavior by considering the combined effects of cell viscosity, elasticity, and compression rate on the resultant volume change. The relation between cell viscosity and elasticity during deformation is parameterized using the dimensionless Ericksen number (*Er*), which determines the relation between viscous and elastic forces (Equation 3.1) [36,37].

$$\textbf{Ericksen number} = \frac{\textbf{Viscous force}}{\textbf{Elastic force}} = \frac{\mu V L}{E\,A} = \frac{T_v}{T_c}\frac{\Delta L}{A}\,L \qquad\qquad (3.1)$$

The cell is modeled as a Maxwell viscoelastic material with dynamic viscosity $\mu = T_v\,E$, [38-40] where E is the Young's Modulus and T_v is the viscous time constant as measured by AFM (Table 3.1). Viscous force is dependent on cell compression velocity (V = $\Delta L/T_c$ where T_c is the compression time measured by video analysis) and a characteristic length (L is the relaxed cell diameter, ΔL = L – compression gap). The elastic force is defined by Young's Modulus and A, cell area.

At slow flow rates, and therefore low *Er* values, the cell exhibits elastic deformation behavior, expanding in area during initial compression [9,10,30,32-35]. The slow flow rate also results in longer duration of compression, so the cell also expands transversely due to viscoelastic creep, resulting in volume conservation. Higher flow rates result in larger *Er* values, wherein the cell enters a viscoelastic behavior regime during compression onset

44

that causes decreased initial elastic deformation [30-32]. In addition, the shorter duration of compression allows less time for viscoelastic creep expansion during compression, resulting in an overall decrease in cell volume [5,9,10].

We find that several cell types follow the same sigmoidal trend of volume change dependence on Ericksen number, as determined by nonlinear regression performed on data points from multiple leukocyte and epithelial cell lines (Figure 3.10). To account for differences in cell size and compression gap in these data, we examined a ratio of the observed cell volume change and the maximum attainable volume change, where the cell does not expand in area during compression.
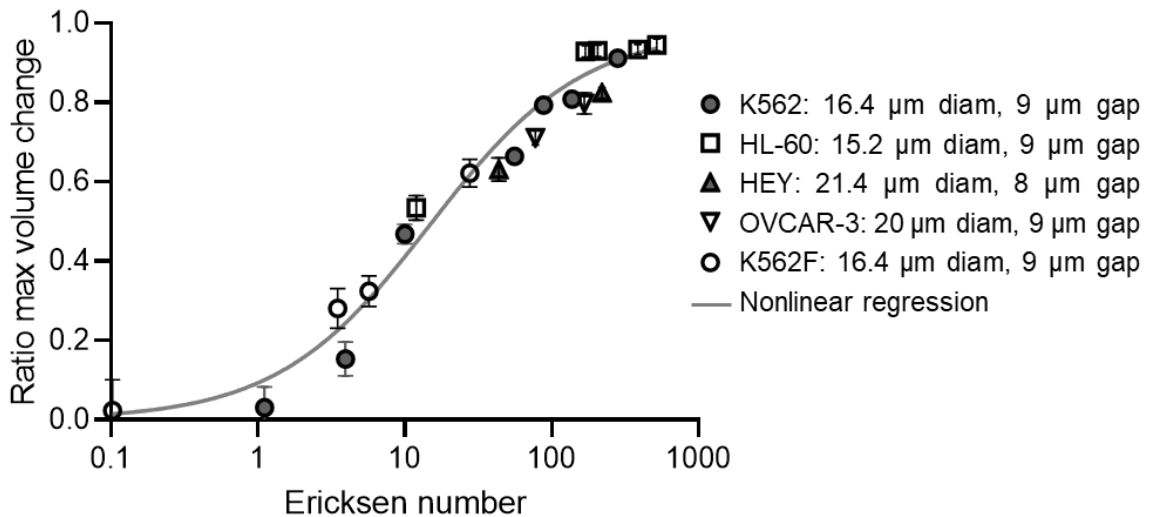
Figure 3.10: Ericksen number as a dimensionless parameterization of cell volume loss. A plot of volume change for multiple cell types shows sigmoidal relation with Ericksen number (*Er*). Cell types include leukocyte cell lines K562, HL-60, and formaldehyde-treated K562F, and epithelial cell lines HEY and OVCAR-3. $N \geq 25$, bars represent standard error.

At conditions in which Er >>1, in which cell volume change occurs, we observe that the time scale (T_c) at which cells transition from fully uncompressed to fully compressed under the first ridge is significantly faster than the cell viscous time constant (T_v). At these conditions, the cell must deform very rapidly and does not demonstrate the area expansion that was observed at small Er conditions. In the cell behavior regime of rapid deformation ($T_c \ll T_v$), cells are forced to compress at a time scale too fast for cytoplasmic remodeling and mechanical stimulus transmission to occur [21].

In order to understand the physical basis of the time scales of cell responses, it is intriguing to note that the T_c at which the cell is unable to expand transverse to the applied force is of the same order of magnitude (~2 ms) as the time scale of mechanical signal transmission in the viscoelastic cytoskeleton (~1 ms) [21]. We hypothesize that when T_c approaches the time scale of mechanical stimulus transmission in the cytoskeleton, deformation occurs too quickly for the cytoskeleton to expand transverse to the compression. The cell membrane is also unable to undergo transverse expansion since it is attached to the compressed cytoskeleton. Therefore, the internal fluid pressure increases rapidly, and fluid leaves the cell as a result. On the other hand, for lower deformation speeds, both fluid and cytoskeleton have sufficient time to undergo transverse expansion, and the cell volume is conserved. Our findings suggest that rapid deformation necessitates that the cell loses some of its volume to accommodate the compression time scale.

The convergence plot of cell volume change behavior with relation to Ericksen number provides a dimensionless parameterization of cell volume loss in response to mechanical forces. The collapse of multiple cell types to a single trend of relation between volume change and Er suggests a primacy of both viscosity and elasticity in determining

46

the extent of volume change, which was not seen in other parameterizations. Therefore cell deformation behavior is governed by the viscoelastic properties of the cell as a whole, and cannot be fully characterized by only considering individual cell components alone. Various subcellular components, including the cytoskeleton and cytosol, can however be contributing factors to the viscoelastic mechanical response of the cell. When mechanical forces cause cells to deform at a time scale that exceeds the limits set by cell viscoelastic behavior, the cell undergoes permeabilization.

3.2.4   *Characterizing Volume Recovery through Molecular Delivery*

The volume reduction of compressed cells indicated that a portion of cytosol was expelled from the cell interior through a mechanically compromised cell membrane. Cell volume recovery, on the other hand, requires extracellular fluid to enter the cell. We characterized the dynamics of intracellular uptake of surrounding fluid volume and molecules through the compromised cell membrane using fluorescently labeled dextran (Sigma-Aldrich) as a tracker molecule. FITC-dextran (2000 kDa MW) was added to the cell suspension immediately before compression experiments. We deduced that cell relaxations after each compression will cause the extracellular fluid to enter the cell interior transporting dispersed fluorescent molecules, and that the molecules will partially remain in the cell interior after consecutive compressions serving as an indicator of volume exchange.

Based on the correlation between volume loss and molecule delivery, we hypothesized that altering the time that the cell relaxes as it moves between consecutive constrictions can affect the volume uptake and, therefore, molecular delivery. The

relaxation time between ridges was controlled either by varying the ridge spacing or the flow rate. We observed that increased flow rate resulted in decreased delivery, while the 200 µm spacing between ridges consistently resulted in higher delivery than the 100 µm spacing (Figure 3.11A). Therefore, the increased relaxation time between ridges led to greater delivery (Figure 3.11B), despite differences in flow speed and ridge spacing. We also observed that molecular delivery showed diminishing returns past a certain duration of cell relaxation between ridges (~1 ms), suggesting a saturation point of relaxation (Figure 3.11B). This result is in contrast with diffusive delivery, which increases with faster flow rates [41,42].
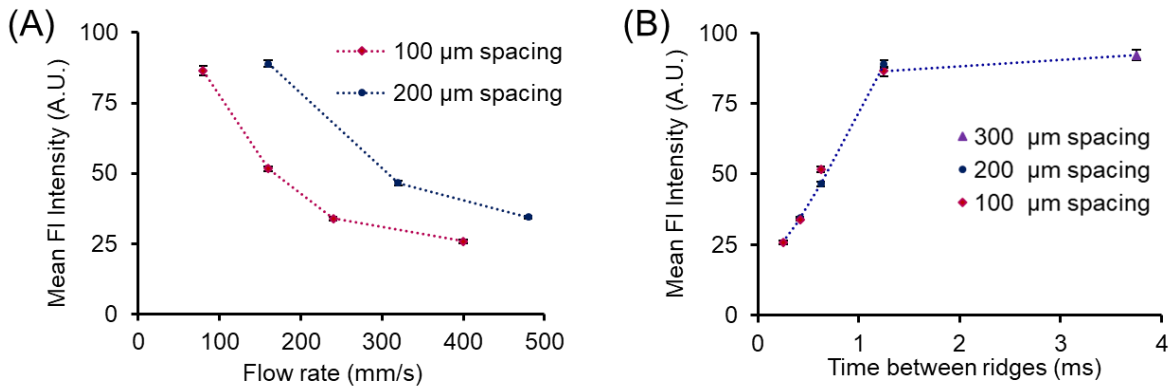
Figure 3.11: Characterizing cell volume recovery through molecule delivery. (A) Molecule delivery of 2000 kDa FITC-dextran (0.3 mg/mL) decreased with faster flow rate. However, 200 µm spacing between ridges consistently demonstrated higher delivery than 100 µm spacing across several flow rates. (B) Delivery increased with greater cell relaxation time between the ridges until a plateau was observed. (C) Molecule delivery was greater with increasing number of constrictions. The trend plateaued after 14 ridges. K562 cells with 9 µm gap devices were used.

3.2.5 More Compressions Increases Delivery

The use of multiple ridges causes repetition of cell volume exchange events. Increasing the number of ridges in the microchannel greatly increased molecular delivery to the cells. We observed a positive and non-linear correlation between the number of ridges and molecule delivery. This trend continued to a plateau, wherein devices with 14 ridges and 21 ridges demonstrated the same delivery for these experimental conditions (Figure 3.12). The overlap in delivered fluorescent molecule intensity at 14 and 21 ridges suggests that intracellular delivery has been maximized for these particular experimental conditions.
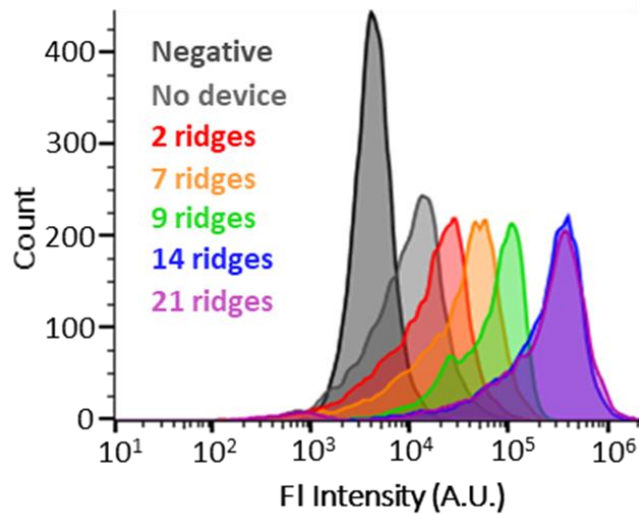
Figure 3.12: Impact of repeated compressions on molecule delivery. Molecule delivery of 2000 kDa FITC-dextran (0.3 mg/mL) was greater with increasing number of constrictions. The trend eventually plateaus, with 14 and 21 ridges showing the same fluorescence intensity profile of delivered fluorescent cargo molecules. K562 cells with 9 μm gap devices were used.

Based on these results, we hypothesize that each ridge compression event results in cell volume exchange, bringing the intracellular concentration of the target molecule closer to the extracellular concentration. By subjecting the cells to repeated volume exchange events by incorporating more ridges into the microfluidic device, we raise the intracellular target molecule concentration. Past a certain number of ridges, we no longer observe significant increase in delivery, suggesting that the intracellular concentration cannot be raised further based on the extracellular concentration.

3.2.6 *Delivery Occurs During Volume Exchange*

To determine the time scale at which delivery occurs during cell VECT, we designed an experiment to analyze the relative amount of delivery that occurs during the brief time (<0.1 s) of cell compressions inside the device channel and immediately after leaving the device. Delivery inside the channel was determined by flowing K562 cells through the channel with the target delivery molecules, 2000 kDa FITC-dextran, and then inhibiting delivery after the channel by immediately diluting the outlet sample into a molecule-free bath (Figure 3.13A). Delivery after the channel was isolated by flowing cells through the channel in the absence of target molecules, then exposing the cells to a molecule-rich bath immediately after leaving the channel (Figure 3.13B). Molecules were delivered to over 80% of cells during their <0.1 s transit through the channel, while only ~33% of cells exhibited delivery when provided dextran immediately after transit through the compressions, even after incubation in the outlet well for >10 minutes. A threshold set at the brightest 10% of the No Device control was used to define the lower bound of fluorescence for positive delivery (Figure 3.13C). The high delivery obtained primarily

50

during compressions inside the channel supports that cell VECT delivers large macromolecules by fluid exchange during compression and relaxation.
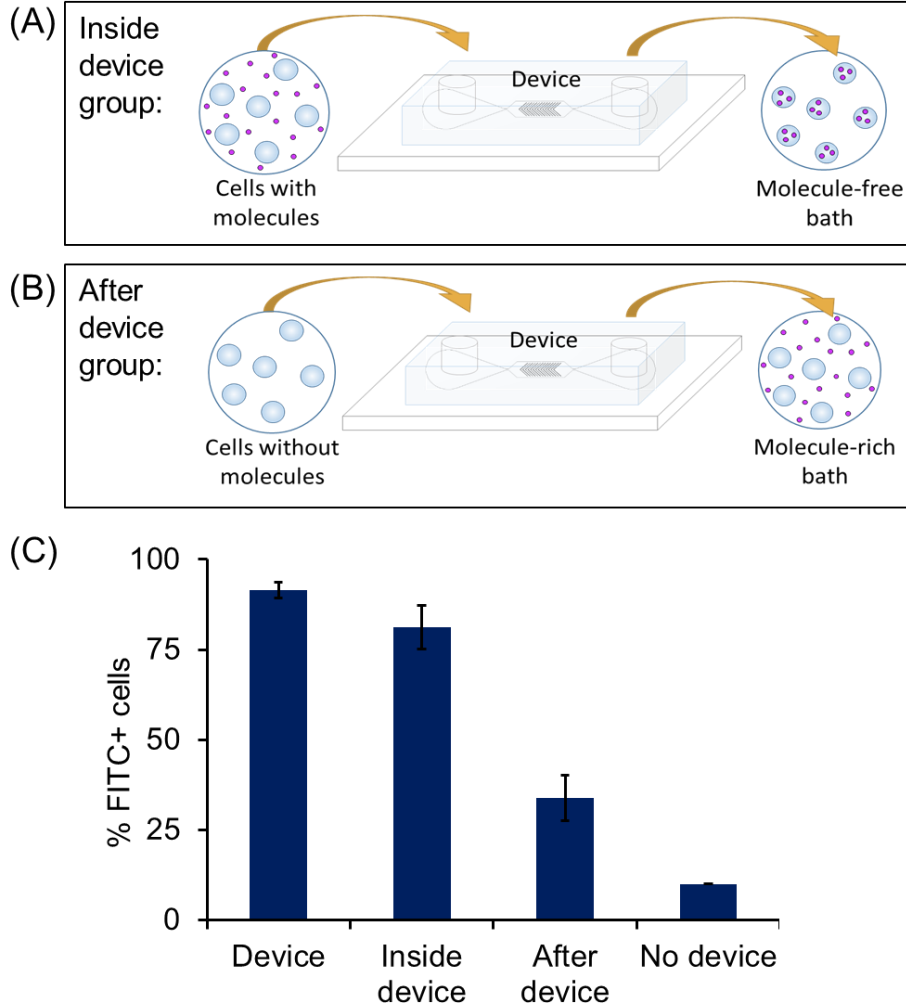
Figure 3.13: Study of intracellular delivery during and after compression. (A) Delivery during compression inside the device was isolated by flowing cells through the device in the presence of target molecules, then immediately plunging the cells into a molecule-free bath. (B) Delivery after compression was isolated by flowing cells through the device in the absence of target molecules, then plunging cells into a molecule-rich bath immediately after leaving the device. (C) Isolation of delivery inside the channel demonstrated that >80% of cells successfully uptake molecules during the brief time inside the channel. Only ~33% of cells showed delivery after incubating in a molecule-rich bath upon leaving the device, n = 3. K562 cells were delivered with 2000 kDa FITC-dextran (0.3 mg/mL) using a 9 μm gap device with 14 ridges.

3.3   Summary of Cell VECT Mechanism

Overall, the process of cell VECT can be summarized beginning with cell volume loss during rapid compression, followed by cell uptake of surrounding volume and target molecules during recovery, and repetition of compressions for maximum intracellular delivery of target molecules.

3.3.1   Cell Volume Loss During Rapid Compression

The rapid compressions that cells experience in the cell VECT microfluidic device are vital for intracellular delivery. As cells flow rapidly down the microchannel, they encounter several ridges with a rectangular profile. In order to pass through the ridge, the cell must undergo rapid compression. A sufficiently rapid compression will cause the cell to lose some of its intracellular volume. Faster compressions have been shown to increase volume loss until a maximum is reached for a cell type with a particular gap size. Smaller compression gaps impose greater strain on the cells, which also results in greater volume loss. We found that the cell behaves as a viscoelastic material, with increasingly viscous behavior as the cell undergoes faster compressions. This viscoelastic behavior allows the cell to deform at a certain range of time scales while conserving volume. If the cell undergoes a compression that exceeds this range of time scales, the cell loses volume. It has been found that increased volume loss facilitates increased intracellular delivery of target molecules suspended with the cells.

52

3.3.2   Uptake of Surrounding Volume During Recovery

The loss of cell volume during compression does not cause intracellular molecule delivery in and of itself. Instead, cell volume loss creates the potential for intracellular delivery to occur because the elastic nature of the cell causes the cell to recover to its normal shape and volume after a deformation. Therefore, convective intracellular molecule delivery requires cell volume recovery. A cell that loses more volume must also recover more volume, and therefore it will uptake more surrounding molecules. Cells that are allowed sufficient time to recover volume between compressions were shown to uptake more target molecules than cells that had less time to recover. Overall, cell volume loss and recovery are both necessary components of intracellular delivery by cell volume exchange.

3.3.3   Repeat Compressions for Maximum Delivery

The repetition of these compressions causes multiple cell volume exchange events. Each volume exchange event raises the intracellular target molecule concentration to be closer to the extracellular concentration. Therefore, the use of multiple ridges in the microfluidic devices results in increased intracellular delivery of target molecules. This trend continues to a plateau, where increasing the number of ridges no longer significantly improves delivery. We determined that molecule delivery occurs at a rapid time scale during cell compression inside the device, rather than at longer time scales as the cell recovers after passing through the device. This finding is consistent with a rapid, convective mechanism of intracellular delivery, rather than a slower, diffusive mechanism.

3.4 Methods

3.4.1 Fabrication of Microfluidic Channels

The microfluidic features of this device were molded onto polydimethylsiloxane (PDMS) and plasma bonded to a glass slide. A reusable SU-8 mold was made using standard two-step photolithography on a silicon wafer. To fabricate the devices, a 10:1 ratio of PDMS and crosslinking agent was mixed and poured onto the SU-8 mold to form the microfluidic channel features by replica molding. The PDMS was then degassed in a vacuum chamber and cured for 1 hr at 80°C. The cooled PDMS was then removed from the molds and outlets and inlets were punched using biopsy punches. The PDMS was then bonded to clean glass slides using a plasma bonder (PDC-32G Harrick) followed by 1 hr in a 80°C oven. After cooling, the channels were passivated using 1% bovine serum albumin (BSA) for an overnight incubation at 4°C. For more detailed protocols, please see Appendix A.1.

3.4.2 Microfluidic Experimental Setup

Cells were resuspended in a cell flow buffer consisting of DPBS (-/-) with 0.1% BSA, 0.04% EDTA. Experiments in which video was taken used cell flow buffer with the addition of 25% Percoll to maintain cell suspension in buffer without settling. The cells were isolated from culture media and resuspended in buffer at ~1-5x10^6 cells/mL with the desired concentration of target molecules. The cell-buffer suspension was infused into the microfluidic device at a controlled rate using syringe pumps (PHD 2000, Harvard Apparatus). A cell flow rate of ~100 mm/s through the channel was used unless the flow rate was the independent variable. For delivery experiments, following collection from the

outlets, the cells were washed 2X with 10-fold volume DPBS (-/-) to remove residual molecules external to the cells

3.4.3   Cell Culture

K562 cells from ATCC were cultured in RPMI-1640 supplemented with 10% fetal bovine serum (FBS) and 1% penicillin-streptomycin. HL-60 cells from ATCC were cultured in IMDM with 20% FBS and 1% penicillin-streptomycin. HEY cells from MD Anderson Cancer Center in Houston, TX were cultured in RPMI-1640 with 10% FBS and 1% penicillin-streptomycin. OVCAR-3 cells from the National Cancer Institute (NCI) in Bethesda, MD were cultured in RPMI-1640 with 20% FBS and 1% penicillin-streptomycin. Adherent cells were passaged using 0.25% Trypsin-EDTA. The cells were incubated at 37°C with 5% CO_2.

3.4.4   High Speed Video Microscopy

The experiments were carried out on the stage of an inverted bright-field microscope (Eclipse Ti, Nikon), with a high-speed camera attachment (Phantom v7.3, Vision Research). PDMS microchannel deformation was analyzed using extra-fine objective focusing on the beginning of the ridge field, where deformation would be highest. Our studies were conducted at flow rates in which deformation of the microchannel and ridges was not detectable (<1 μm). The minimum flow rate of 3 μL/min was the slowest flow rate at which cells would pass under the ridges. High speed (>1,000 fps) videos were taken of cells during processing at various segments of the device.

3.4.5   *Video Analysis for Cell Volume Change*

To measure the cell volume inside the device, we took measurements of the cell area from video data and applied volume assumptions based on a cell deformation model. For automated measurements, a custom cell tracking algorithm was used to automatically track the trajectory and area of cells in the video, with manual measurements used to verify. For each tracked cell, the algorithm identified all video frames where the cell was visible, and extracted the position and number of pixels it occupied (area). For each manual measurement, we took the ellipse that fit to the pixels of the sharpest gray scale intensity gradient to represent the maximum projected cell boundary. We calibrated the length scales of each image based on known ridge dimensions, which enabled us to translate the number of pixels into an area measurement. For each cell, we measured the area before it entered the ridge region of the device to determine its uncompressed volume and the area when completely under each ridge to determine the compressed volumes. The volume of the unperturbed suspension cell was taken as an ellipsoid where radius was extracted from cell area measurement and used to calculate volume. The process of calculating a volume measurement from a 2-dimensional image of a compressed cell has potential sources of error due to the uncertainty of the 3-dimensional shape of the cell under the ridge. To address this uncertainty, we considered two cases for cell shape that represent the upper and lower limits of possible cell volume. The smallest possible cell volume corresponds to the unperturbed ellipsoid case, where the cell maintains an ellipsoid shape with a diameter in the Z-plane (into the image plane) equal to the known ridge compression gap as measured by profilometry. The largest possible cell volume corresponds to the cylindrical case, where the Z-plane height of the cylindrical cell is equal to the known ridge

compression gap. To reconcile these two cell shape cases, we modeled the compressed cell as a truncated ellipsoid. To calculate the volume of a truncated ellipsoid cell, we applied the ellipsoid procedure to the compressed cell area and cut away equal caps that represent the volume of the ellipsoid that intersected with the known constraints of the ridge and channel bottom. This was considered the maximum reasonable volume for the compressed cell as it approached the cylindrical case for larger cells and collapsed back to the unperturbed ellipsoid case for smaller cells.

3.4.6 Statistical Analysis

GraphPad Prism and Microsoft Excel were used to perform statistical analysis (ANOVA and t-test) and generate plots. The curve for Er vs volume change was obtained in Prism by transforming the Er values for all four cell types to log, then performing a nonlinear regression to a sigmoidal function as a physiologically relevant model of cell volume change behavior during the volume change transition phase of Er values and at the maximum and minimum Er values.

3.4.7 Flow Cytometry

The BD Accuri C6 Flow Cytometer was used to characterize cell uptake of fluorescent target molecules. Samples processed with FITC-dextran were excited with a 488 nm wavelength laser and emission was detected with a 533/30 filter. Fluorescence intensity was normalized with respect to the highest intensity group. A threshold fluorescence intensity set to include the brightest 10% of the No device control was used to gate for positive delivery, unless otherwise stated.

3.4.8   Atomic Force Microscopy

To characterize the mechanical properties of the ovarian cancer cell lines, we used force spectroscopy to obtain force-indentation curves with an MFP-3D atomic force microscope (Asylum Research) with an integrated optical microscope (Nikon) on a vibration isolation table. Cells were grown on glass FluoroDishes (World Precision Instruments). For better global stiffness measurements of the cell, 5.46 μm spherical polystyrene particles were attached to tipless silica nitride cantilevers (Bruker Probes) using a two-part epoxy and dried for >24 hours. The AFM was calibrated by taking a single force curve on a clean FluoroDish. The Sader calibration method was used to obtain cantilever spring constants (k is approximately 10-25 pN/nm) based on the thermal vibration of the cantilever. Cells were indented at 2 μm/s until a force trigger of 10 nN was reached. The z position of the cantilever was held in place for 5 seconds, dwelling towards the surface, allowing for viscous relaxation of the cell before the cantilever was retracted. See Figure ## for schematic of AFM setup, force curve acquisition, and fit. We used custom R code to fit the dwell region of the force curve to an exponential decay function to extract the viscous rate constant. To extract the cell Young's modulus, we used custom R code relying on the Hertzian contact model.

3.5 References

[1]   Deng, Y. X. *et al.* Inertial Microfluidic Cell Stretcher (iMCS): Fully Automated, High-Throughput, and Near Real-Time Cell Mechanotyping. *Small.* **13**, doi:UNSP 170070510.1002/smll.201700705 (2017).

[2]   Evans, E. A. Structural model for passive granulocyte behaviour based on mechanical deformation and recovery after deformation tests. *Kroc Found. Ser.* **16**, 53-71 (1984).

[3]   Gabriele, S., Benoliel, A.-M., Bongrand, P. & Théodoly, O. Microfluidic Investigation Reveals Distinct Roles for Actin Cytoskeleton and Myosin II Activity in Capillary Leukocyte Trafficking. *Biophys. J.* **96**, 4308-4318, doi:http://dx.doi.org/10.1016/j.bpj.2009.02.037 (2009).

[4]   Guo, Q., Park, S. & Ma, H. Microfluidic micropipette aspiration for measuring the deformability of single cells. *Lab Chip.* **12**, 2687-2695, doi:10.1039/c2lc40205j (2012).

[5]   Lokhandwalla, M. & Sturtevant, B. Mechanical haemolysis in shock wave lithotripsy (SWL): I. Analysis of cell deformation due to SWL flow-fields. *Phys. Med. Biol.* **46**, 413-437 (2001).

[6]   Mokbel, M. *et al.* Numerical Simulation of Real-Time Deformability Cytometry To Extract Cell Mechanical Properties. *ACS Biomater. Sci. Eng.*, doi:10.1021/acsbiomaterials.6b00558 (2017).

[7]   Needham, D. & Hochmuth, R. M. Rapid flow of passive neutrophils into a 4 microns pipet and measurement of cytoplasmic viscosity. *J. Biomech. Eng.* **112**, 269-276 (1990).

[8]   Tran-Son-Tay, R., Needham, D., Yeung, A. & Hochmuth, R. M. Time-dependent recovery of passive neutrophils after large deformation. *Biophys. J.* **60**, 856-866, doi:10.1016/S0006-3495(91)82119-1 (1991).

[9]   Trickey, W. R., Baaijens, F. P. T., Laursen, T. A., Alexopoulos, L. G. & Guilak, F. Determination of the Poisson's ratio of the cell: recovery properties of chondrocytes after release from complete micropipette aspiration. *J. Biomech.* **39**, 78-87, doi:10.1016/j.jbiomech.2004.11.006 (2006).

[10]   Jones, W. R. *et al.* Alterations in the Young's modulus and volumetric properties of chondrocytes isolated from normal and osteoarthritic human cartilage. *J. Biomech.* **32**, 119-127, doi:Doi 10.1016/S0021-9290(98)00166-3 (1999).

[11]   Deng, Y. *et al.* Intracellular Delivery of Nanomaterials via an Inertial Microfluidic Cell Hydroporator. *Nano Lett.* **18**, 2705-2710, doi:10.1021/acs.nanolett.8b00704 (2018).

[12]   Islam, M. *et al.* Microfluidic Sorting of Cells by Viability Based on Differences in Cell Stiffness. *Sci. Rep.* **7**, 1997, doi:10.1038/s41598-017-01807-z (2017).

[13]   Kizer, M. E. *et al.* Hydroporator: a hydrodynamic cell membrane perforator for high-throughput vector-free nanomaterial intracellular delivery and DNA origami biostability evaluation. *Lab Chip.* **19**, 1747-1754, doi:10.1039/c9lc00041k (2019).

[14]   Liu, A. *et al.* Microfluidic generation of transient cell volume exchange for convectively driven intracellular delivery of large macromolecules. *Mater. Today.* **21**, 703-712, doi:10.1016/j.mattod.2018.03.002 (2018).

[15]   Liu, A. *et al.* Cell Mechanical and Physiological Behavior in the Regime of Rapid Mechanical Compressions that Lead to Cell Volume Change. *Small.* e1903857, doi:10.1002/smll.201903857 (2019).

[16]   Wang, G. *et al.* Microfluidic cellular enrichment and separation through differences in viscoelastic deformation. *Lab Chip.* **15**, 532-540, doi:10.1039/c4lc01150c (2015).

[17]   Wang, G. *et al.* Stiffness dependent separation of cells in a microfluidic device. *PLoS One.* **8**, e75901, doi:10.1371/journal.pone.0075901 (2013).

[18]   Wang, G., Turbyfield, C., Crawford, K., Alexeev, A. & Sulchek, T. Cellular enrichment through microfluidic fractionation based on cell biomechanical properties. *Microfluid. Nanofluid.* **19**, 987-993, doi:10.1007/s10404-015-1608-y (2015).

[19]   Sharei, A. *et al.* Plasma membrane recovery kinetics of a microfluidic intracellular delivery platform. *Integr. Biol.* **6**, 470-475, doi:10.1039/c3ib40215k (2014).

[20]   Hallow, D. M. *et al.* Shear-induced intracellular loading of cells with molecules by controlled microfluidics. *Biotechnol. Bioeng.* **99**, 846-854, doi:10.1002/bit.21651 (2008).

[21]   Hwang, Y., Gouget, C. L. & Barakat, A. I. Mechanisms of cytoskeleton-mediated mechanical signal transmission in cells. *Commun. Integr. Biol.* **5**, 538-542, doi:10.4161/cib.21633 (2012).

[22]   Martens, J. C. & Radmacher, M. Softening of the actin cytoskeleton by inhibition of myosin II. *Pflugers Arch.* **456**, 95-100, doi:10.1007/s00424-007-0419-8 (2008).

[23]   Varkuti, B. H. *et al.* A highly soluble, non-phototoxic, non-fluorescent blebbistatin derivative. *Sci Rep.* **6**, 26141, doi:10.1038/srep26141 (2016).

[24]   Thoumine, O. & Ott, A. Time scale dependent viscoelastic and contractile regimes in fibroblasts probed by microplate manipulation. *J. Cell Sci.* **110 (Pt 17)**, 2109-2116 (1997).

[25]   Li, Q. S., Lee, G. Y. H., Ong, C. N. & Lim, C. T. AFM indentation study of breast cancer cells. *Biochem. Biophys. Res. Commun.* **374**, 609-613, doi:10.1016/j.bbrc.2008.07.078 (2008).

[26]   Nawaz, S. *et al.* Cell Visco-Elasticity Measured with AFM and Optical Trapping at Sub-Micrometer Deformations. *PLoS One.* **7**, doi:ARTN e4529710.1371/journal.pone.0045297 (2012).

[27]   Raj, A., Dixit, M., Doble, M. & Sen, A. K. A combined experimental and theoretical approach towards mechanophenotyping of biological cells using a constricted microchannel. *Lab Chip.* **17**, 3704-3716, doi:10.1039/c7lc00599g (2017).

[28]   Leong, F. Y., Li, Q. S., Lim, C. T. & Chiam, K. H. Modeling cell entry into a micro-channel. *Biomech. Model. Mechanobiol.* **10**, 755-766, doi:10.1007/s10237-010-0271-1 (2011).

[29]   Yeung, A. & Evans, E. Cortical shell-liquid core model for passive flow of liquid-like spherical cells into micropipets. *Biophys. J.* **56**, 139-149, doi:10.1016/S0006-3495(89)82659-1 (1989).

[30]   Deng, L. *et al.* Fast and slow dynamics of the cytoskeleton. *Nat. Mater.* **5**, 636-640, doi:10.1038/nmat1685 (2006).

[31]   Gardel, M. L. *et al.* Scaling of F-actin network rheology to probe single filament elasticity and dynamics. *Phys. Rev. Lett.* **93**, 188102, doi:10.1103/PhysRevLett.93.188102 (2004).

[32]   Stamenovic, D. Cell mechanics: two regimes, maybe three? *Nat. Mater.* **5**, 597-598, doi:10.1038/nmat1700 (2006).

[33]   Bursac, P. *et al.* Cytoskeletal remodelling and slow dynamics in the living cell. *Nat. Mater.* **4**, 557-561, doi:10.1038/nmat1404 (2005).

[34]   Fabry, B. *et al.* Scaling the microrheology of living cells. *Phys. Rev. Lett.* **87**, 148102, doi:10.1103/PhysRevLett.87.148102 (2001).

[35]   Lenormand, G. & Fredberg, J. J. Deformability, dynamics, and remodeling of cytoskeleton of the adherent living cell. *Biorheology.* **43**, 1-30 (2006).

[36]   Calderer, C. & Liu, C. Liquid Crystal Flow: Dynamic and Static Configurations. *SIAM J. Appl. Math.* **60**, 1925-1949 (2000).

[37]   Klein, D. H., Leal, L. G., Garcia-Cervera, C. J. & Ceniceros, H. D. Ericksen number and Deborah number cascade predictions of a model for liquid crystalline polymers for simple shear flow. *Phys. Fluids.* **19**, doi:Artn 02310110.1063/1.2424499 (2007).

[38]   Vincent, J. *Structural Biomaterials*. 3rd edn, (Princeton University Press, 2012).

[39]   Cacopardo, L., Guazzelli, N., Nossa, R., Mattei, G. & Ahluwalia, A. Engineering hydrogel viscoelasticity. *J. Mech. Behav. Biomed. Mater.* **89**, 162-167, doi:10.1016/j.jmbbm.2018.09.031 (2019).

[40]   Roylance, D. *Engineering Viscoelasticity*. (Massachusetts Institute of Technology Press, 2001).

[41]   Sharei, A. *et al.* A vector-free microfluidic platform for intracellular delivery. *Proc. Natl. Acad. Sci. U. S. A.* **110**, 2082-2087, doi:10.1073/pnas.1218705110 (2013).

[42]   Sharei, A. *et al.* Cell squeezing as a robust, microfluidic intracellular delivery platform. *J. Visualized Exp.*, e50980, doi:10.3791/50980 (2013).

CHAPTER 4.   DELIVERY CAPABILITIES AND CELL PHYSIOLOGICAL EFFECTS

4.1   Introduction

Studies of microscale cell deformations observed by high speed video microscopy have elucidated a new cell behavior in which sufficiently rapid mechanical compression of cells can lead to transient cell volume loss and then recovery. Our work has discovered that the resulting volume exchange between the cell interior and the surrounding fluid can be utilized for efficient, convective delivery of large macromolecules (2000 kDa) to the cell interior. However, many fundamental questions remain about this cell behavior, including the intracellular macromolecule delivery capabilities the physiological effects experienced by the cell. In this section we study the relation between intracellular delivery and molecule size, the intracellular molecule concentration achieved, and the localization of delivery. We also analyze nuclear envelope integrity and intracellular protein loss after the volume exchange process. These results define a highly controlled cell volume exchange mechanism for intracellular delivery of large macromolecules that maintains cell viability and function for invaluable downstream research and clinical applications.

Efficient intracellular delivery of target macromolecules remains a major obstacle in cell engineering and other biomedical applications. The ability of cells to rapidly exchange fluid with their surroundings in response to ultrafast mechanical compressions opens a potent new way to deliver large extracellular molecules and particles into cells. We utilized this method of cell volume exchange for convective transfer (VECT) to

intracellularly deliver molecules and particles suspended in extracellular fluid. The ability to efficiently deliver large molecules contrasts with currently described delivery methods that rely on diffusion for transmembrane transfer of molecules, which is inefficient for large macromolecules [1-7]. Thus, this new phenomenon of cell volume exchange under ultrafast mechanical deformation potentially enables a multitude of highly valuable cell engineering processes.

Studies have shown that compression-mediated cell volume change increases with higher cell strain and faster strain rate [8-11]. In this chapter, we aim to characterize the delivery capabilities of cell VECT with regard to molecule size and intracellular localization of the payload. Furthermore, studying the effects of cell volume loss on cell physiology will inform the use of this method in research and clinical intracellular delivery applications. While cells that undergo volume change were shown to maintain viability, other factors of interest such as nuclear envelope integrity and intracellular protein loss have not yet been characterized. This aim seeks to characterize the intracellular molecule delivery capabilities and the resultant physiological effects on the cell.

The cell volume exchange phenomenon is implemented in a microfluidic system that uses ridges to briefly impose compressions (Figure 4.1A, B). Cells suspended in buffer and flowed through the device rapidly pass through a microchannel in which they undergo sudden deformations under the ridges (Figure 4.1C), resulting in an abrupt change in shape. This compression is designed to have a rapid onset (on the order of 10-100 μs) and brief duration (~1 ms as determined by high-speed video microscopy), resulting in a cell behavior regime of fast cell volume loss and recovery [9,11,12]. The volume loss and recovery can cause cells to uptake surrounding molecules suspended therein (Figure 4.1D),

a phenomenon called cell volume exchange for convective transfer (cell VECT). This cell behavior has been used to deliver macromolecules to the interior of various human cell types using convection, which is not restrained by molecule size for the range tested (4-2000 kDa) [9,11].
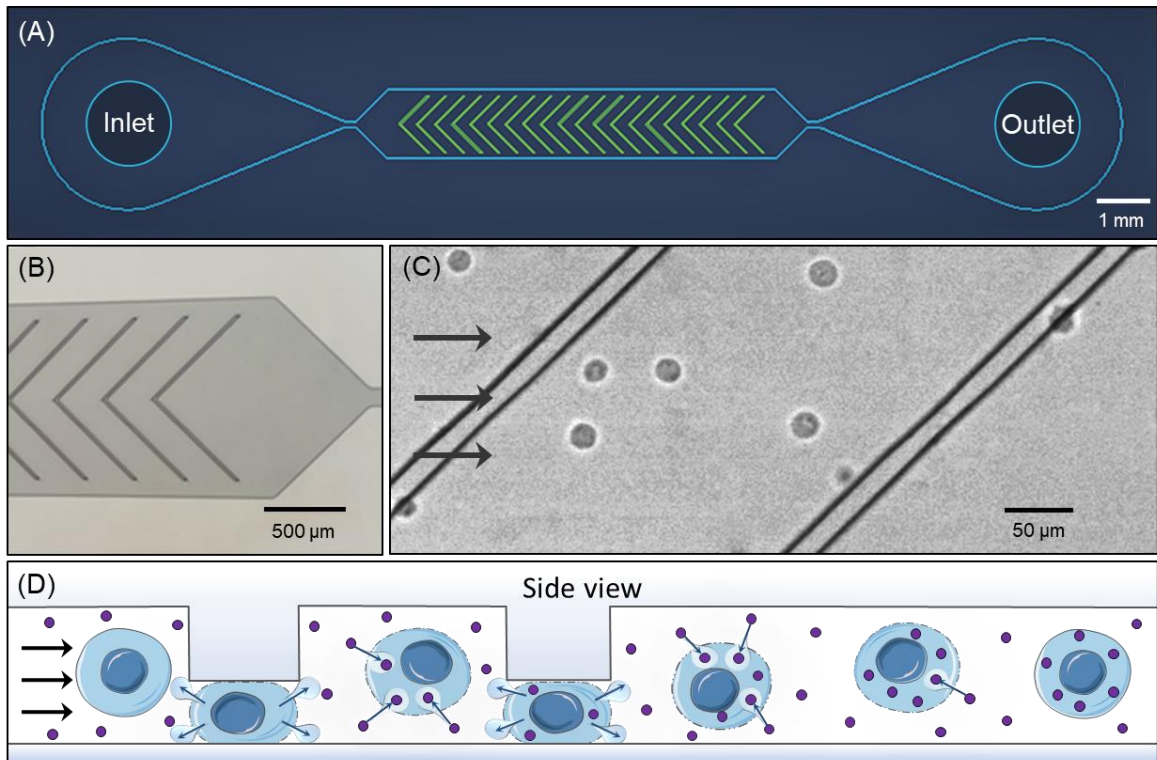
Figure 4.1: Microfluidic ridge-based cell compressions cause volume exchange. (A) Schematic of device layout. See Appendix A.2 for device design details. (B) Optical micrograph of microchannel with chevron ridge geometry. (C) Still-frame image from video of K562 cells flowing through the microchannel and ridges under light microscopy. (D) Schematic of cell permeabilization and volume loss, subsequent recovery, and repeated volume exchange with compressions.

4.2   Characterizing Intracellular Delivery Capabilities

4.2.1   Convective Delivery Dependence on Molecule Size

We aimed to characterize the convective nature of intracellular delivery using cell VECT by testing the impact of molecule size on delivery. Since diffusion rate is inversely proportional to molecule size, diffusive delivery typically shows lower efficiency for larger macromolecules [2-7]. In contrast, cell VECT demonstrated intracellular delivery with high efficiency (~90% of cells uptake molecules) regardless of molecule size for the range tested (Figure 4.2A). This study used an equal buffer concentration (mass per volume) of molecules ranging from 4 kDa, roughly the molecular weight (MW) of a small molecule drug, to 2000 kDa, which is roughly the MW of a 3200 bp plasmid. This size-independent delivery supported our hypothesis that molecule uptake was achieved predominantly by advection, which is the directional transport of extracellular molecules into the cell due to bulk fluid flow during cell volume recovery [13,14], rather than molecular diffusion through membrane pores. We also demonstrated delivery of FluoSphere 100 nm diameter fluorescent polystyrene beads (ThermoFisher) to K562 cells as a demonstration of this method's ability to deliver extremely large particles (Figure 4.2B).
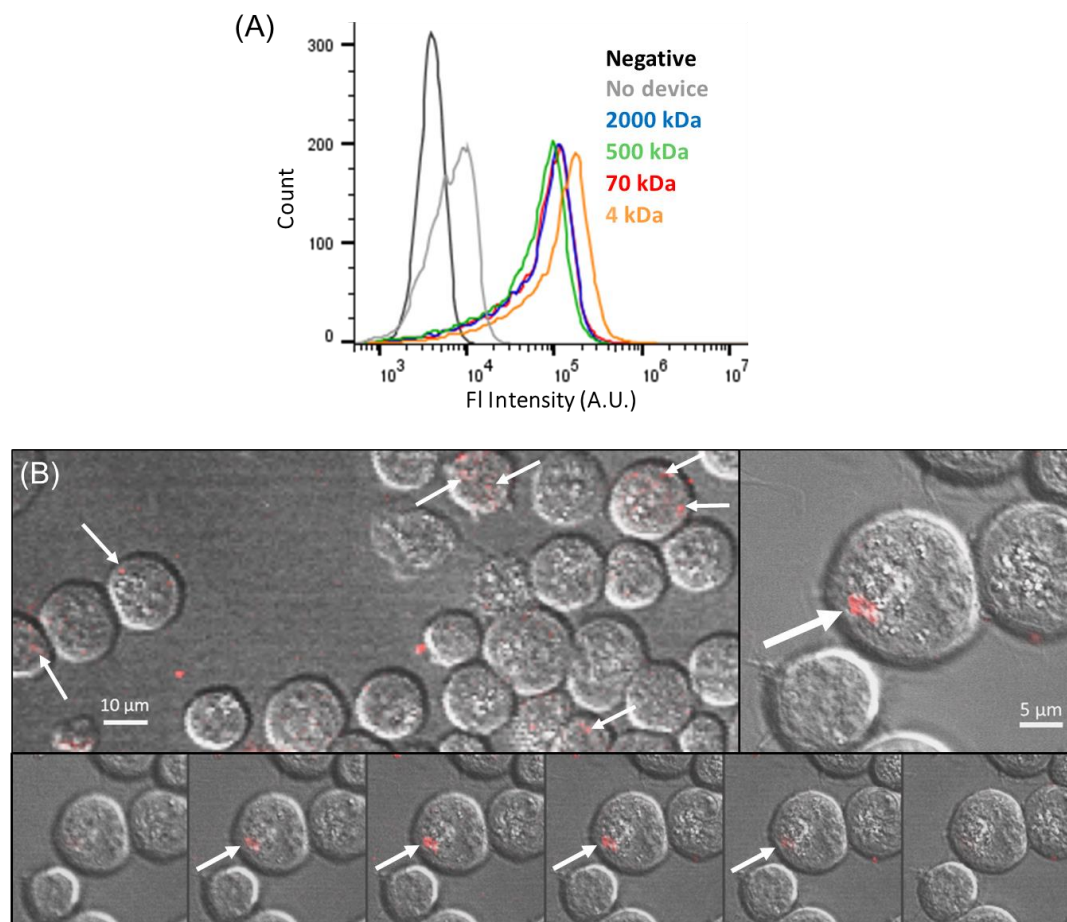
Figure 4.2: Molecule size capability of intracellular delivery. (A) Delivery was independent of molecule size for the range tested (4-2000 kDa FITC-dextran, 0.3 mg/mL). No device control with 2000 kDa FITC-dextran. K562 cells with 10.2 μm gap device. (B) Delivery of 100 nm fluorescent particles to K562 cells with 7 μm gap device. Confocal microscopy shows fluorescent particles (red) delivered to the cell interior after microfluidic device processing. Confocal microscopy Z-stacks of the same cell (bottom row) show that fluorescent particles are in the cell interior.

4.2.2   *Delivery Saturation and Removal*

We tested the dependence of intracellular delivery on extracellular concentration of the target molecule. The intracellular molecular delivery was also found to increase with higher extracellular concentration of the target molecule (Figure 4.3A) when qualitatively analyzed by flow cytometry of a delivered fluorescent tracer molecule, 2000 kDa FITC-

dextran. To more precisely quantify intracellular delivery, we delivered ferumoxytol iron nanoparticles to adipose-derived stem cells (ADSCs). Inductively coupled plasma (ICP) mass spectrometry was used to quantify the iron content per cell. Approximating the volume of an ADSC to be on the order of 1 pL, we find that the intracellular concentration of target molecule reaches ~10-20% of the extracellular concentration (Figure 4.3B,C) [15]. This intracellular concentration is reasonable considering that cells, for the most part, consist of large internal structures such as the nucleus, membrane bound organelles, and the cytoskeleton, and therefore a significant portion of the intracellular volume is inaccessible to foreign molecules.
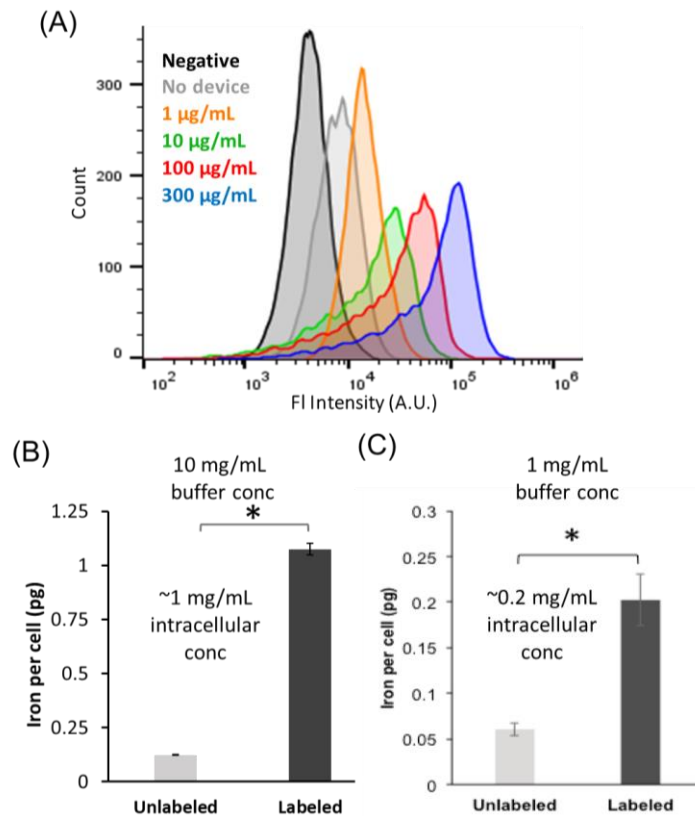
Figure 4.3: Characterizing intracellular concentration of delivered molecules. (A) K562 cells processed with 1-300 μg/mL of 2000 kDa FITC-dextran qualitatively increased in intracellular delivery when characterized by cell fluorescence intensity. No device control with 1 μg/mL. 10.2 μm gap devices used. (B) Iron nanoparticles delivered to

ADSCs were quantified with ICP mass spectrometry to reach intracellular concentration ~10-20% of the extracellular concentration. ADSCs were processed in a 9.6 μm gap device. ICP mass spectrometry done by Daldrup-Link Lab, Stanford.

To further explore the hypothesis that cell VECT causes the target molecule concentration in the cytosol to reach equilibrium due to repeated compressions, we processed previously dextran-positive cells through the device with dextran-free buffer to remove the dextran from within the cells. We first delivered 2000 kDa FITC-dextran to K562 cells using VECT, then resuspended these delivered cells in FITC-free buffer and processed them in the device again for the Removal group. We found that the Removal group has a mean fluorescence intensity that matches the No Device group, indicating that this method is highly effective in removing previously delivered molecules (Figure 4.4A). These results support our assertion that cell VECT achieved molecule concentration equilibrium and can remove unbound molecules from the cell interior, a capability not demonstrated with diffusive delivery [16]. Similarly, we also delivered a fluorescently labeled nonbinding isotype control antibody to human embryonic kidney (HEK) cells and then removed the delivered antibodies by processing the cells again using cell VECT in an antibody-free buffer (Figure 4.4B). These data suggest that multiple compartments exist within the cell, some of which undergo rapid exchange by cell VECT to reach a saturation point of exchange with the extracellular molecule concentration.
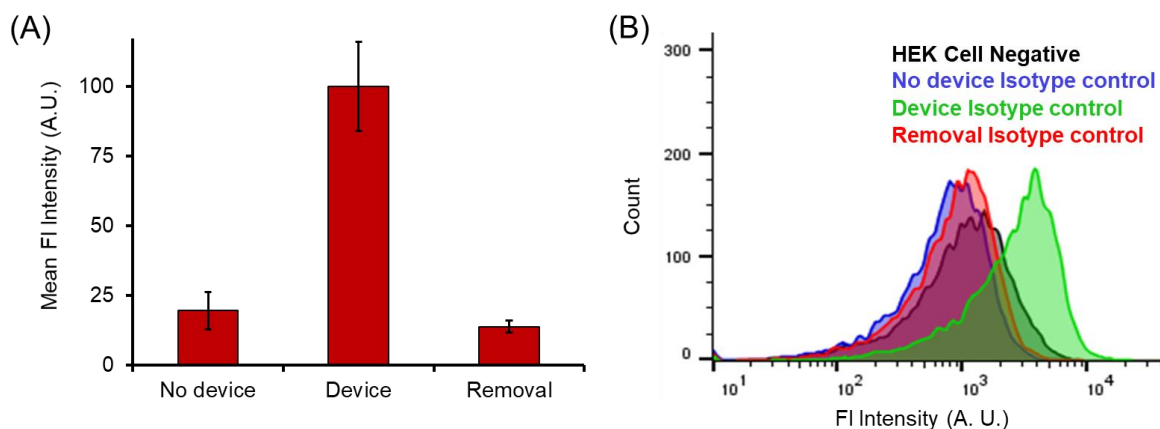
Figure 4.4: Characterizing equilibration with extracellular concentration by removal of delivered molecules. (A) 2000 kDa FITC-dextran (0.3 mg/mL) delivered to K562 cells was removed by processing the cells in the device with a FITC-free buffer, N=2. 7 μm gap device with 22 ridges used. Fluorescence intensity was normalized to the highest group. (B) A non-binding APC IgG1 isotype control antibody (50 μg/mL) was delivered to HEK cells using a 7 μm gap device, and then removed by processing the cells through the device again in antibody-free buffer.

4.2.3   Intracellular Localization of Delivered Molecules

The application of cell VECT can address important limitations of intracellular delivery platforms. Endocytic intracellular delivery is often confined to endosomes, which detain and eventually degrade the delivered reagent in lysosomes. Therefore, the majority of target molecules delivered using endocytic mechanisms are unable reach their desired intracellular interaction sites due to an inability to escape the endosome [17-20]. Confocal imaging of live cells less than an hour after processing with cell VECT shows that the fluorescently labeled delivered molecules have a diffuse localization profile throughout the cell interior, rather than a punctate profile that is characteristic of endocytosis (Figure 4.5A) [21]. These findings suggest that cell VECT delivery does not rely on endocytosis, and instead delivers target molecules unencapsulated, directly to the cytosol. Direct cytosolic

delivery is more advantageous for a majority of applications since it allows more direct access to various intracellular interaction sites of interest, such as the nucleus, ribosomes, cytoskeleton, and organelles.
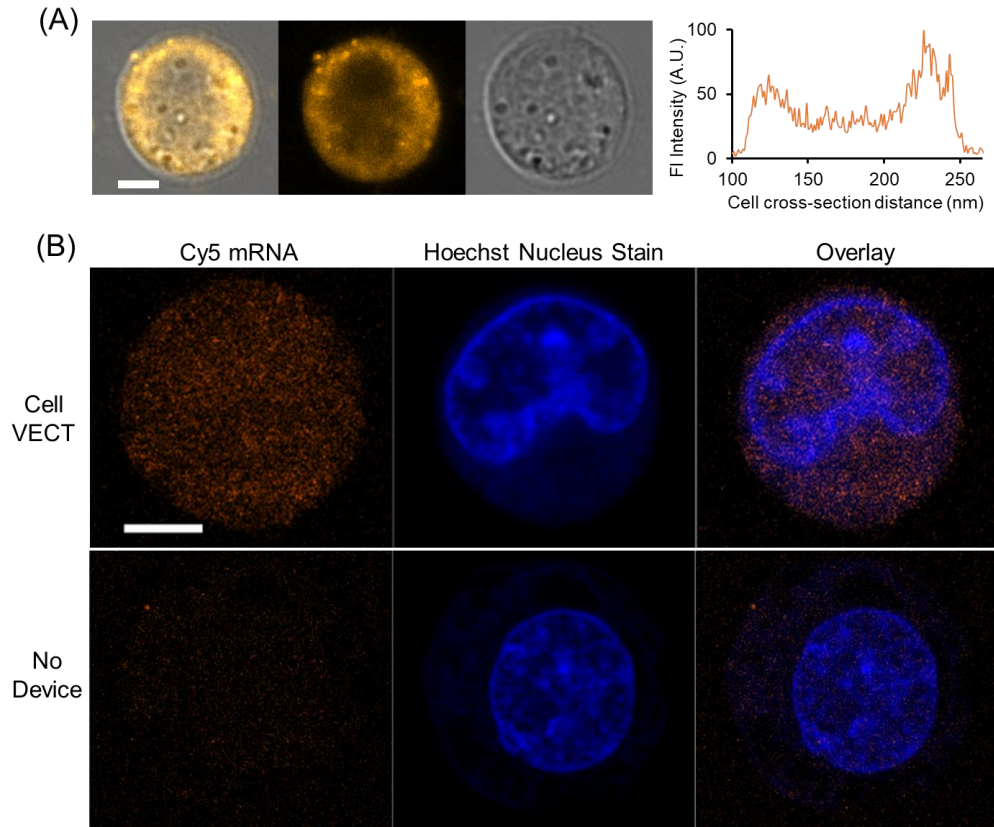
Figure 4.5: Imaging intracellular localization of delivered molecules. (A) Confocal microscopy images of a live K562 cell delivered with 2000 kDa TRITC-dextran (0.5 mg/mL) with diffuse fluorescence profile throughout the cell interior. 10.2 μm gap device used. Scale bar 5 μm. (B) Confocal microscopy showed diffuse delivery of Cy5-labeled mRNA throughout the interior of a fixed K562 cell with nucleus staining. 7 μm gap device used. No Device control showed no such delivery. Scale bar 5 μm, n = 2.

To demonstrate the capabilities of the use of VECT as a highly efficient delivery platform for transfection agents, we successfully delivered Cy5-mRNA (TriLink) into K562 cells. The cells were stained with Hoechst nucleus stain to visualize the intracellular

localization of the Cy5-mRNA (Figure 4.5B). Using confocal microscopy on live cells less than an hour after microfluidics, the mRNA was shown to permeate the cell interior. A No Device control of K562 cells exposed to Cy5-mRNA without device processing was imaged for comparison.

To further determine the non-endocytic nature of cell VECT intracellular delivery, we stained cells with DiO membrane stain, which stains both the exterior plasma membrane and intracellular membranes. Cells were also stained with Hoechst nucleus stain and then live cells were imaged using confocal microscopy less than an hour after microfluidic processing. The intracellular localization of a delivered fluorescently labeled noncoding plasmid did not overlap with the localization of fluorescently dyed intracellular membranes (Figure 4.6).
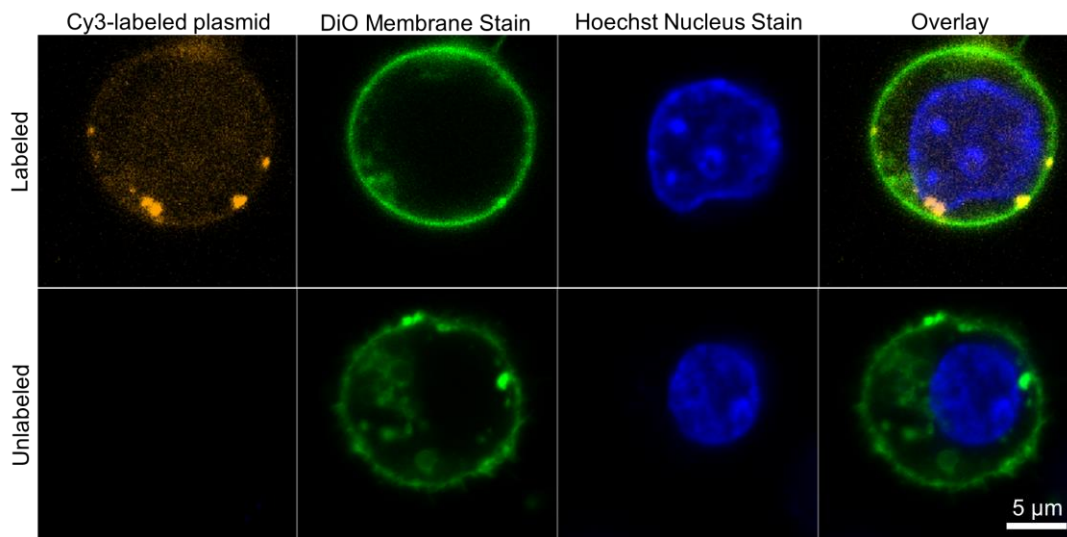
Figure 4.6: Imaging nonendocytic intracellular delivery. K562 cells with nucleus and membrane staining were delivered with Cy3-labeled non-coding plasmid using a 9 μm gap microfluidic device. Cells were stained with DiO membrane stain, which stains both the exterior plasma membrane and intracellular membranes. Cy3-plasmid can be observed inside the cytoplasm of live cells outside of the areas occupied by stained intracellular

membranes. The imaging suggests that a relatively small volume immediately beneath the cell membrane undergoes increased exchange with cell VECT.

Following microfluidic processing, intracellularly delivered molecules will persist in the cell cytoplasm. After several hours, they will eventually be sequestered into lysosomes and metabolized by the cell. We studied the localization of iron ferumoxytol nanoparticles that were delivered to adipose tissue-derived stem cells (ADSCs). Cells were imaged ≥ 24 hrs after delivery using transmission electron microscopy (TEM). The delivered nanoparticles were observed to be stored in lysosomes, where they are slowly metabolized by the cell (Figure 4.7) [15]. This observation is consistent with published studies wherein non-endosomally delivered molecules are internally captured over the course of several hours and metabolized in lysosomes by the cell [22].
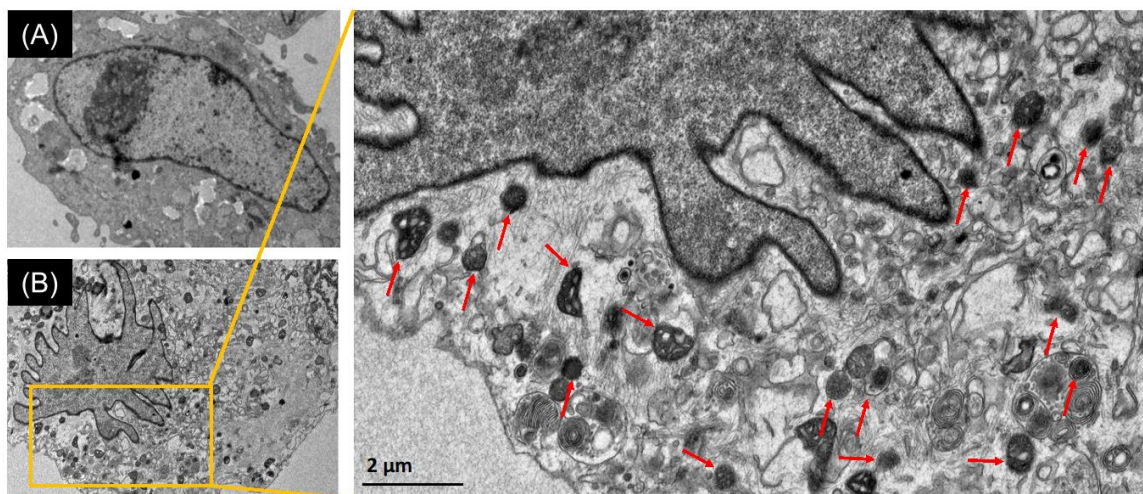
Figure 4.7: Imaging long-term intracellular localization and metabolism of delivered molecules. Adipose tissue-derived stem cells (ADSCs) were imaged with transmission electron microscopy (TEM). (A) Control ADSCs without delivery showed no nanoparticles present in the cytoplasm. (B) ADSCs delivered with iron ferumoxytol nanoparticles (10 mg/mL) show particles sequestered in lysosomes in the cytoplasm. TEM occurred ≥ 24 hrs after delivery. 9.6 μm gap device used. TEM done by Daldrup-Link Lab, Stanford.

4.3 Physiological Effects on the Cells

4.3.1 Nuclear Envelop Integrity

We next sought to understand the physiological impact of these rapid mechanical compressions on the cells. While it has been shown that the cell cytoplasm has a high capacity for deformation and recovery even at high strains, the nucleus – typically one of the largest and stiffest organelles – can limit the rate of cell deformation [23,24]. The demonstrated exchange in volume and macromolecules between the cell and its outside environment suggests that the cell membrane is compromised by fast compressions [2,9,11,25], but the integrity of the nuclear envelope has not been characterized. Nuclear envelope rupture is important to characterize because it has been associated with genome instability, aneuploidy, and DNA damage [23,26]. Severe nuclear disruption can cause material to leave the nucleus, leading to chromatin protrusions, nuclear fragmentation, and chromothripsis [26,27].

We used human embryonic kidney HEK-293 cells transduced with fluorescently labeled genes for cyclic GMP-AMP synthase (cGAS-mCherry) and nuclear localization signal (NLS-GFP) to indicate nuclear envelope rupture and loss of nuclear contents to the cytosol, respectively [23,26,28-30]. The cGAS-mCherry is a cytosolic protein that binds DNA at sites of nuclear envelop rupture. We used devices with compression gap of 7 μm and 5 μm. These gaps impose cell strains of ~0.4 and ~0.6 respectively, which is a typical range of strains used in cell VECT [9]. Electroporation was used as a positive control for nuclear envelope disruption. Nuclear envelope disruption is indicated by cGAS-mCherry accumulation in and around the nucleus at sites of rupture (Figure 4.8A). Compression of

cells using cell VECT resulted in ~10% increase in number of cells with nuclear envelope

disruption (Figure 4.8B). Varying the compression gap size between 7 µm and 5 µm did

not appear to impact percentage of nuclear rupture. Cells that were positive for nuclear

envelope rupture did not exhibit a difference in overall nucleus size (Figure 4.8C).
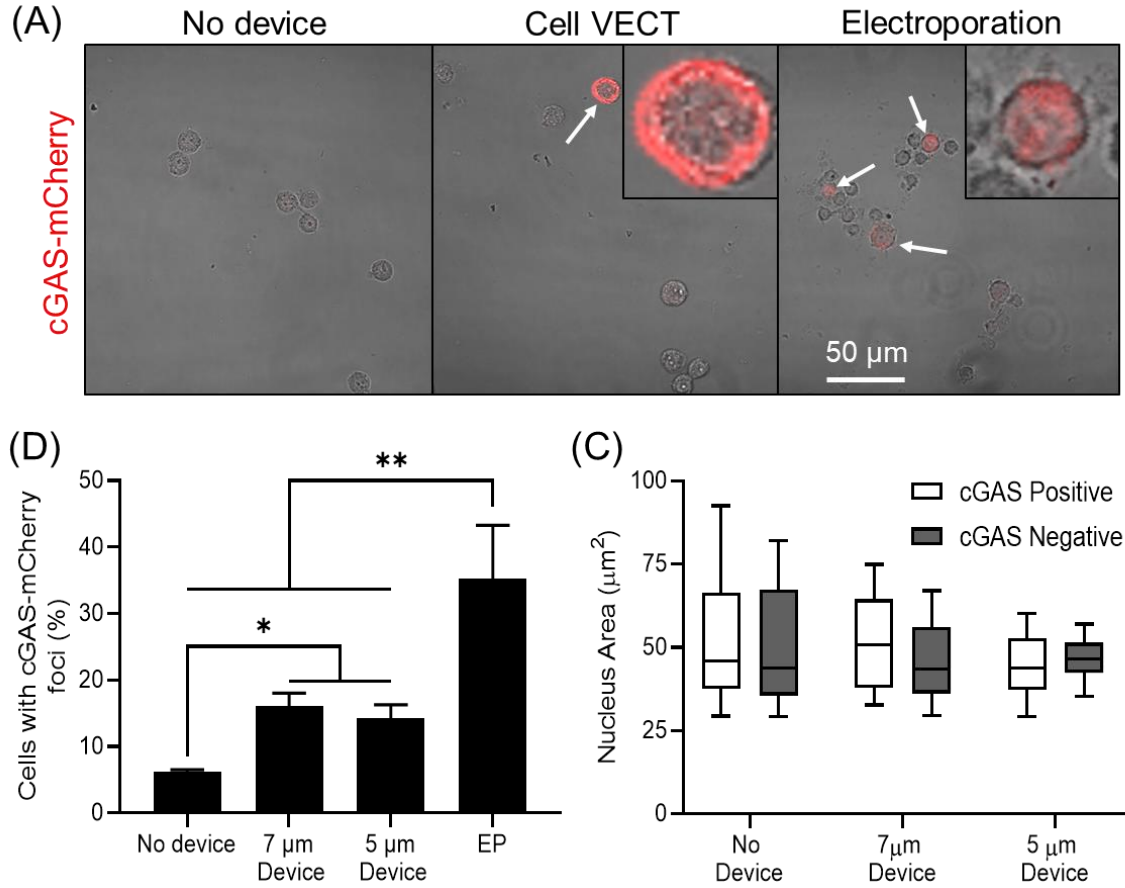
Figure 4.8: Analysis of nuclear envelop disruption in HEK cells. (A) Confocal microscopy shows cGAS-mCherry foci nuclear envelop disruption indicator (white arrows) present in a minority of 7 µm gap device-processed HEK cells and a significant portion of electroporated cells. Cells in insets are zoomed in 5X. (B) Cell VECT treated cells displayed cGAS-mCherry in ~15% of cell nuclei compared to ~6% for No Device control. Electroporation used as positive control. *P < 0.05, **P < 0.01, N = 3 (C) There is not a statistically significant correlation between nucleus size and nuclear envelope disruption.
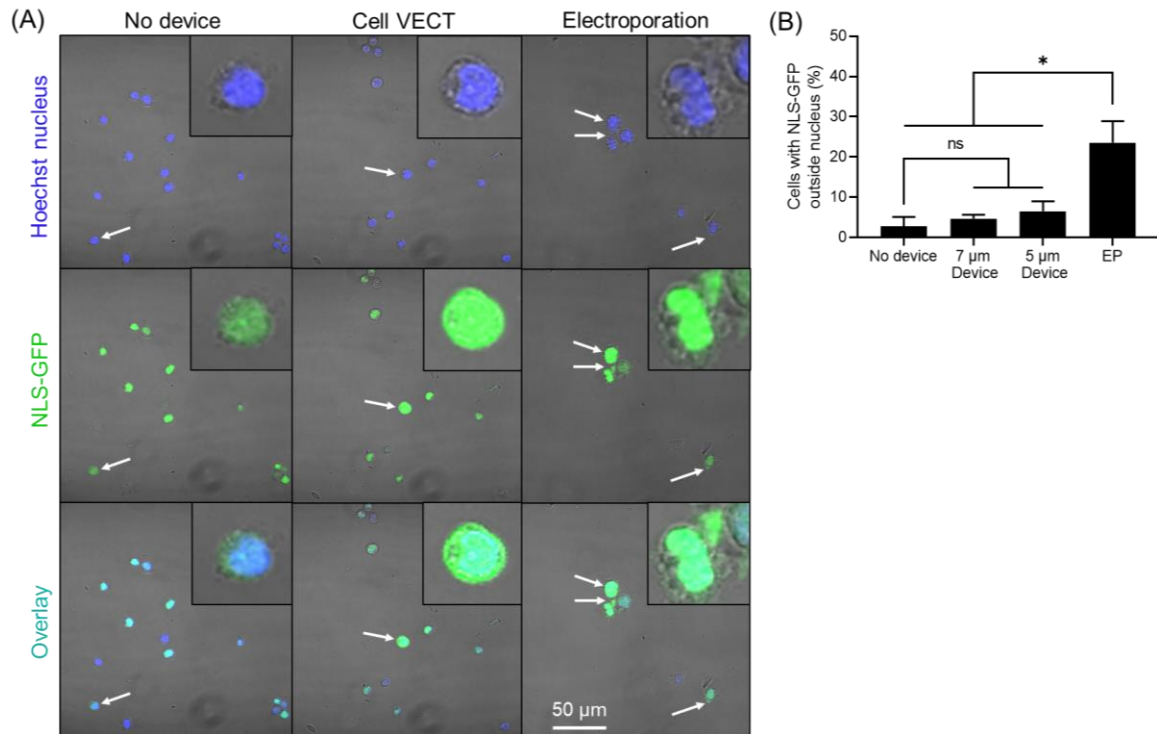
Figure 4.9: Analysis of nuclear content loss in HEK cells. (A) Confocal imaging shows colocalization of NLS-GFP to the Hoechst-stained nucleus in the majority of No device and 7 μm gap device cells, with NLS-GFP outside the nucleus in a small minority of cells (white arrows). NLS-GFP can be observed outside the nucleus in electroporated cells. Cells in insets are zoomed in 5X. (E) Compressed cells exhibit NLS-GFP outside the nucleus in <10% of cells but is not statistically significant compared to No Device control. Electroporation used as positive control. *P < 0.01, N = 3.

Nuclear content loss was determined by analyzing colocalization of NLS-GFP with a Hoechst nucleus stain (Figure 4.9A). Cells processed with cell VECT displayed a small (<5%) increase in NLS-GFP loss to the cytoplasm, but this increase was not statistically significant (Figure 4.9B). Therefore, we find that rapid, brief compressions with cell VECT causes nuclear envelope disruption in a small minority of cells. However, the disruptions do not appear to be significant enough to cause nuclear contents to leave the nuclear envelope. Therefore, it appears that the extent or duration of nuclear disruption is not

sufficient to cause loss of materials from the nucleus to the cytoplasm. Overall the findings indicate that the compression conditions typically used in cell VECT have minimal impact on nuclear integrity, which indicates a low risk of associated negative effects such as DNA damage. In contrast, electroporation substantially damages the nuclear integrity of cells, which may partially account for the low proliferative ability of electroporated cells.

4.3.2   Cell Viability and Proliferation

Understanding the physiological impact of compression-based cell volume loss not only confers a deeper understanding of this phenomenon, but also informs its use in research and clinical settings. Studies have shown that mechanically-induced cell permeabilization may also result in cell damage, as seen in various cell and tissue injuries caused by mechanical trauma [31-36]. This permeabilization can have lasting physiological effects, particularly in nerve cells [33,36]. However, numerous human cell types, including epithelial cells, chondrocytes, and leukocytes, have demonstrated the ability to recover from mechanical compression without significant impact on viability and function [2,8-12,37].

While cell volume was observed to decrease by up to 30% during compressions, cells were quickly restored to their initial size with little impact on cell integrity, viability, and related gene expression. After microfluidic processing, cell culture and expansion were successfully conducted with no change in cell growth rate. Analysis of still images of >800 cells immediately after microfluidic processing shows <3% change in mean cell size compared to cells without microfluidic processing (Figure 4.10A). Similarly, ethidium

homodimer-1 (EthD-1) staining of processed cells showed <3% cell death compared to the No Device group (Figure 4.10A). We used RT PCR immediately after microfluidics to further quantify that the compressions in the microchannel did not impact the expression of apoptotic, cytoskeletal, and other signaling genes (Figure 4.10B). A separate, detailed study on cell viability after rapid compressions, including expression of apoptotic genes, was consistent with this observation [38]. These results suggested that cells recovered normal volume and function after the brief volume loss.

Characterization of long-term viability in K562 cells up to 5 days after microfluidics indicated <5% viability loss compared to No Device and Negative controls (Figure 4.10C). Negative controls were maintained in culture, while No Device controls were exposed to the same buffer and out-of-culture conditions as Device groups. Note that all cell groups, including Negative and No Device controls, showed decreased viability at days 4 and 5 of culture without passaging due to culture overgrowth. Additionally, device-treated cells demonstrated rapid proliferation over 5 days on par with that of No Device and Negative control groups, doubling roughly once per day (Figure 4.10D). These results were not significantly impacted by decreasing the cell compression gap from 9.5 μm (~0.4 strain) to 7 μm (~0.6 strain) (Figure 4.10C,D).
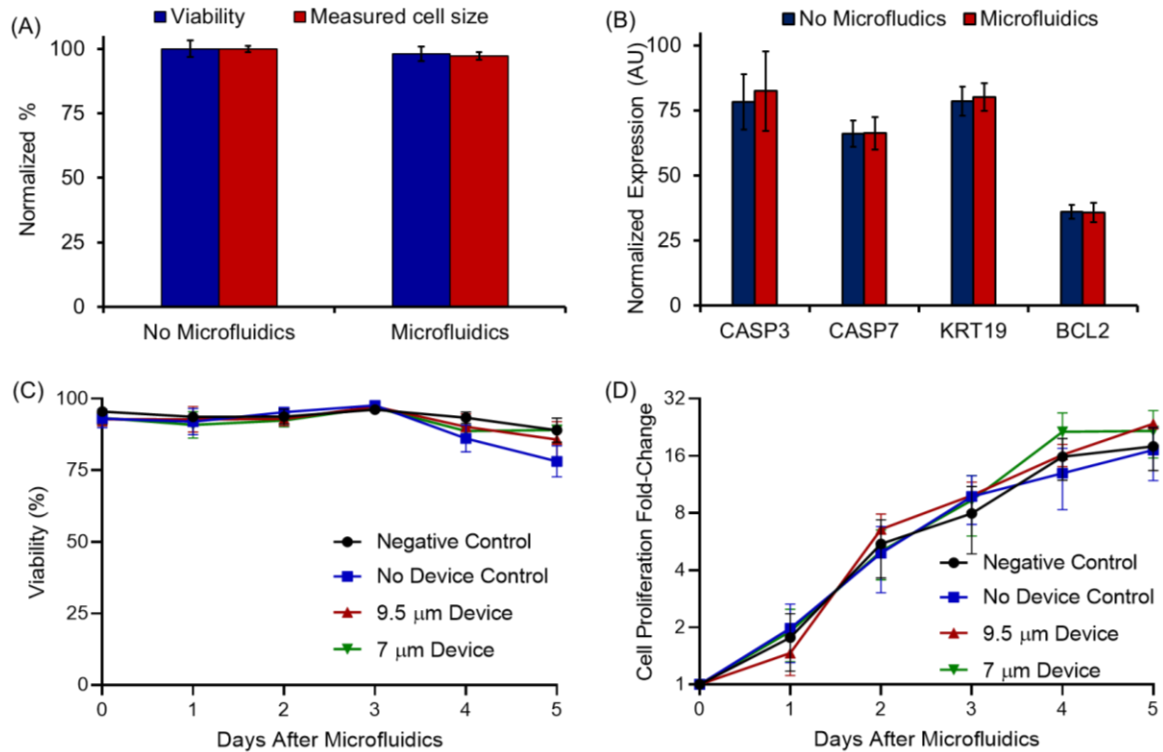
Figure 4.10: Effects of microfluidic compressions on cell viability and function. (A) Measured cell size showed minimal impact by device. Viability stain showed device processing caused <5% cell death, N = 2. (B) Expression of genes related to cell viability and integrity is unaffected by cell VECT. RNA expression of apoptosis-related and cytoskeletal genes is unaffected by the microfluidic cell VECT processing. Expression data was normalized with respect to the highest expressing gene, Casp3, set to ~100%, N = 2. K562 cells in 9 μm gap device used. (C) Cell viability following compression with two different device compression gaps has minimal (<5%) change compared to No Device controls up to 5 days after microfluidics. Note all cell groups, including Negative and No Device controls, showed decreased viability at days 4 and 5 of culture without passaging due to culture overgrowth. N = 3, bars represent SD (D) Cells processed by the device also appear to proliferate at a rate consistent with No Device and Negative controls. Cells in all groups doubled roughly once per day of culture without passaging. N = 3, bars represent SD.

4.3.3   *Intracellular Protein Loss*

To evaluate whether volume loss during rapid compression led to loss of intracellular proteins, we performed a gel electrophoresis analysis and mass spectroscopy

analysis of extracellular fluid after microfluidic processing to search for proteins that

originate from the cell interior. We suspended thrice-washed K562 cells in serum-free flow

buffer and isolated the cells after microfluidic compressions. The cells were removed with

centrifugation and the concentrated extracellular proteins were stained with SYPRO Ruby

protein gel stain (ThermoFisher). Gel imaging revealed that the device groups had very

similar band intensity compared to the No device control. The overall intensity and number

of protein bands was much lower in the device and No device groups compared to the Cell

lysate group (Figure 4.11).
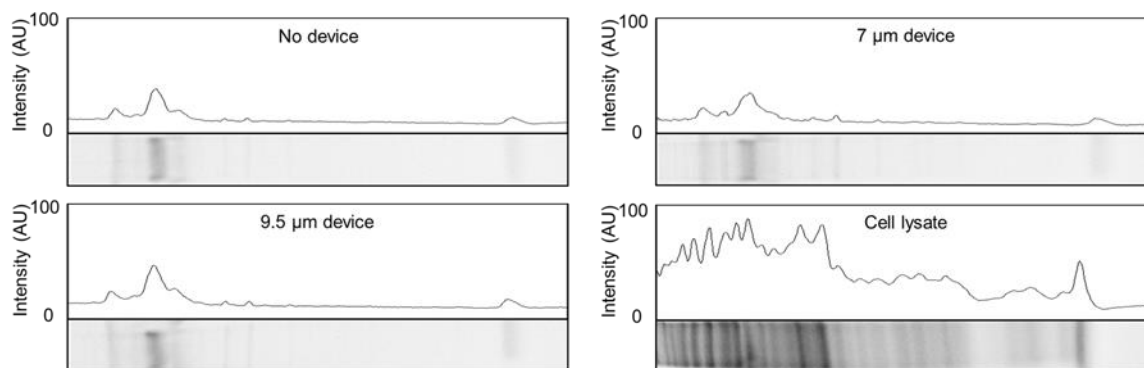
Figure 4.11: Protein gel analysis of proteins lost during cell VECT. Protein in the
extracellular buffer from device-processed K562 cells was concentrated and stained.
Protein gel imaging shows cell samples processed with two different device gap sizes have
very similar protein band intensity profiles to No device control. Cell lysate control group
has a much higher protein content.

The concentrated extracellular protein from device processing was also analyzed

with mass spectrometry to further quantify the type and amount of protein present. The

mass spectrometry results showed the overall peptide-spectrum matches (PSMs) were low

in the device and No device groups (Figure 4.12). The composition of proteins in the buffer

was unchanged in the 9.5 µm gap device compared to the No device group. The 7 µm gap

device group appears to be selectively enriched for certain intracellular proteins,

particularly the cytoskeletal proteins actin and myosin (Table 4.1). Overall the extracellular

buffer of the No device and device groups showed very low PSMs compared to Cell lysate

control, indicating low protein content. The No device group had only 1.6% of the total

PSMs of the Cell lysate control, while the 7 µm and 9.5 µm device had 4.4% and 1.6%

respectively. The overall conclusion is that the amount of protein lost during this

compression-based cell volume loss is not significant, as the results with both protein gel

and mass spectrometry are very similar to the No device control, and much lower than the

Cell lysate control. This conclusion is supported by the maintained cell viability in culture

after processing.
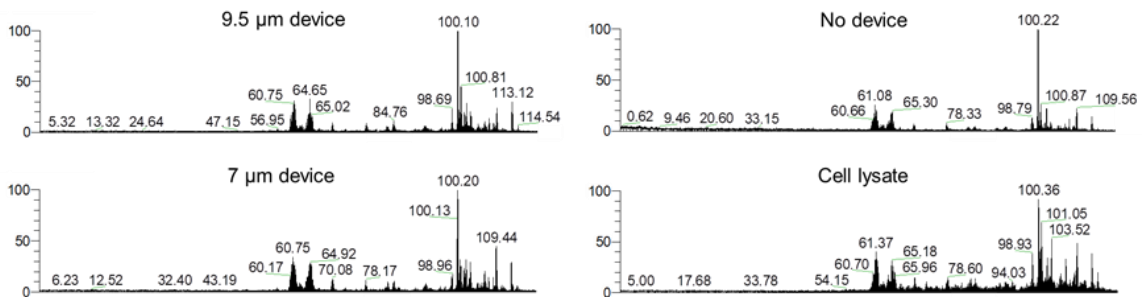
Figure 4.12: Mass spectrometry analysis of proteins lost during cell VECT. Mass spectrometry of the extracellular buffer showed protein composition of device groups similar to No Device, but did identify low levels of intracellular proteins that were differentially expressed in the device groups, especially the smaller compression gap (7 µm). Cell lysate control group has much higher protein content.

Protein	No device [# PSMs]	7 µm device [# PSMs]	9.5 µm device [# PSMs]	Cell lysate [# PSMs]
Actin, alpha skeletal muscle	3	12	3	31
Myosin-1	3	8	3	26
Myosin-3	3	4	3	9
Creatine kinase M-type	2	5	2	13
GAPDH	2	3	2	10
Myosin-4	2	3	2	9
Beta-enolase	1	4	1	15
Actin, cytoplasmic 1	2	2	2	17
Myosin-8	2	2	2	10
Isoform Myosin light chain 1/3	0	4	0	6
Histone H4 OS Homo sapiens	2	0	2	4
Alpha-enolase OS Homo sapiens	0	2	0	25
Myosin-8	0	2	0	5
Total: All proteins	32	86	32	1972

Table 4.1: Identification of intracellular proteins in supernatant. Mass spectrometry was used to identify the protein types present in the supernatant of each sample group. Relative protein abundance is represented by # PSMs (peptide-spectrum matches). In both the No device and device groups, overall protein concentration is low compared to the Cell lysate group (<5% of the total PSMs of the Cell lysate group) indicating low protein content. The No device group had only 1.6% of the total PSMs of the Cell lysate control, while the 7 µm and 9.5 µm device had 4.4% and 1.6% respectively. Protein composition is unchanged in the 9.5 µm device group compared to No device. The 7 µm device group appears to be selectively enriched for certain intracellular proteins, including actin and myosin. Cell lysate was used as a control group, in which >400 different proteins were detected.

To explain the observation of low protein loss, we considered the sponge-like behavior of the cytoskeleton, which is believed to play a role in intracellular solute retention during transmembrane volume transport [37-41]. Cells have also demonstrated to ability to modulate cytosolic ion concentration at a rapid time scale (on the order of seconds). Intracellular ion concentration modulation is achieved through ion exchange across membranes and release of intracellularly stored ions [42-44]. These ion exchange pathways have been shown to correct disturbances to ion homeostasis after membrane

permeabilization, an important function in cell recovery following mechanical injury. Studies of electroporated cells show that Na^+/K^+ pumps promote repolarization and restoration of intracellular Na^+ and K^+ concentrations [45-47]. The observation of low protein content in the extracellular buffer suggests cells recover from compression with minimal lysis or loss of intracellular contents, which is consistent with maintained cell viability, function, and proliferation.

4.4   Summary of Delivery Capabilities and Physiological Impact

This section characterizes both the nature and capabilities of intracellular delivery using cell VECT. Delivery is shown to be convective, and therefore not subject to the limitations in delivery cargo size that have been demonstrated in diffusive delivery [2-7,9]. Delivery using cell VECT is shown to raise intracellular target molecule concentration to ~10–20% of extracellular concentration. Therefore, while convective delivery is shown to be independent of molecule size, it is still limited by the extracellular concentration of the target reagent. The non-endosomal nature of cell VECT delivery allows intracellular cargoes to directly access intracellular interaction sites without being detained and degraded in endosomes [17-20].

Cells also appear to maintain physiological health and function following microfluidic compressions. Nuclear envelop disruption is often associated with DNA damage and genome instability [23,26]. Device-processed cells were shown to maintain nuclear envelop integrity, which would limit access of delivered molecules to the nucleus. It is possible that smaller compression gaps (<20% of average cell diameter) could result

83

in increased nuclear envelop disruption, at the additional cost of cell viability. Loss of intracellular proteins during compression was found to be similar to No device controls and significantly lower than Cell lysate controls. The protein loss studies suggest that there is also minimal loss of other intracellular contents, such as mRNA or organelles, although these studies would need to be performed in order to validate that claim. Overall, these findings are consistent with our observations of minimal impact on cell viability, function, and proliferation [9,11]. These findings help validate future potential applications for cell VECT in both research and clinical settings.

4.5   Methods

4.5.1   Fabrication of Microfluidic Channels

The microfluidic features of this device were molded onto polydimethylsiloxane (PDMS) and plasma bonded to a glass slide. A reusable SU-8 mold was made using standard two-step photolithography on a silicon wafer. To fabricate the devices, a 10:1 ratio of PDMS and crosslinking agent was mixed and poured onto the SU-8 mold to form the microfluidic channel features by replica molding. The PDMS was then degassed in a vacuum chamber and cured for 1 hr at 80°C. The cooled PDMS was then removed from the molds and outlets and inlets were punched using biopsy punches. The PDMS was then bonded to clean glass slides using a plasma bonder (PDC-32G Harrick) followed by 1 hr in a 80°C oven. After cooling, the channels were passivated using 1% bovine serum albumin (BSA) for an overnight incubation at 4°C. For more detailed protocols, please see Appendix A.1.

4.5.2   Microfluidic Experimental Setup

Cells were resuspended in a cell flow buffer consisting of DPBS (-/-) with 0.1% BSA, 0.04% EDTA. Experiments in which video was taken used cell flow buffer with the addition of 25% Percoll to maintain cell suspension in buffer without settling. The cells were isolated from culture media and resuspended in buffer at ~1-5x10^6 cells/mL with the desired concentration of target molecules. Multiple sizes of FITC-dextran were purchased from the same maker (Sigma-Aldrich) with very little variation in labeling fraction. The dextran molecules had an average FITC/dextran molar ratio of 0.00525 ± 0.0017. Our largest molecule, 2000 kDa, had a labeling fraction of 0.006, almost identical with the smallest molecule, 3-5 kDa, labeling fraction of 0.007. We also used the same mass per volume, so the mass of fluorophore in solution is the same across all molecule sizes. The cell-buffer suspension was infused into the microfluidic device at a controlled rate using syringe pumps (PHD 2000, Harvard Apparatus). A cell flow rate of ~100 mm/s through the channel was used unless the flow rate was the independent variable. For delivery experiments, following collection from the outlets, the cells were washed 2X with DPBS (-/-) to remove residual molecules external to the cells. For experiments in which cells were cultured following microfluidics, the microfluidic experiment was conducted inside a sterile biosafety cabinet. All cell-handling supplies, including the device, syringe, and needles, were sterilized by autoclaving.

4.5.3   Cell Culture

K562 cells from ATCC were cultured in RPMI-1640 supplemented with 10% fetal bovine serum (FBS) and 1% penicillin-streptomycin. HEK-293 cells, a generous gift from

Lammerding lab, were cultured in EMEM with 10% FBS and 1% penicillin-streptomycin and passaged using 0.25% Trypsin-EDTA. Adipose tissue-derived stem cells were harvested from knee joints of Goettingen minipigs. <1mm^3 tissue samples from the infrapatellar fat pad were collected, placed in type I collagenase (1.5mg/mL, Sigma Aldrich) for dissociation, centrifuged and then cultured in adipose-derived stem cell specific media. The cultured cells were characterized with specific surface markers for ADSCs according to the International Society for Cell Therapy (ISCT) criteria, including CD29, CD44, CD71, CD90, CD105/SH2, SH3 and STRO-1 with lack of CD31, CD45 and CD106. The cells were incubated at 37°C with 5% CO_2.

4.5.4   Flow Cytometry

The BD Accuri C6 Flow Cytometer was used to characterize cell uptake of fluorescent target molecules. Samples processed with FITC-dextran were excited with a 488 nm wavelength laser and emission was detected with a 533/30 filter. Fluorescence intensity was normalized with respect to the highest intensity group. The viability of the cells immediately after microfluidics was tested by staining with 2 µM EthD-1 (Molecular Probes Inc.) solution per manufacturer protocol [48,49] (640 nm excitation and 670 LP filter). The long term viability of the cells was tested by propidium iodide staining per manufacturer protocol and excited with a 488 nm wavelength laser and emission was detected with a 670 LP filter.

4.5.5   Plasmids and Generation of Fluorescently Labeled Cell Lines

HEK-293-TN (System Biosciences, SBI) cells were stably modified with lentiviral vectors to express the nuclear rupture reporter NLS-GFP (pCDH-CMV-NLS-copGFP-

EF1-blastiS) and/or cGAS-mCherry (pCDH-CMV-cGAS$^{E225A/D227A}$-mCherry2-EF1-Puro) [23]. cGAS is a cytosolic DNA binding protein; we used a cGAS mutant (E225A/D227A) with abolished enzyme activity and interferon production, but that still binds DNA and serve as a nuclear envelope rupture reporter [50]. To generate stable lines, pseudoviral particles were produced as described previously [23]. In brief, HEK-293-TN cells (System Biosciences, SBI) were co-transfected with the lentiviral plasmid, packaging and envelope plasmids using PureFection (SBI), following manufacturer protocol. Lentivirus-containing supernatants were collected at 48 hours and 72 hours after transfection and filtered through a 0.45 µm filter. Cells were seeded into 6-well plates so that they reached 50-60% confluency on the day of infection and transduced with the viral supernatant in the presence of 8 µg/mL polybrene (hexadimethrine bromide). After 24 hours, the viral solution was replaced with fresh culture medium, and cells were cultured for 72 hours before selection with 1 µg/mL of puromycin or 2 µg/mL blasticidin S for 2-5 days. After selection, cells were subcultured and maintained in their recommended medium without the continued use of selection agents.

4.5.6 Electroporation

Electroporation of HEK-293 cells was carried out using an Amaxa Nucleofector II and Amaxa Cell Line Nucleofector Kit V using manufacturer protocols. Cells were electroporated using Nucleofector Program Q-001 in a 100 µL Amaxa cuvette.

4.5.7 Confocal Microscopy

Confocal microscopy of fixed K562 cells and HEK-293 cells was done using the Zeiss LSM 700. The K562 and HEK-293 cells were stained with Hoechst nucleus stain

(405 nm excitation and 300-629 nm detection) per manufacturer protocol. After processing, cells were fixed with 4% PFA, resuspended in imaging buffer (RPMI-1640 plus 1 mg/mL ascorbic acid), and mounted onto glass coverslips using clear nail polish for imaging. HEK-293 cells were imaged with a 40X oil lens to analyze the expression of NLS-GFP and cGAS-mCherry. A 63X Apochromat oil lens was used to image fixed K562 cells delivered with Cy5-mRNA (639 nm excitation and 629-800 nm detection). Confocal microscopy of live cells with tetramethylrhodamine (TRITC)-dextran (555 nm excitation and 560-800 nm detection) was performed using the Zeiss LSM 700. The Zeiss 710 NLO with a 40X water lens was used to image live K562 cells with 100 nm nanoparticles (514 nm excitation and 527-601 nm detection) (ThermoFisher) and live K562 cells stained with DiO membrane stain and Hoechst nucleus stain and delivered with Cy3-labled non-coding plasmid.

4.5.8   Confocal Image Analysis

Using Zen Lite software by Zeiss International, the raw fluorescence values from the Hoechst stain channel was exported as an 8-bit tag image file format (TIFF) image. The Hoechst image stacks were then imported into ImageJ and the fluorescence profile was modulated by a threshold intensity value of 20 to reduce background fluorescence. The outer edges of the stained areas were found, and using a circular profile estimator, the areas of the cell nuclei could be calculated for each layer. The cell area data was organized and averaged using MATLAB. Cells in which NLS-GFP has left the nucleus were identified by the presence of GFP fluorescence signal outside the Hoechst stained nucleus area. In determining the presence of a nuclear breach, the fluorescence data from the cGAS-mCherry was modulated by increasing the multiplier for the intensity values for ease of viewing. Positive nuclear disruption was marked by small areas of higher intensity

mCherry fluorescence or marked by an outline of the nucleus by a ring of higher mCherry fluorescence intensity. Cells that presented these mCherry fluorescence signals were counted towards positive nuclear disruption and paired with the calculated average cell area for that cell.

4.5.9 Protein Gel

K562 cells were washed 3X with PBS (-/-) to remove serum protein and resuspended in serum-free RPMI-1640 at $2x10^6$ cells/mL. For the Cell lysate control, cells were mixed with Halt™ Protease Inhibitor Cocktail, EDTA-Free (ThermoFisher), then underwent a 30-second liquid nitrogen snap freeze before thawing on ice for 10 minutes. The freeze-thaw process was repeated 5X. Cell lysate was centrifuged at 20,000xg for 15 min at 15°C and the supernatant was collected. Cells were processed with 7 and 9.5 µm gap microfluidic devices, plus a No device control. Device and No device samples, 2.5 mL each, were centrifuged at 200xg. 1.5 mL of supernatant was collected and centrifuged again. Only 1 mL of supernatant was collected to avoid contamination from cell debris. All samples were mixed with protease inhibitor and then concentrated 10-fold using a Vivaspin® 5 kDa molecular weight cut-off spin concentrator (Sigma-Aldrich). Supernatant proteins were characterized by protein gel electrophoresis using pre-cast SDS-polyacrylamide gel (Bio-Rad) according to manufacturer protocol. Sample loaded gel was run at constant voltage 200V. Gel was stained with SYPRO Ruby protein gel stain (Thermo Fisher) according to manufacturer protocol. Stained gel was imaged on a Bio-Rad ChemiDoc imager.

4.5.10 Mass Spectrometry

The proteins in each sample were reduced, alkylated and digested with trypsin according to the FASP protocol [51]. The peptides were analyzed by nano-LC-MS/MS, and peptide identification as previously described with the following modifications [52]. Reverse phase chromatography was performed using an in-house packed column (40 cm long X 75 µm ID X 360 OD, Dr. Maisch GmbH ReproSil-Pur 120 C18-AQ 1.9 µm beads) and a 120 min gradient. The Raw files were searched using the Mascot algorithm (ver. 2.5.1) against a protein database constructed by combining the human UniProt protein database (downloaded April 24, 2018, 20,303 entries), and a contaminant database (cRAP, downloaded 11-21-16 from http://www.thegpm.org) via Proteome Discoverer 2.1. Only peptide spectral matches with expectation value of less than 0.01 ("High Confidence") were used.

4.6   References

[1]   Sharei, A. *et al.* Cell squeezing as a robust, microfluidic intracellular delivery platform. *J. Visualized Exp.*, e50980, doi:10.3791/50980 (2013).

[2]   Sharei, A. *et al.* Plasma membrane recovery kinetics of a microfluidic intracellular delivery platform. *Integr. Biol.* **6**, 470-475, doi:10.1039/c3ib40215k (2014).

[3]   Hallow, D. M. *et al.* Shear-induced intracellular loading of cells with molecules by controlled microfluidics. *Biotechnol. Bioeng.* **99**, 846-854, doi:10.1002/bit.21651 (2008).

[4]   Sharei, A. *et al.* Ex vivo cytosolic delivery of functional macromolecules to immune cells. *PLoS One.* **10**, e0118803, doi:10.1371/journal.pone.0118803 (2015).

[5]   Szeto, G. L. *et al.* Microfluidic squeezing for intracellular antigen loading in polyclonal B-cells as cellular vaccines. *Sci. Rep.* **5**, 10276, doi:10.1038/srep10276 (2015).

[6]   Ding, X. *et al.* High-throughput nuclear delivery and rapid expression of DNA via mechanical and electrical cell-membrane disruption. *Nat. Biomed. Eng.* **1**, 0039, doi:10.1038/s41551-017-0039   http://www.nature.com/articles/s41551-017-0039#supplementary-information (2017).

[7]   Saung, M. T. *et al.* A Size-Selective Intracellular Delivery Platform. *Small.* doi:10.1002/smll.201601155 (2016).

[8]   Jones, W. R. *et al.* Alterations in the Young's modulus and volumetric properties of chondrocytes isolated from normal and osteoarthritic human cartilage. *J. Biomech.* **32**, 119-127, doi:Doi 10.1016/S0021-9290(98)00166-3 (1999).

[9]   Liu, A. *et al.* Microfluidic generation of transient cell volume exchange for convectively driven intracellular delivery of large macromolecules. *Mater. Today.* **21**, 703-712, doi:10.1016/j.mattod.2018.03.002 (2018).

[10]   Trickey, W. R., Baaijens, F. P. T., Laursen, T. A., Alexopoulos, L. G. & Guilak, F. Determination of the Poisson's ratio of the cell: recovery properties of chondrocytes after release from complete micropipette aspiration. *J. Biomech.* **39**, 78-87, doi:10.1016/j.jbiomech.2004.11.006 (2006).

[11]   Liu, A. *et al.* Cell Mechanical and Physiological Behavior in the Regime of Rapid Mechanical Compressions that Lead to Cell Volume Change. *Small.* e1903857, doi:10.1002/smll.201903857 (2019).

[12]   Kizer, M. E. *et al.* Hydroporator: a hydrodynamic cell membrane perforator for high-throughput vector-free nanomaterial intracellular delivery and DNA origami biostability evaluation. *Lab Chip.* **19**, 1747-1754, doi:10.1039/c9lc00041k (2019).

[13]   Ramaswamy, B. Finite element solution for advection and natural convection flows. *Computers & Fluids.* **16**, 349-388, doi:https://doi.org/10.1016/0045-7930(88)90023-0 (1988).

[14]   Manzini, G. & Russo, A. A finite volume method for advection–diffusion problems in convection-dominated regimes. *Computer Methods in Applied Mechanics and Engineering.* **197**, 1242-1261, doi:https://doi.org/10.1016/j.cma.2007.11.014 (2008).

[15]   Nejadnik, H., Jung, K. O., Theruvath, A. J., Kiru, L., Liu, A., Wu, W., Sulchek, T., Pratx, G., Daldrup-Link, H. E. Instant labeling of therapeutic cells for multimodality imaging. *Theranostics.* doi:10.7150/thno.39554 (2020).

[16]   Sharei, A. *et al.* A vector-free microfluidic platform for intracellular delivery. *Proc. Natl. Acad. Sci. U. S. A.* **110**, 2082-2087, doi:10.1073/pnas.1218705110 (2013).

[17]   Meacham, J. M., Durvasula, K., Degertekin, F. L. & Fedorov, A. G. Physical methods for intracellular delivery: practical aspects from laboratory use to

industrial-scale processing. *J. Lab Autom.* **19**, 1-18, doi:10.1177/2211068213494388 (2014).

[18] Zorko, M. & Langel, Ü. Cell-penetrating peptides: mechanism and kinetics of cargo delivery. *Adv. Drug Delivery Rev.* **57**, 529-545, doi:http://dx.doi.org/10.1016/j.addr.2004.10.010 (2005).

[19] Joliot, A. & Prochiantz, A. Transduction peptides: from technology to physiology. *Nat. Cell Biol.* **6**, 189-196 (2004).

[20] Bechara, C. & Sagan, S. Cell-penetrating peptides: 20 years later, where do we stand? *FEBS Letters.* **587**, 1693-1702, doi:10.1016/j.febslet.2013.04.031 (2013).

[21] Kirschman, J. L. *et al.* Characterizing exogenous mRNA delivery, trafficking, cytoplasmic release and RNA-protein correlations at the level of single cells. *Nucleic Acids Res.*, doi:10.1093/nar/gkx290 (2017).

[22] Remaut, K., Oorschot, V., Braeckmans, K., Klumperman, J. & De Smedt, S. C. Lysosomal capturing of cytoplasmic injected nanoparticles by autophagy: an additional barrier to non viral gene delivery. *J Control Release.* **195**, 29-36, doi:10.1016/j.jconrel.2014.08.002 (2014).

[23] Denais, C. M. *et al.* Nuclear envelope rupture and repair during cancer cell migration. *Science.* **352**, 353-358, doi:10.1126/science.aad7297 (2016).

[24] Guilak, F., Tedrow, J. R. & Burgkart, R. Viscoelastic properties of the cell nucleus. *Biochem. Biophys. Res. Commun.* **269**, 781-786, doi:10.1006/bbrc.2000.2360 (2000).

[25] Kizer, M. E. *et al.* Hydroporator: a hydrodynamic cell membrane perforator for high-throughput vector-free nanomaterial intracellular delivery and DNA origami biostability evaluation. *Lab on a Chip.* doi:10.1039/C9LC00041K (2019).

[26] Isermann, P. & Lammerding, J. Consequences of a tight squeeze: Nuclear envelope rupture and repair. *Nucleus.* **8**, 268-274, doi:10.1080/19491034.2017.1292191 (2017).

[27] Lim, S., Quinton, R. J. & Ganem, N. J. Nuclear envelope rupture drives genome instability in cancer. *Mol. Biol. Cell.* **27**, 3210-3213, doi:10.1091/mbc.E16-02-0098 (2016).

[28] Zhang, Q. *et al.* Local, transient tensile stress on the nuclear membrane causes membrane rupture. *Mol. Biol. Cell.* **30**, 899-906, doi:10.1091/mbc.E18-09-0604 (2019).

[29] Raab, M. *et al.* ESCRT III repairs nuclear envelope ruptures during cell migration to limit DNA damage and cell death. *Science.* **352**, 359-362, doi:10.1126/science.aad7611 (2016).

[30]   De Vos, W. H. *et al.* Repetitive disruptions of the nuclear envelope invoke temporary loss of cellular compartmentalization in laminopathies. *Hum. Mol. Genet.* **20**, 4175-4186, doi:10.1093/hmg/ddr344 (2011).

[31]   Barbee, K. A. Mechanical cell injury. *Ann N Y Acad Sci.* **1066**, 67-84, doi:10.1196/annals.1363.006 (2005).

[32]   Geddes, D. M., Cargill, R. S., 2nd & LaPlaca, M. C. Mechanical stretch to neurons results in a strain rate and magnitude-dependent increase in plasma membrane permeability. *J Neurotrauma.* **20**, 1039-1049, doi:10.1089/089771503770195885 (2003).

[33]   Farkas, O., Lifshitz, J. & Povlishock, J. T. Mechanoporation induced by diffuse traumatic brain injury: an irreversible or reversible response to injury? *J Neurosci.* **26**, 3130-3140, doi:10.1523/JNEUROSCI.5119-05.2006 (2006).

[34]   Whalen, M. J. *et al.* Acute plasmalemma permeability and protracted clearance of injured cells after controlled cortical impact in mice. *J Cereb Blood Flow Metab.* **28**, 490-505, doi:10.1038/sj.jcbfm.9600544 (2008).

[35]   Wang, W., Huang, Y., Grujicic, M. & Chrisey, D. B. Study of Impact-Induced Mechanical Effects in Cell Direct Writing Using Smooth Particle Hydrodynamic Method. *Journal of Manufacturing Science and Engineering.* **130**, doi:10.1115/1.2896118 (2008).

[36]   Kilinc, D., Gallo, G. & Barbee, K. A. Mechanically-induced membrane poration causes axonal beading and localized cytoskeletal damage. *Exp Neurol.* **212**, 422-430, doi:10.1016/j.expneurol.2008.04.025 (2008).

[37]   DiTommaso, T. *et al.* Cell engineering with microfluidic squeezing preserves functionality of primary immune cells in vivo. *Proc. Natl. Acad. Sci. U. S. A.* **115**, E10907-E10914, doi:10.1073/pnas.1809671115 (2018).

[38]   Islam, M. *et al.* Microfluidic Sorting of Cells by Viability Based on Differences in Cell Stiffness. *Sci. Rep.* **7**, 1997, doi:10.1038/s41598-017-01807-z (2017).

[39]   Chao, P. C., Sivaselvan, M. & Sachs, F. Cytoskeletal Contribution to Cell Stiffness Due to Osmotic Swelling; Extending the Donnan Equilibrium. *Curr. Top. Membr.* **81**, 83-96, doi:10.1016/bs.ctm.2018.07.002 (2018).

[40]   Taber, L. A., Shi, Y., Yang, L. & Bayly, P. V. A Poroelastic Model for Cell Crawling Including Mechanical Coupling between Cytoskeletal Contraction and Actin Polymerization. *J. Mech. Mater. Struct.* **6**, 569-589, doi:10.2140/jomms.2011.6.569 (2011).

[41]   Sachs, F. & Sivaselvan, M. V. Cell volume control in three dimensions: Water movement without solute movement. *J. Gen. Physiol.* **145**, 373-380, doi:10.1085/jgp.201411297 (2015).

[42]   Atwater, I., Dawson, C. M., Ribalet, B. & Rojas, E. Potassium permeability activated by intracellular calcium ion concentration in the pancreatic beta-cell. *J. Physiol.* **288**, 575-588 (1979).

[43]   Nguyen, T., Chin, W. C. & Verdugo, P. Role of Ca2+/K+ ion exchange in intracellular storage and release of Ca2+. *Nature.* **395**, 908-912, doi:10.1038/27686 (1998).

[44]   Muallem, S., Zhang, B. X., Loessberg, P. A. & Star, R. A. Simultaneous recording of cell volume changes and intracellular pH or Ca2+ concentration in single osteosarcoma cells UMR-106-01. *J. Biol. Chem.* **267**, 17658-17664 (1992).

[45]   Gissel, H. Effects of varying pulse parameters on ion homeostasis, cellular integrity, and force following electroporation of rat muscle in vivo. *Am. J. Physiol.: Regul., Integr. Comp. Physiol.* **298**, R918-929, doi:10.1152/ajpregu.00692.2009 (2010).

[46]   Clausen, T. Na+-K+ pump stimulation improves contractility in damaged muscle fibers. *Ann. N. Y. Acad. Sci.* **1066**, 286-294, doi:10.1196/annals.1363.021 (2005).

[47]   Clausen, T. & Gissel, H. Role of Na,K pumps in restoring contractility following loss of cell membrane integrity in rat skeletal muscle. *Acta Physiol. Scand.* **183**, 263-271, doi:10.1111/j.1365-201X.2004.01394.x (2005).

[48]   Barron, J. A., Ringeisen, B. R., Kim, H. S., Spargo, B. J. & Chrisey, D. B. Application of laser printing to mammalian cells. *Thin Solid Films.* **453**, 383-387, doi:10.1016/j.tsf.2003.11.161 (2004).

[49]   Zhou, H. M. *et al.* In vitro cytotoxicity of calcium silicate-containing endodontic sealers. *J Endod.* **41**, 56-61, doi:10.1016/j.joen.2014.09.012 (2015).

[50]   Civril, F. *et al.* Structural mechanism of cytosolic DNA sensing by cGAS. *Nature.* **498**, 332-337, doi:10.1038/nature12305 (2013).

[51]   Wisniewski, J. R., Zougman, A., Nagaraj, N. & Mann, M. Universal sample preparation method for proteome analysis. *Nat. Methods.* **6**, 359-362, doi:10.1038/nmeth.1322 (2009).

[52]   Rinker, T. E. *et al.* Microparticle-mediated sequestration of cell-secreted proteins to modulate chondrocytic differentiation. *Acta Biomaterialia.* doi:https://doi.org/10.1016/j.actbio.2017.12.038 (2017).

CHAPTER 5.   APPLICATIONS FOR CELL ENGINEERING

5.1   Introduction

The field of cell engineering is experiencing rapid growth due to the development of cell-based immunotherapies. Cell engineering techniques are used to modify or analyze the cell physiological state for diagnostic or therapeutic applications. Intracellular delivery and analysis of intracellular molecular probes allows for characterization of cell physiological processes. Gene expression probes delivered to the intracellular space allow for analysis of gene expression in live cells that does not rely on cell surface expression [1,2]. Modification of the cell physiological state can occur through transient transfection of cells through the delivery of plasmids and mRNA that cause temporary expression of an exogenous gene without altering the cell genome. Permanent modification of cell gene expression can be achieved through the delivery of gene editing reagents [3-6]. Overall, methods to analyze cell physiological processes and modify cell gene expression are invaluable tools for cell engineering. The demand for these techniques continues to grow as the field of cell engineering expands in both research and clinical settings.

Cell engineering techniques for modification and analysis of the cell state often require the intracellular delivery of large macromolecules, including plasmids, mRNA, nuclease complexes, and nanoparticle constructs. However, existing cell engineering techniques do not meet the growing demands for efficient processing of highly functional and viable cell products. The current standard approach is viral transduction, an expensive technique that has long-standing safety concerns [7-13]. The viral packing limits of the two most commonly used viral vectors are 5 kb for adeno-associated virus and 9 kb for

lentivirus [14,15], which impedes the application of viral transduction for next-generation cell therapies that require the delivery of larger genetic constructs and multiple gene edits [16,17]. Non-viral approaches such as electroporation are not effective for all molecule types of interest and can lead to inconsistent delivery with low viability and proliferation of cellular products, making this technique not ideally suited for cell therapy manufacture [9,18,19].

This thesis presents a convective mechanism, called cell VECT, for macromolecule delivery to cells to meet the growing demands of cell manufacturing and enable a new realm of applications for intracellular molecule delivery using microfluidics. During cell VECT processing, abrupt compressions cause the cell to change in shape and reduce in volume. Immediately following this brief cell volume loss, the cell automatically returns to its pre-compression shape and volume, causing the cell to uptake surrounding solution and any molecules suspended therein. This method utilizes this unique cell volume exchange phenomenon as a mechanism to deliver macromolecules into the cell on convective bulk flow currents, rather than diffusion alone. Cells processed using cell VECT have been shown to maintain high viability and proliferation [20,21].

Therefore, convective intracellular delivery of large macromolecules using cell VECT has the potential to serve as a useful platform for various cell engineering applications. These applications include intracellular gene expression analysis, temporary exogenous gene expression, and permanent endogenous gene editing. In this aim, we will explore applications in intracellular labeling and analysis by delivering mRNA nanoparticle probes to analyze intracellular gene expression in living cells. We will also validate the application of cell VECT for both temporary and permanent gene expression

modification through the delivery of mRNA, plasmids, and gene editing reagents. Overall, our objective is to establish potential applications for cell VECT for various use cases in cell engineering.

5.2 Intracellular Gene Expression Analysis

A major application for intracellular molecule delivery is the analysis of gene expression in live cells. Current standard methods of analyzing intracellular gene expression require the cell to be lysed in order to extract DNA, RNA, or proteins for analysis. These methods are not capable of providing information on the localization of the gene expression or the trends in gene expression over time because the cell is no longer viable after processing [22,23]. Methods in which cells are fixed and permeabilized for intracellular gene labeling similarly cannot track temporal variation of gene expression [22,23]. Gene expression assays of live cells are typically limited to analysis of genes expressed on the cell surface, whereas the vast majority of genes are expressed in the cell interior. Therefore, methods for real-time analysis of intracellular gene expression in living cells are invaluable tools for the study of cell biology [22,23].

Towards this objective, a family of RNA-based probes called nano-flares have been developed for intracellular analysis of RNA expression in live cells [1,2,22,23]. These nano-flare probes must be able to interact with the cell interior in an unencapsulated manner in order to access the cytosol and bind with their target RNA. Therefore, a non-endosomal method of delivering RNA probes would be advantageous for real-time labeling and analysis of intracellular RNA in live cells. We tested the cell VECT platform's potential

applications for intracellular labeling and analysis of gene expression by delivering SmartFlare Live Cell RNA probes (Millipore). The SmartFlare is a type of RNA-based nanoflare probe that consists of a gold nanoparticle conjugated with oligonucleotides and quenched fluorophores. When the SmartFlare binds its target mRNA, the fluorophore is released as a fluorescent indicator of target mRNA expression (Figure 5.1A) [1,2]. This method of gene expression analysis allows for detection of gene expression at the RNA level, and facilitates analysis of intracellularly expressed genes in living cells, unlike traditional surface labeling and cell lysate assays.

Our experiments delivered SmartFlare probes to detect GAPDH mRNA in K562 cells and adherent PC3 prostate cancer cells. Delivery of the SmartFlare probe to PC3 cells was competitive with the established method of 24 hr endocytosis, and was completed in less than 30 mins (Figure 5.1B). The rapid nature of cell VECT delivery allows for a more immediate readout of gene expression, rather than an overnight incubation. Furthermore, it has been shown that not all cells will endocytose SmartFlare particles. K562 cells, which do not uptake SmartFlare particles through endocytosis, showed successful delivery using cell VECT (Figure 5.1C). Our success in delivering to PC3 and K562 cells demonstrated this method's robustness for delivery to both adherent and nonadherent cells, and cells that do not uptake this particle through endocytosis. These delivery capabilities would expand the applications of intracellular live-cell gene expression assays to a wider range of use cases and cell types.
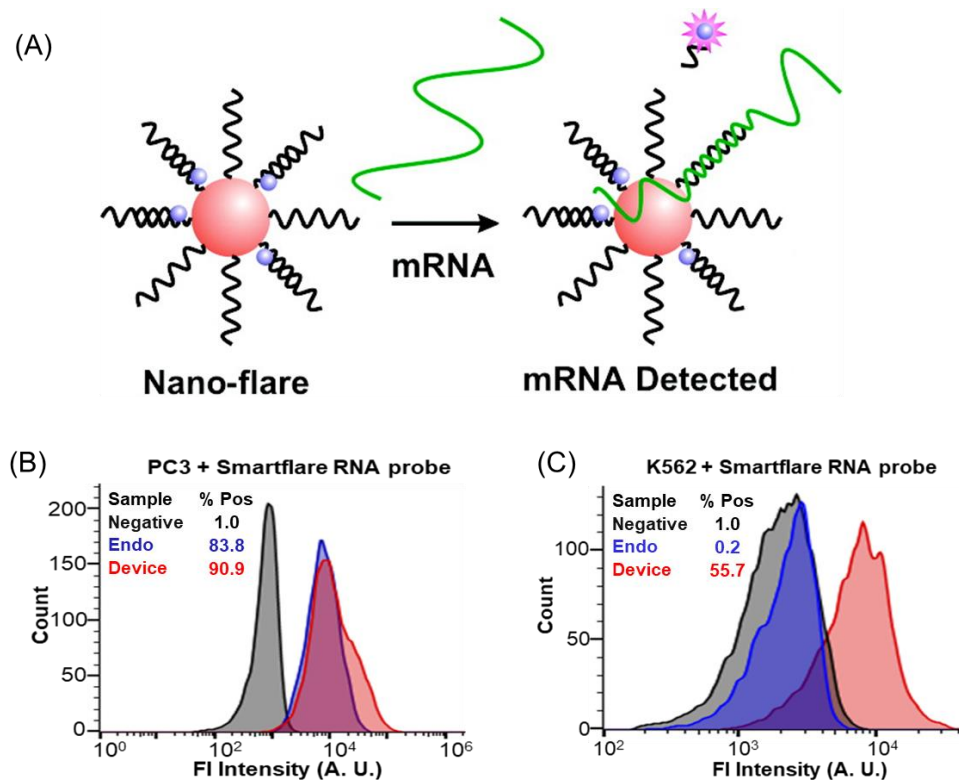
Figure 5.1: Intracellular delivery of nano-flare RNA probes. (A) Schematic of the mode of function of nano-flares. A gold nanoparticle is conjugated to oligonucleotides and quenched fluorophores. When the oligonucleotides bind a target mRNA, the fluorophore is released as a fluorescent indicator of gene expression. Figure reproduced with permission from reference [1]. (B) Cell VECT device intracellular delivery of SmartFlare nano-flare RNA probes to PC3 cells was competitive with the established standard method of 24 hr endocytosis. (C) The cell VECT device successfully delivered SmartFlare to K562 cells, which do not endocytose SmartFlares, which enables this probe to be usable with cells regardless of endocytic properties. Cells were processed with SmartFlare concentration of 100 pM.

An additional failure mode of nanoparticle-based intracellular probes that are delivered by endocytosis is endosomal degradation. Degradation of the nano-flare can result in fluorescent signal release even without binding of the target mRNA, resulting in a false positive fluorescent readout that can compromise the accuracy of this gene expression assay [24,25]. This degradation results in a scramble control readout that has

the same intensity profile as the target mRNA readout (Figure 5.2A). The non-endosomal

nature of cell VECT delivery allows the delivered particles to interact with mRNA in the

cytosol without the need to escape the primary endosome. Therefore the fluorescent probe

is not degraded due to cell VECT delivery, resulting in a target mRNA readout signal that

is higher than the scramble control (Figure 5.2B). Furthermore, the fluorescent readout is

detectable immediately after delivery with cell VECT, whereas endocytosis must be

analyzed 24 hrs later.
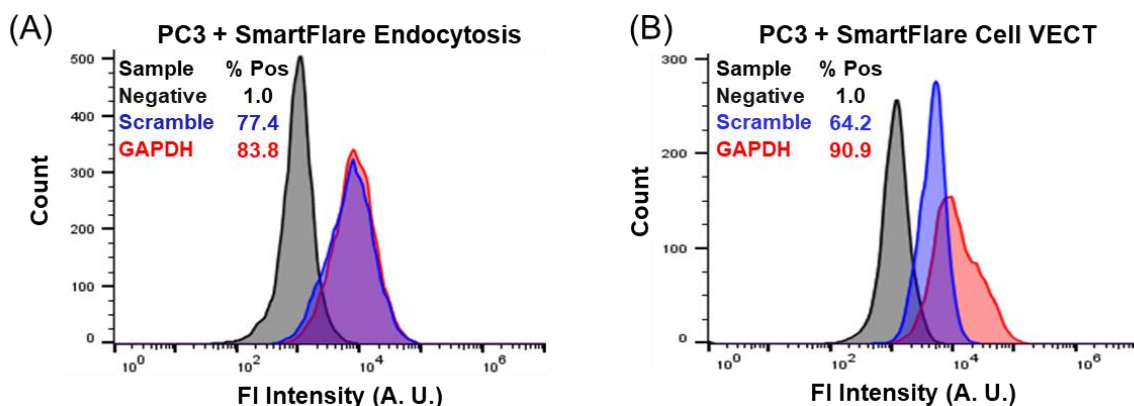
Figure 5.2: Non-endosomal delivery of nano-flare RNA probes prevents probe degradation. (A) Endosomal delivery of SmartFlare RNA probes results in probes being detained and degraded in the endosomes, causing a Scramble control signal that is indistinguishable from the gene readout signal (GAPDH). (B) Non-endosomal delivery using cell VECT results in SmartFlare localization to the cytosol, which avoids endosomal degradation and results in a Scramble control signal that is significantly lower than the GAPDH gene readout signal. Cells were processed with SmartFlare concentration of 100 pM.

5.3   Modification of Cell Gene Expression

Modification of cell gene expression is vital for both the study of various cell

processes and the manufacture of life-saving cell therapies. Cell engineering techniques to

modify cell gene expression profile can have temporary effects, through the delivery of transiently expressed mRNA or plasmids, or permanent effects through genome editing. The various cell engineering techniques, both temporary and permanent, usually require the delivery of reagents for cell transfection or gene editing, which are often large molecules such as plasmids or mRNA. The use of cell VECT for research and clinical applications can address important limitations of other microfluidic delivery platforms, particularly those that primarily use diffusive transport. Since diffusive transport is limited in the size of molecules that it can efficiently deliver, this presents a challenge in delivering these large cell engineering reagents. Convective transport does not have the size limitations inherent to diffusive transport [20,21,26], and is therefore a more efficient driving mechanism for the delivery of larger macromolecules for cell engineering.

5.3.1   *Temporary transfection through delivery of mRNA and plasmid*

Intracellular delivery of mRNA can be used to study and transiently express exogenous genes. Transfection using mRNA results in gene expression that is independent of cell cycle and has a more immediate gene expression readout than plasmid, since the mRNA can be directly translated and expressed in the cytoplasm without entering the nucleus. Unlike plasmid, expression of the gene encoded in the mRNA can easily be tuned by adjusting the amount of mRNA delivered [10]. Intracellular delivery of mRNA is also useful in immunotherapy applications, including loading dendritic cells with tumor antigens encoded in mRNA as a form of vaccination to elicit a targeted T-cell response [27].

To demonstrate the capabilities of cell VECT as a delivery platform for mRNA, we successfully delivered EGFP mRNA (TriLink) to K562 cells as a proof of concept experiment for transient expression of an exogenous gene (Figure 5.3A). The delivered EGFP mRNA construct measured 996 bases in length, or approximately 320 kDa in mass, which demonstrates the ability of cell VECT to deliver large macromolecules that will function and influence gene expression in the cell. We also successfully transfected primary peripheral blood mononuclear cells (PBMCs) with EGFP mRNA (Figure 5.3B). By demonstrating transfection in primary PBMCs, we exhibit the ability of cell VECT to successfully process a primary, heterogeneous cell population that is of therapeutic relevance.
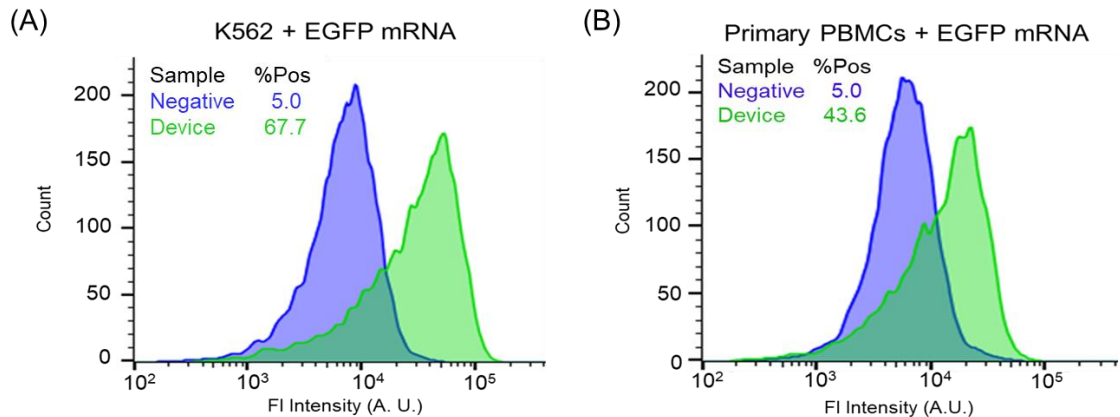
Figure 5.3: Transient exogenous gene expression by mRNA delivery. (A) Fluorescent expression signal of EGFP in K562 cell line following delivery of EGFP mRNA. K562s were processed in a microfluidic device with 9 μm compression gap. (B) Expression of EGFP in primary PBMCs delivered with EGFP mRNA. PBMCs were processed in a microfluidic device with 6.5 μm compression gap. Cells were processed with 100 μg/mL EGFP mRNA.

Transfection through intracellular delivery of non-integrating plasmids is another method of temporary transfection. These non-integrating plasmids must enter the nucleus in order for the encoded genes to be expressed, which results in a longer lead time to expression. However, gene expression using transfected plasmids can persist for several days longer than that of transfected mRNA [10]. We validate the application of cell VECT for temporary plasmid transfection by delivering EGFP plasmid (OZ Biosciences) (Figure 5.4). We demonstrated gene expression of EGFP in K562 cells after delivery of an EGFP plasmid that is 5781 basepairs in length, or approximately 3,500 kDa in mass. This result exhibits the ability of cell VECT technology to deliver very large and functional cargoes that influence cell gene expression, a useful capability for both clinical and research settings.

We do note that EGFP expression through plasmid delivery is lower than that observed by EGFP mRNA delivery. This is likely because plasmid must reach the cell nucleus in order to be expressed. We determined that cell VECT has minimal impact on nuclear envelop integrity [21]. Therefore, the delivered plasmid can only access the nucleus when the nuclear envelop is disrupted during cell division, which could result in a lower EGFP expression for the delivered plasmids.
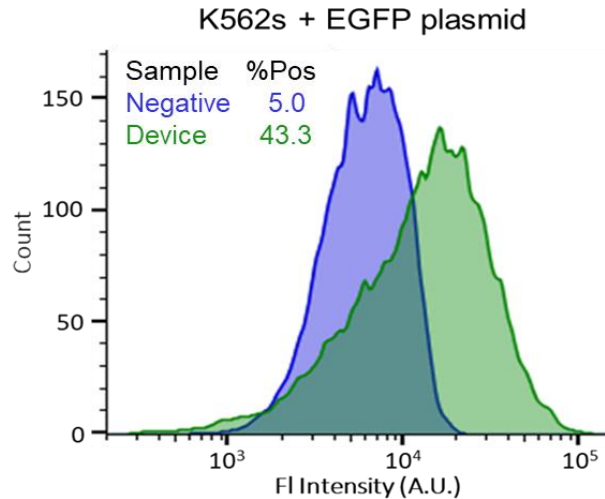
Figure 5.4: Transient exogenous gene expression by plasmid delivery. EGFP expression proof of concept results after EGFP plasmid delivery to K562 cells. K562s were processed in a microfluidic device with 9 μm compression gap, 60 μg/mL EGFP plasmid, at 200 μL/min flow rate.

5.3.2   Permanent Endogenous Gene Knockout

Permanent modification of cell gene expression can be achieved through the intracellular delivery of genome editing reagents, such as CRISPR-Cas9 complexes. CRISPR-Cas9 was discovered in bacteria, which use clustered regularly interspaced short palindromic repeat (CRISPR) DNA sequences retained from previous bacteriophage infections to recognize and cleave viral DNA to prevent new infections [28-30]. This discovery was adapted into the CRISPR-Cas9 gene editing technology, wherein the CRISPR associated protein 9 (Cas9) nuclease is complexed to a guide RNA (gRNA) to form the CRISPR-Cas9 ribonucleoprotein (RNP) complex. The gRNA targets the RNP complex to a specified DNA sequence, and the Cas9 nuclease cuts at this location to permanently disrupt the encoded gene [28-30].

To demonstrate the gene editing capabilities of cell VECT, we used our microfluidic device to deliver precomplexed CRISPR-Cas9 RNPs for permanent knockout of a target gene. We chose the Jurkat T-cell line as a surrogate for primary T-cells, which are the main cell type of interest for cell-based immunotherapies. We selected the T-cell receptor alpha chain (TRAC) locus as the gene editing site. The TRAC locus is a gene editing site of interest for both CAR T-cell and TCR therapies. Targeted insertion of the CAR gene at the TRAC locus has been shown to improve tumor rejection in CAR T therapies [31]. Techniques for knocking out the endogenous T-cell receptor gene are of interest for the developing fields of TCR therapies and allogeneic T-cell therapies. Permanent silencing of the endogenous TCR genes prevents unpredictable interactions with the exogenous TCR, and lack of endogenous TCR expression can also attenuate the graft-vs-host response [32-35].

To form the CRISPR-Cas9 RNP, the NLS-Cas9 nuclease (Aldevron) was precomplexed to a gRNA sequence (IDT) targeting the TRAC locus. The RNP was delivered to Jurkat cells using a 3.5 µm gap microfluidic device. We demonstrated successful knockout of the TRAC locus in Jurkat cells using analysis by TCR α/β antibody staining and flow cytometry (Figure 5.5A). Passing the cells through the microfluidic device multiple times only marginally improved editing efficiency (Figure 5.5A). Gene editing results were confirmed using Sanger sequencing (**Error! Reference source not f ound.**5B). Using a smaller microfluidic compression gap was shown to significantly increase the device gene editing efficiency (Figure 5.5C).
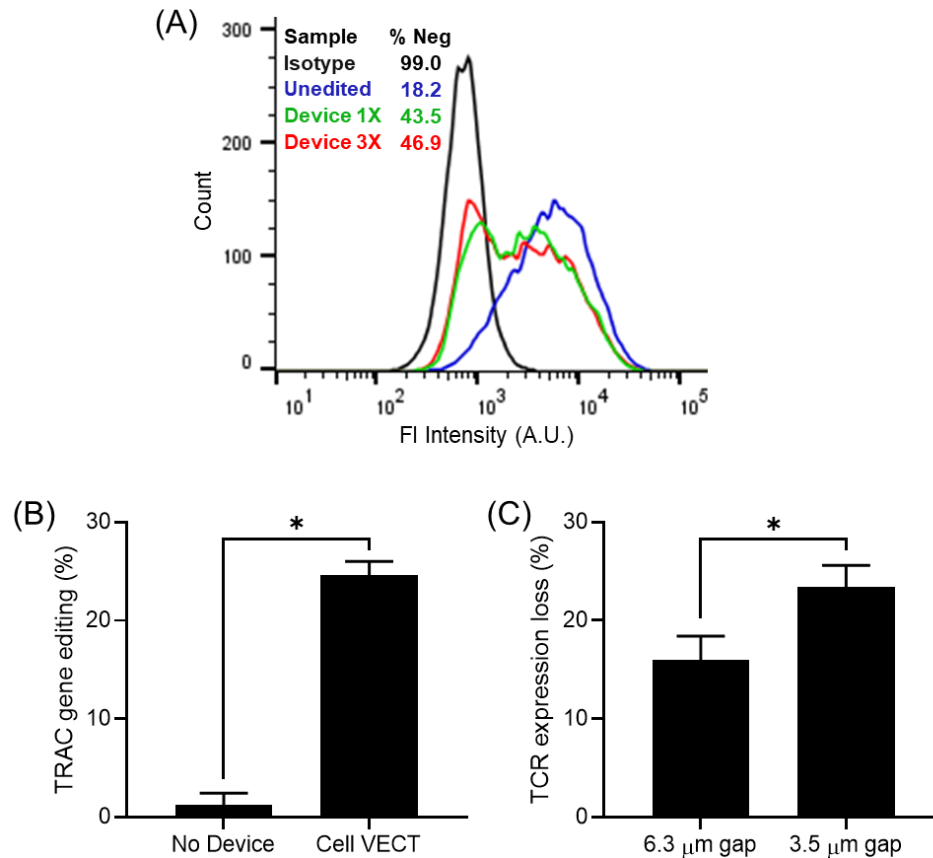
Figure 5.5: Gene editing of the TRAC locus by CRISPR-Cas9 RNP delivery. (A) Jurkat cells stained with TCR α/β antibody show significant loss of TCR expression in device-processed cells. Processing the cells through the device multiple times (3X) only marginally impacted TCR expression. (B) TRAC locus gene editing was confirmed using Sanger sequencing and indel analysis. No Device cells were exposed to the TRAC locus RNP but not processed by the device. N = 3, bars represent SD, *P<0.0001. (C) Processing cells using a smaller microfluidic compression gap resulted in increased loss of TCR expression, as determined by TCR α/β staining and flow cytometry. N = 3, bars represent SD, *P<0.05.

Furthermore, cell VECT processing is shown to have minimal impact on viability and proliferation, even at high rate and magnitude of compression. Cells experience <10% change in viability compared to No device controls, and proliferation continues par with No device controls for several days after processing, doubling approximately once per day.

In contrast, cells that undergo gene editing by electroporation show a significant decrease in cell viability and proliferation (Table 5.1).

Editing Method	Viability Day 5	5-Day Proliferation Fold-Change	Editing (%)	Edited Cell ROI
Electroporation	71.3 ± 12.5	3.2 ± 0.6	51.2 ± 2.1	1.6 ± 0.6
Cell VECT	98.4 ± 1.4	30.3 ± 3.7	26.0 ± 2.5	8.4 ± 0.4

Table 5.1: Table of cell VECT viability, proliferation, and editing vs electroporation. Electroporation has significantly lower viability and proliferation compared to cell VECT and untreated controls. In contrast, cell VECT samples maintain viability and proliferation comparable to untreated controls, doubling approximately once per day. Therefore, cell VECT has a higher edited cell ROI than electroporation despite having lower editing efficiency. Viability normalized to negative control. Mean ± SD, N = 3.

The combination of maintained viability and rapid proliferation enables cell VECT to produce a larger number of gene-edited cells than electroporation after a 5-day expansion period, despite electroporation producing a higher gene editing percentage. We can consider each gene editing technique as a system that takes a given input, a particular amount of CRISPR-Cas9 RNP and cells for processing, and produces gene-edited, viable cells as its output. The cell VECT system produces a higher return on input (ROI) for viable gene edited cells than electroporation due to higher cell viability and proliferation (Figure 5.6A,B). High viability and expansion are both important properties for cell therapy manufacturing, since engineered immunotherapy cells must usually be expanded to a therapeutic dose of at least 1 billion cells for an adult patient, and must maintain high cell viability to avoid adverse effects [36-38].
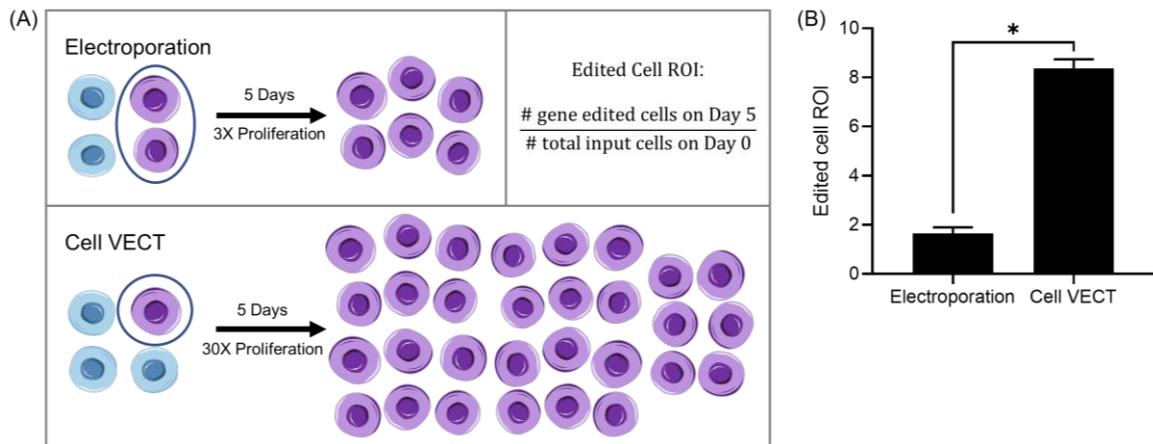
Figure 5.6: Cell VECT edited cell ROI compared to electroporation. (A) A schematic explanation of edited cell ROI. For a given number of input cells, the electroporation method produces a higher percentage of edited cells (purple). However the cell VECT population exhibits higher viability and proliferation over 5 days, resulting in a larger total population of edited cells. Note the post-proliferation population only shows gene edited cells, but the overall gene editing percentage remains the same as the pre-proliferation population. The total number of edited cells is a product of cell viability, proliferation, and gene editing efficiency. The edited cell ROI metric is the number of gene edited cells on Day 5 divided by the number of total input cells on Day 0. (B) Edited cell ROI of cell VECT exceeds electroporation due to higher viability and proliferation. N = 3, bars represent SD, *P<0.0001.

5.3.3 Multiplexed Endogenous Gene Editing

With the validation of cell VECT for permanent gene editing, we next sought to further apply this delivery platform for multiplexed gene editing. Multiplexed gene editing requires the delivery of multiple gene editing reagents to target different gene editing sites. Techniques for multiplexed gene editing are of great interest in many cell engineering use cases, particularly in cell therapies. Many cell therapies currently in preclinical and clinical development use multiple gene edits to target disease indications that cannot be effectively targeted by cell therapies that were created using a single gene edit. A powerful example

is in the treatment of T-cell acute lymphoblastic leukemia (T-ALL), which accounts for ~15% of all pediatric ALL and 25% of all adult ALL [33]. While certain T-cell surface markers, such as CD5 and CD3, can be used to target T-ALL using CARs, T-cell malignancies remain difficult to treat using single-edit CAR T-cell therapies due to the occurrence of T-on-T killing, or fratricide [33,39,40]. Therefore, a CAR T-cell that targets CD5 to treat T-cell malignancies must also undergo knockout of the endogenous CD5 gene to prevent fratricide.

Another invaluable application for multiplexed editing in cell therapies is motivated by the high demand for allogeneic cell therapies. The current dependence of clinical cell therapies on autologous cells poses a substantial cost, logistical, and manufacturing burden [41-43]. Furthermore, many patients are not able to provide usable T-cells for autologous treatment due to advanced disease state or chemotherapy effects, making them ineligible for life-saving cell therapies [43]. Knockout of endogenous TCR expression has been shown to enable the use of allogeneic T-cell therapies without provoking the graft-vs-host immune response [34]. Therefore, the implementation of multiplexed gene editing for cell therapy manufacturing facilitates a wide range of new cell therapy use cases and treatment targets.

In our experiments, we aimed to perform permanent gene knockout of the TRAC locus and the CD5 gene, a combination that would potentially enable the development of an allogeneic T-cell therapy that targets T-ALL. We used the cell VECT platform for simultaneous delivery of two species of CRISPR-Cas9 RNPs to target both editing sites in a single delivery. Flow cytometry analysis of antibody staining of TCR and CD5 showed successful knockout of both genes in ~10% of processed cells (Figure 5.7).
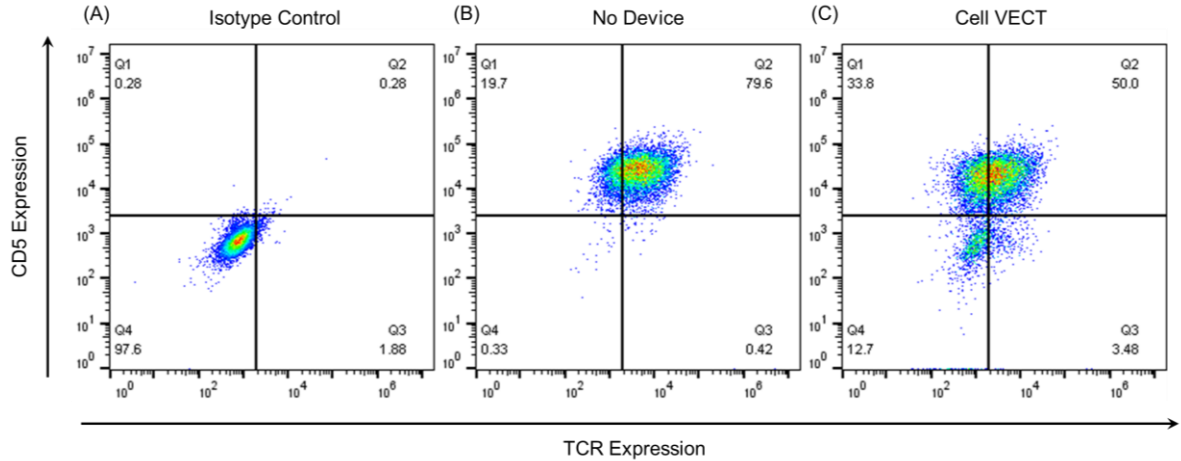
Figure 5.7: Multiplexed editing of CD5 and TRAC locus by CRISPR-Cas9 RNP delivery. (A) Jurkat cells stained with mouse IgG1 isotype controls to define double negative antibody stain gating. (B) No device control exposed to both CD5 and TRAC RNP without device processing and stained with CD5 and TCR α/β antibody. (C) Jurkat cells processed with cell VECT and both CD5 and TRAC RNP and stained with CD5 and TCR α/β antibody show a subpopulation of successful double knockout of CD5 and TCR expression in device-processed cells.

Editing Method	Viability Day 5	5-Day Proliferation Fold-Change	Double Editing (%)	Double-edited Cell ROI
Electroporation	75.3 ± 3.2	3.7 ± 1.2	44.4 ± 13.5	1.5 ± 1.2
Cell VECT	99.1 ± 2.1	33.7 ± 5.1	9.1 ± 1.0	3.1 ± 0.8

Table 5.2: Table of cell VECT double-editing, viability, and proliferation vs electroporation. As with single-editing, cell VECT maintains higher cell viability and proliferation than electroporation, resulting in a higher viable double-edited cell ROI than electroporation despite having lower double editing efficiency. Viability normalized to negative control. Mean ± SD, N = 3.

Similar to the single-knockout gene editing experiments, cells subjected to

multiplexed gene editing in the cell VECT device maintained high viability and

110

proliferation, whereas cells that underwent multiplexed gene editing by electroporation had

significantly lower viability and proliferation, but higher double-editing efficiency (Table

5.2). Overall, the viable double-edited cell ROI was higher in cell VECT cells than

electroporation due to higher proliferation and viability (Figure 5.8).
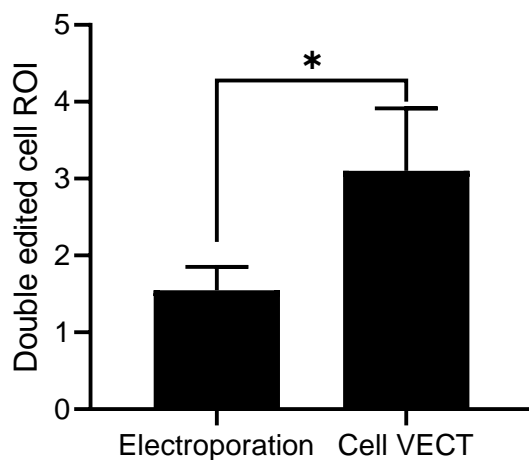
Figure 5.8: Cell VECT double-edited cell ROI compared to electroporation. ROI of multiplexed gene editing for cell VECT exceeds electroporation due to higher viability and proliferation. N = 3, bars represent SD, *P<0.05.

5.4   Summary of cell VECT applications for cell engineering

The rapidly growing field of cell manufacturing requires robust methods for

intracellular delivery of macromolecule reagents for cell engineering and analysis.

However, this field still lacks an intracellular delivery platform that is cost-effective,

maintains high cell viability, and is broadly applicable for diverse cargoes and cell types.

We utilize the unique biophysical phenomenon of mechanically-induced cell volume

exchange for convective intracellular delivery of large macromolecules. Successful results

in intracellular gene analysis, temporary transfection, and gene editing demonstrate great potential for cell VECT to address major challenges in cell manufacturing.

The ability of cell VECT to deliver large macromolecules facilitates the intracellular delivery of high molar mass reagents for transfection and gene editing. We have demonstrated proof-of-concept results using EGFP mRNA and plasmid for temporary transfection of cell lines and primary cells. We validate the use of cell VECT for gene editing by delivering CRISPR-Cas9 RNP complexes for permanent knockout of the TRAC locus. We further utilize the ability of cell VECT to deliver multiple cargoes by successfully demonstrating multiplexed gene editing of the TRAC locus and CD5 genes by simultaneously delivering two CRISPR-Cas9 RNP constructs.

Our transfection experiments also revealed some of the limitations faced by cell VECT in comparison to established electroporation techniques. We observed that electroporation achieved higher EGFP expression than cell VECT when delivering EGFP mRNA and plasmid. In our gene editing studies, we aimed to compensate for this factor by optimizing intracellular delivery with higher magnitude compressions and faster flow rates, which were facilitated by glass-reinforced devices. Gene editing efficiency using cell VECT was improved after optimization, but remained lower than electroporation for the same cell and reagent concentrations. These findings suggest that electroporation, or possibly the electrophoretic delivery driving mechanism, is able to achieve higher intracellular delivery concentration with less limitation due to extracellular reagent concentration.

Macromolecule delivery using cell VECT enables a number of useful applications for intracellular analysis. The nonendosomal delivery allows unencapsulated delivered molecules to interact directly with the cell interior, which enables the delivery of intracellular gene expression probes, like nano-flare mRNA probes, directly to the cytosol without the need to escape an endosome. The rapid nature of delivery while maintaining cell viability allows the nano-flares to directly bind target mRNA for a more immediate readout of gene expression in live cells, which is not possible with standard methods of intracellular analysis that require cell lysis or fixation

Overall, these results in a wide array of useful applications in intracellular gene expression analysis, temporary transfection, and permanent and multiplexed gene editing validate several highly valuable use cases for cell VECT in cell manufacturing and open the doors to many more applications.

5.5   Additional Applications

Further applications of interest have included using cell VECT for intracellular delivery of proteins for in-cell nuclear magnetic resonance (NMR) spectroscopy, and labeling stem cells for *in-vivo* therapeutic cell tracking. These applications have been explored through collaborations with laboratories at other institutions. In-cell NMR is being studied in collaboration with Alexander Shekhtman's lab at State University of New York at Albany. Stem cell labeling for *in-vivo* tracking is being studied in collaboration with Heike Daldrup-Link's lab at Stanford University.

In-cell NMR protein spectroscopy allows for the characterization of protein structure and interactions in the intracellular environment to help reveal protein signaling pathways [44,45]. However, in order to detect a target protein using in-cell NMR, the target signal must be distinguished from the background signal of other cell proteins, which requires the target protein concentration to exceed typical physiological levels [44,45]. Therefore, the field of in-cell protein NMR requires efficient methods for intracellular delivery of the target proteins. The delivery characteristics of cell VECT are advantageous for in-cell NMR applications. Since cell VECT delivers directly to the cell cytosol, the delivered protein does not face the additional impediment of escaping a primary endosome in order to reach its target interaction site.

We demonstrate the application of cell VECT for intracellular delivery of target proteins for in-cell NMR protein spectroscopy. For this study, we delivered dopamine- and cAMP-regulated neuronal phosphoprotein (DARPP-32) to HeLa cervical epithelial cells. DARPP-32 is a neuronal phosphoprotein that is part of the dopamine signaling pathway and has been shown to be decreased in the leukocytes and prefrontal cortex of the brain in patients with schizophrenia and bipolar disorder [46-49]. Therefore, a detailed study of the protein interactions and signaling cascade in the dopamine signaling pathway would grant a stronger understanding of dopamine signaling abnormalities and the associated psychiatric diseases. DARPP-32 delivered using cell VECT can then be analyzed by in-cell NMR and western blot to determine DARPP-32 presence and locations of modifications that impact protein function, such as phosphorylation (Figure S5. 1).

Labeling therapeutic stem cells for *in vivo* imaging allows for long term tracking of cell localization and regenerative progression. However, existing methods for intracellular

labeling require lengthy laboratory processing, which poses potential contamination risks [50] and can potentially impact stem cell physiology and potency [51-53]. Furthermore, because the labeling process usually takes several hours, it is impractical for stem cells to be harvested, labeled, and transplanted in a single surgery. We investigated the application of cell VECT as a method of rapid stem cell labeling to facilitate a single surgical procedure in which stem cells can be harvested, labeled with a contrast agent, and transplanted to track stem cell localization and engraftment without impacting treatment outcomes (Figure S5. 2A) [54].

Delivery of multiple contrast agents allows for cell tracking and detection using multiple imaging modalities: positron emission tomography (PET) and magnetic resonance imaging (MRI). For this study, we labeled and tracked adipose tissue-derived stem cells (ADSCs), which are used in regenerative medicine to treat degenerative joint diseases and cartilage defects. We used cell VECT to deliver ferumoxytol nanoparticles to the ADSCs for tracking using MRI (Figure S5. 2B) [54]. We simultaneously delivered a second tracer molecule, 18F-fluorodeoxyglucose (FDG), for cell tracking using PET (Figure S5. 2C) [54]. This multimodal labeling and imaging allows for quantification of ADSC delivery and engraftment in the disease site using PET, with long term cell tracking and observation using MRI. Delivery of both ferumoxytol and FDG labeling agents can be done using cell VECT in a single microfluidic delivery without additional processing steps.

5.6 Methods

5.6.1 Fabrication of Microfluidic Channels

The microfluidic features of this device were molded onto polydimethylsiloxane (PDMS) and plasma bonded to a glass slide. A reusable SU-8 mold was made using standard two-step photolithography on a silicon wafer. To fabricate the devices, a 10:1 ratio of PDMS and crosslinking agent was mixed and poured onto the SU-8 mold to form the microfluidic channel features by replica molding. For permanent gene editing devices, a glass slide was embedded into the PDMS. The PDMS was then degassed in a vacuum chamber and cured for 1 hr at 80°C. The cooled PDMS was then removed from the molds and outlets and inlets were punched using biopsy punches. The PDMS was then bonded to clean glass slides using a plasma bonder (PDC-32G Harrick) followed by 1 hr in a 80°C oven. After cooling, the channels were passivated using sterile filtered 1% bovine serum albumin (BSA) in DI water. For more detailed device fabrication protocols, please see Appendix A.1.

5.6.2 Microfluidic Experimental Setup

For SmartFlare RNA probe delivery experiments, cells were resuspended in serum-free RPMI-1640. For transfection and gene editing microfluidic experiments, cells were resuspended in Opti-MEM before flowing through the device. The cells were isolated from culture media and resuspended in buffer at ~$1\text{-}10 \times 10^6$ cells/mL with the desired concentration of target molecules. The cell-buffer suspension was infused into the microfluidic device at a controlled rate using syringe pumps (PHD 2000, Harvard

Apparatus). For delivery of constitutively fluorescent molecules, following collection from the outlets, the cells were washed 2X with 10-fold volume DPBS (-/-) to remove residual molecules external to the cells before analysis. Cells transfected with mRNA were analyzed at 12, 24, and 48 hour time points following transfection, with peak expression at 12 hours. Cells transfected with plasmid were analyzed at 24, 48, 72, and 96 hours following transfection, with peak expression at 24 hours. For experiments in which cells were cultured following microfluidics, the microfluidic experiment was conducted inside a sterile biosafety cabinet. All cell-handling supplies, including the device, syringe, and needles, were sterilized by autoclaving. For more detailed microfluidic experimental protocols, please see Appendix A.1.

5.6.3   Cell Culture

K562 cells from ATCC were cultured in RPMI-1640 supplemented with 10% fetal bovine serum (FBS) and 1% penicillin-streptomycin. PC3 prostate cancer cells (CRL-1435), a gift from BD Biosciences, were cultured in F-12K with 10% FBS and 1% penicillin-streptomycin and passaged using 0.25% Trypsin-EDTA. Deidentified and discarded blood sample was collected from Lam Lab, Georgia Institute of Technology, under an institutional review board (IRB) approved study for laboratory research on discarded clinical samples and all methods were performed in accordance with the relevant guidelines and regulations. Primary leukocytes were isolated from whole donor blood by density gradient centrifugation. Whole donor blood was centrifuged at 700 RCF for 10 mins with Ficoll density centrifugation media and the concentrated leukocyte band (buffy coat) was collected. Primary T-cells were isolated from healthy donor leukapheresis product using the EasySep Human T cell Enrichment Kit (Stem Cell Technologies)

according to manufacturer protocol. Primary T-cells were cultured in TexMACS medium (Miltenyi Biotec) with 100 IU/mL IL-2 (Miltenyi Biotec) and activated with T Cell TransAct (Miltenyi Biotec) CD3/CD28 nanoparticle T-cell activator at a 1:1 T-cell: nanoparticle ratio. Experiments took place 2 days after T-cell activation. Jurkat cells from ATCC were cultured in RPMI-1640 supplemented with 10% fetal bovine serum (FBS), 1% L-glutamine, and 1% penicillin-streptomycin. The cells were incubated at 37°C with 5% CO_2.

5.6.4   CRISPR-Cas9 RNP Gene Editing

The Cas9 nuclease was precomplexed to a gRNA sequence targeting the TRAC locus (IDT) to form the CRISPR-Cas9 RNP. We used the following CRISPR-Cas9 gRNA sequence for TRAC locus editing which has been previously published and validated: AGAGTCTCTCAGCTGGTACA [31]. To form the RNP, the Cas9 was mixed with a 2.5 molar excess of gRNA and incubated at room temperature for 30 mins. To promote localization of the RNP to the nuclease for gene editing, we used a Cas9 nuclease conjugated to a nuclear localization signal (NLS) (sNLS-SpCas9-sNLS Nuclease, Aldevron). Cells were processed using a microfluidic device with 3.5 μm compression gap and glass reinforcement in Opti-MEM with at 800 μL/min with 100 μg/mL NLS-Cas9 plus 2.5 molar excess gRNA. For multiplexed gene editing experiments, we precomplexed each species of RNP individually. For each multiplexed gene editing cell sample, we prepared 100 μg/mL NLS-Cas9 plus 2.5 molar excess gRNA for both TRAC and CD5, doubling the overall amount of CRISPR-Cas9 RNP. The two species of RNP were combined with cells immediately before processing with microfluidics or electroporation. Gene expression was

118

analyzed with flow cytometry after 5 days. Gene editing was analyzed by Sanger sequencing.

5.6.5 DNA Sequencing

Genomic DNA from the CRISPR-Cas9 gene editing experiments were isolated using QuickExtract DNA Extraction Solution (Lucigen) according to manufacturer protocol five days after delivery experiments. The genomic DNA was amplified using Phusion High-Fidelity PCR Master Mix (New England BioLabs) according to manufacturer protocol. The following primers were used to amplify the TRAC locus cut site: TGC CTG CCT TTA CTC TGC CA (forward) and AGG CCG AGA CCA ATC AG (reverse). Amplification was determined by gel electrophoresis. The PCR products were purified and then analyzed by Sanger sequencing (Eton Bioscience) and TIDE software was used for indel analysis.

5.6.6 Flow Cytometry

Flow cytometry was performed using the BD Accuri C6 Flow Cytometer and FlowJo analysis software. Cell uptake of cyanine-3 SmartFlare RNA probes was analyzed using 488 nm excitation and 585/40 filter. Expression of GFP RNA or plasmid was analyzed using 488 nm excitation and 533/30 filter. Cy5 delivery was analyzed using 640 nm excitation and 670 long pass filter. TCR expression was analyzed by staining with Alexa Fluor 488 anti-human TCR α/β antibody (488 nm excitation and 585/40 filter) (BioLegend) according to manufacturer protocol. 7-AAD (BioLegend) was used per manufacturer protocol to exclude nonviable cells (488 nm excitation and 670 long pass filter). CD5 expression was analyzed using PE anti-human CD5 antibody (488 nm

excitation and 585/40 filter) (BioLegend). Multiplex antibody staining was done using Helix NP NIR (BioLegend) viability stain exclusion and compensation to minimize fluorescent channel crosstalk.

5.6.7 Statistical Analysis

GraphPad Prism and Microsoft Excel were used to perform statistical analysis (ANOVA and t-test) and generate plots.

5.6.8 Electroporation

Electroporation of Primary T-cells was carried out using an Amaxa Nucleofector II and Lonza Human T Cell Nucleofector Kit using manufacturer protocols. T-cells were electroporated using Nucleofector Program T-023 in a 100 µL Amaxa cuvette. Jurkat cells were electroporated using Lonza Cell Line Nucleofector Kit V using manufacturer protocols. Jurkat cells were electroporated using Nucleofector Program X-001 in a 100 µL Amaxa cuvette.

5.7 References

[1]   Prigodich, A. E. *et al.* Nano-flares for mRNA regulation and detection. *ACS Nano.* **3**, 2147-2152, doi:10.1021/nn9003814 (2009).

[2]   Seferos, D. S., Giljohann, D. A., Hill, H. D., Prigodich, A. E. & Mirkin, C. A. Nano-flares: probes for transfection and mRNA detection in living cells. *J Am Chem Soc.* **129**, 15477-15479, doi:10.1021/ja0776529 (2007).

[3]   Stewart, M. P. *et al.* In vitro and ex vivo strategies for intracellular delivery. *Nature.* **538**, 183-192, doi:10.1038/nature19764 (2016).

[4]   Yin, H., Kauffman, K. J. & Anderson, D. G. Delivery technologies for genome editing. *Nature Reviews Drug Discovery.* **16**, 387-399, doi:10.1038/nrd.2016.280 (2017).

[5]   Gupta, S. K. & Shukla, P. Gene editing for cell engineering: trends and applications. *Critical Reviews in Biotechnology.* **37**, 672-684, doi:10.1080/07388551.2016.1214557 (2017).

[6]   Mali, P. & Cheng, L. Concise review: Human cell engineering: cellular reprogramming and genome editing. *Stem Cells.* **30**, 75-81, doi:10.1002/stem.735 (2012).

[7]   Osumi, N. & Inoue, T. Gene Transfer into Cultured Mammalian Embryos by Electroporation. *Methods.* **24**, 35-42, doi:http://dx.doi.org/10.1006/meth.2001.1154 (2001).

[8]   Glover, D. J., Lipps, H. J. & Jans, D. A. Towards safe, non-viral therapeutic gene expression in humans. *Nat. Rev. Genet.* **6**, 299-310 (2005).

[9]   Meacham, J. M., Durvasula, K., Degertekin, F. L. & Fedorov, A. G. Physical methods for intracellular delivery: practical aspects from laboratory use to industrial-scale processing. *J. Lab Autom.* **19**, 1-18, doi:10.1177/2211068213494388 (2014).

[10]   Kim, T. K. & Eberwine, J. H. Mammalian cell transfection: the present and the future. *Anal. Bioanal. Chem.* **397**, 3173-3178, doi:10.1007/s00216-010-3821-6 (2010).

[11]   Yang, S., Rosenberg, S. A. & Morgan, R. A. Clinical-scale lentiviral vector transduction of PBL for TCR gene therapy and potential for expression in less-differentiated cells. *J. Immunother.* **31**, 830-839, doi:10.1097/CJI.0b013e31818817c5 (2008).

[12]   Dodo, K. *et al.* An efficient large-scale retroviral transduction method involving preloading the vector into a RetroNectin-coated bag with low-temperature shaking. *PLoS One.* **9**, e86275, doi:10.1371/journal.pone.0086275 (2014).

[13]   Zhao, Y. *et al.* Multiple injections of electroporated autologous T cells expressing a chimeric antigen receptor mediate regression of human disseminated tumor. *Cancer Res.* **70**, 9053-9061, doi:10.1158/0008-5472.CAN-10-2880 (2010).

[14]   Wu, Z., Yang, H. & Colosi, P. Effect of genome size on AAV vector packaging. *Mol Ther.* **18**, 80-86, doi:10.1038/mt.2009.255 (2010).

[15]   Kumar, M., Keller, B., Makalou, N. & Sutton, R. E. Systematic determination of the packaging limit of lentiviral vectors. *Hum Gene Ther.* **12**, 1893-1905, doi:10.1089/104303401753153947 (2001).

[16] Rupp, L. J. *et al.* CRISPR/Cas9-mediated PD-1 disruption enhances anti-tumor efficacy of human chimeric antigen receptor T cells. *Sci. Rep.* **7**, 737, doi:10.1038/s41598-017-00462-8 (2017).

[17] Schultz, L. & Mackall, C. Driving CAR T cell translation forward. *Sci Transl Med.* **11**, doi:10.1126/scitranslmed.aaw2127 (2019).

[18] Boissel, L., Betancur, M., Wels, W. S., Tuncer, H. & Klingemann, H. Transfection with mRNA for CD19 specific chimeric antigen receptor restores NK cell mediated killing of CLL cells. *Leuk. Res.* **33**, 1255-1259, doi:10.1016/j.leukres.2008.11.024 (2009).

[19] Yarmush, M. L., Golberg, A., Sersa, G., Kotnik, T. & Miklavcic, D. Electroporation-Based Technologies for Medicine: Principles, Applications, and Challenges. *Annu. Rev. Biomed. Eng.* **16**, 295-320, doi:10.1146/annurev-bioeng-071813-104622 (2014).

[20] Liu, A. *et al.* Microfluidic generation of transient cell volume exchange for convectively driven intracellular delivery of large macromolecules. *Mater. Today.* **21**, 703-712, doi:10.1016/j.mattod.2018.03.002 (2018).

[21] Liu, A. *et al.* Cell Mechanical and Physiological Behavior in the Regime of Rapid Mechanical Compressions that Lead to Cell Volume Change. *Small.* e1903857, doi:10.1002/smll.201903857 (2019).

[22] Santangelo, P. J., Alonas, E., Jung, J., Lifland, A. W. & Zurla, C. Probes for intracellular RNA imaging in live cells. *Methods Enzymol.* **505**, 383-399, doi:10.1016/B978-0-12-388448-0.00028-0 (2012).

[23] Lahm, H. *et al.* Detection of Intracellular Gene Expression in Live Cells of Murine, Human and Porcine Origin Using Fluorescence-labeled Nanoparticles. *J. Visualized Exp.*, 53268, doi:10.3791/53268 (2015).

[24] Czarnek, M. & Bereta, J. SmartFlares fail to reflect their target transcripts levels. *Sci. Rep.* **7**, 11682, doi:10.1038/s41598-017-11067-6 (2017).

[25] Wu, X. A., Choi, C. H., Zhang, C., Hao, L. & Mirkin, C. A. Intracellular fate of spherical nucleic acid nanoparticle conjugates. *J Am Chem Soc.* **136**, 7726-7733, doi:10.1021/ja503010a (2014).

[26] Kizer, M. E. *et al.* Hydroporator: a hydrodynamic cell membrane perforator for high-throughput vector-free nanomaterial intracellular delivery and DNA origami biostability evaluation. *Lab Chip.* **19**, 1747-1754, doi:10.1039/c9lc00041k (2019).

[27] Gilboa, E. & Vieweg, J. Cancer immunotherapy with mRNA-transfected dendritic cells. *Immunol Rev.* **199**, 251-263, doi:10.1111/j.0105-2896.2004.00139.x (2004).

[28]   Bhaya, D., Davison, M. & Barrangou, R. CRISPR-Cas Systems in Bacteria and Archaea: Versatile Small RNAs for Adaptive Defense and Regulation. *Annual Review of Genetics.* **45**, 273-297, doi:10.1146/annurev-genet-110410-132430 (2011).

[29]   Terns, M. P. & Terns, R. M. CRISPR-based adaptive immune systems. *Current Opinion in Microbiology.* **14**, 321-327, doi:https://doi.org/10.1016/j.mib.2011.03.005 (2011).

[30]   Wiedenheft, B., Sternberg, S. H. & Doudna, J. A. RNA-guided genetic silencing systems in bacteria and archaea. *Nature.* **482**, 331-338, doi:10.1038/nature10886 (2012).

[31]   Eyquem, J. *et al.* Targeting a CAR to the TRAC locus with CRISPR/Cas9 enhances tumour rejection. *Nature.* **543**, 113-117, doi:10.1038/nature21405 (2017).

[32]   Roth, T. L. *et al.* Reprogramming human T cell function and specificity with non-viral genome targeting. *Nature.* **559**, 405-409, doi:10.1038/s41586-018-0326-5 (2018).

[33]   Rasaiyaah, J., Georgiadis, C., Preece, R., Mock, U. & Qasim, W. TCRalphabeta/CD3 disruption enables CD3-specific antileukemic T cell immunotherapy. *JCI Insight.* **3**, doi:10.1172/jci.insight.99442 (2018).

[34]   Poirot, L. *et al.* Multiplex Genome-Edited T-cell Manufacturing Platform for "Off-the-Shelf" Adoptive T-cell Immunotherapies. *Cancer Res.* **75**, 3853-3864, doi:10.1158/0008-5472.CAN-14-3321 (2015).

[35]   Stadtmauer, E. A. *et al.* CRISPR-engineered T cells in patients with refractory cancer. *Science.* doi:10.1126/science.aba7365 (2020).

[36]   Allan, D. S. *et al.* Number of viable CD34(+) cells reinfused predicts engraftment in autologous hematopoietic stem cell transplantation. *Bone Marrow Transplant.* **29**, 967-972, doi:10.1038/sj.bmt.1703575 (2002).

[37]   Lee, S. *et al.* Post-thaw viable CD34+ cell count is a valuable predictor of haematopoietic stem cell engraftment in autologous peripheral blood stem cell transplantation. *Vox Sanguinis.* **94**, 146-152, doi:10.1111/j.1423-0410.2007.01009.x (2008).

[38]   Yang, H. *et al.* Association of post-thaw viable CD34+ cells and CFU-GM with time to hematopoietic engraftment. *Bone Marrow Transplant.* **35**, 881-887, doi:10.1038/sj.bmt.1704926 (2005).

[39]   Moot, R. *et al.* Genetic engineering of chimeric antigen receptors using lamprey derived variable lymphocyte receptors. *Mol Ther Oncolytics.* **3**, 16026, doi:10.1038/mto.2016.26 (2016).

[40] Mamonkin, M., Rouce, R. H., Tashiro, H. & Brenner, M. K. A T-cell-directed chimeric antigen receptor for the selective treatment of T-cell malignancies. *Blood.* **126**, 983-992, doi:10.1182/blood-2015-02-629527 (2015).

[41] Abou-El-Enein, M., Bauer, G., Medcalf, N., Volk, H. D. & Reinke, P. Putting a price tag on novel autologous cellular therapies. *Cytotherapy.* **18**, 1056-1061, doi:10.1016/j.jcyt.2016.05.005 (2016).

[42] Wang, X. & Riviere, I. Clinical manufacturing of CAR T cells: foundation of a promising therapy. *Mol Ther Oncolytics.* **3**, 16015, doi:10.1038/mto.2016.15 (2016).

[43] MacLeod, D. T. *et al.* Integration of a CD19 CAR into the TCR Alpha Chain Locus Streamlines Production of Allogeneic Gene-Edited CAR T Cells. *Molecular Therapy.* **25**, 949-961, doi:https://doi.org/10.1016/j.ymthe.2017.02.005 (2017).

[44] Sciolino, N., Burz, D. S. & Shekhtman, A. In-Cell NMR Spectroscopy of Intrinsically Disordered Proteins. *PROTEOMICS.* **19**, 1800055, doi:10.1002/pmic.201800055 (2019).

[45] Breindel, L., Burz, D. S. & Shekhtman, A. Interaction proteomics by using in-cell NMR spectroscopy. *Journal of Proteomics.* **191**, 202-211, doi:https://doi.org/10.1016/j.jprot.2018.02.006 (2019).

[46] Sarah M. Clinton, Ph.D. , *et al.* Dopaminergic Abnormalities in Select Thalamic Nuclei in Schizophrenia: Involvement of the Intracellular Signal Integrating Proteins Calcyon and Spinophilin. *American Journal of Psychiatry.* **162**, 1859-1871, doi:10.1176/appi.ajp.162.10.1859 (2005).

[47] Albert, K. A. *et al.* Evidence for Decreased DARPP-32 in the Prefrontal Cortex of Patients With Schizophrenia. *Archives of General Psychiatry.* **59**, 705-712, doi:10.1001/archpsyc.59.8.705 (2002).

[48] Ishikawa, M., Mizukami, K., Iwakiri, M. & Asada, T. Immunohistochemical and immunoblot analysis of Dopamine and cyclic AMP-regulated phosphoprotein, relative molecular mass 32,000 (DARPP-32) in the prefrontal cortex of subjects with schizophrenia and bipolar disorder. *Progress in Neuro-Psychopharmacology and Biological Psychiatry.* **31**, 1177-1181, doi:https://doi.org/10.1016/j.pnpbp.2007.04.013 (2007).

[49] Torres, K. C. L. *et al.* The leukocytes expressing DARPP-32 are reduced in patients with schizophrenia and bipolar disorder. *Progress in Neuro-Psychopharmacology and Biological Psychiatry.* **33**, 214-219, doi:https://doi.org/10.1016/j.pnpbp.2008.10.020 (2009).

[50] FDA. Inspection of Human Cells, Tissues, and Cellular and Tissue-Based Products (HCT/Ps). (2012).

[51]   Kuroda, T., Yasuda, S. & Sato, Y. Tumorigenicity studies for human pluripotent stem cell-derived products. *Biol Pharm Bull.* **36**, 189-192 (2013).

[52]   Motaln, H., Schichor, C. & Lah, T. T. Human mesenchymal stem cells and their use in cell-based therapies. *Cancer.* **116**, 2519-2530, doi:10.1002/cncr.25056 (2010).

[53]   Soenen, S. J. & De Cuyper, M. Assessing cytotoxicity of (iron oxide-based) nanoparticles: an overview of different methods exemplified with cationic magnetoliposomes. *Contrast Media Mol Imaging.* **4**, 207-219, doi:10.1002/cmmi.282 (2009).

[54]   Nejadnik, H., Jung, K. O., Theruvath, A. J., Kiru, L., Liu, A., Wu, W., Sulchek, T., Pratx, G., Daldrup-Link, H. E. Instant labeling of therapeutic cells for multimodality imaging. *Theranostics.* doi:10.7150/thno.39554 (2020).

5.8   Supplemental Information
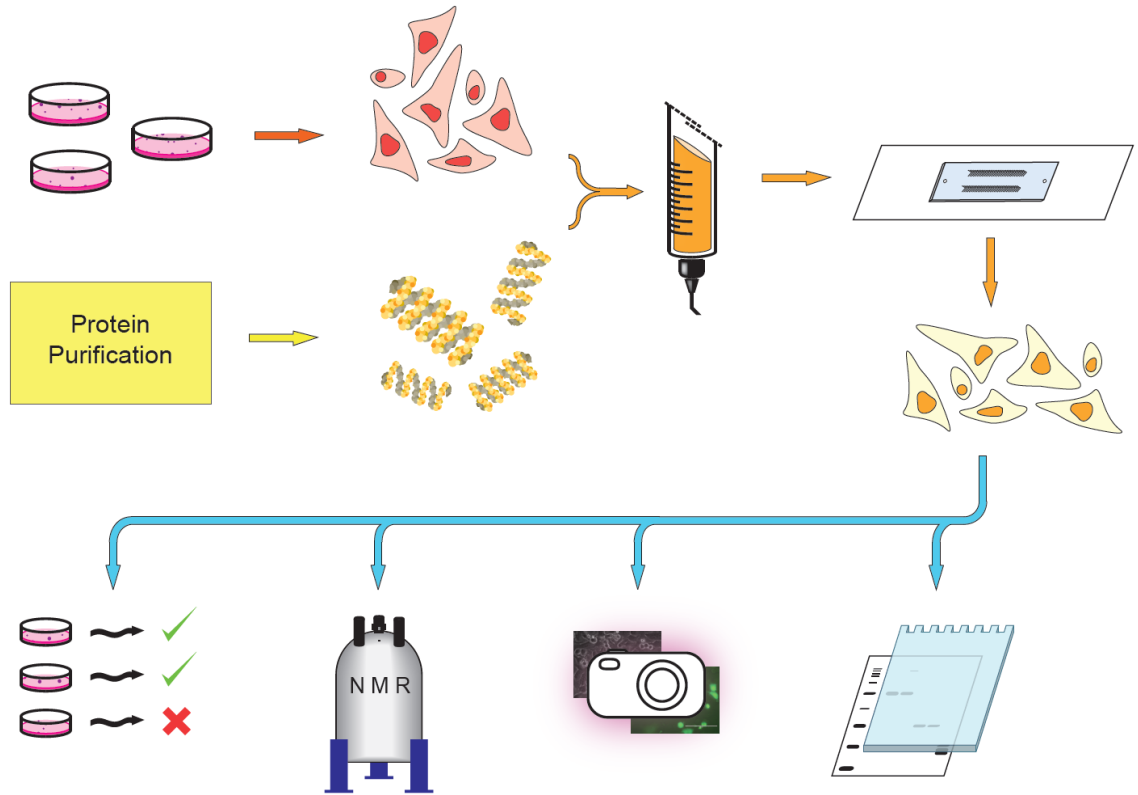
Figure S5. 1: Schematic of intracellular protein delivery and analysis. Suspended cells combined with purified protein are infused into the microfluidic device. The protein-loaded cells are then analyzed for viability (bottom left-most) and can then be characterized by (left to right) in-cell NMR, fluorescence microscopy, and western blot to determine protein signal and phosphorylation sites.
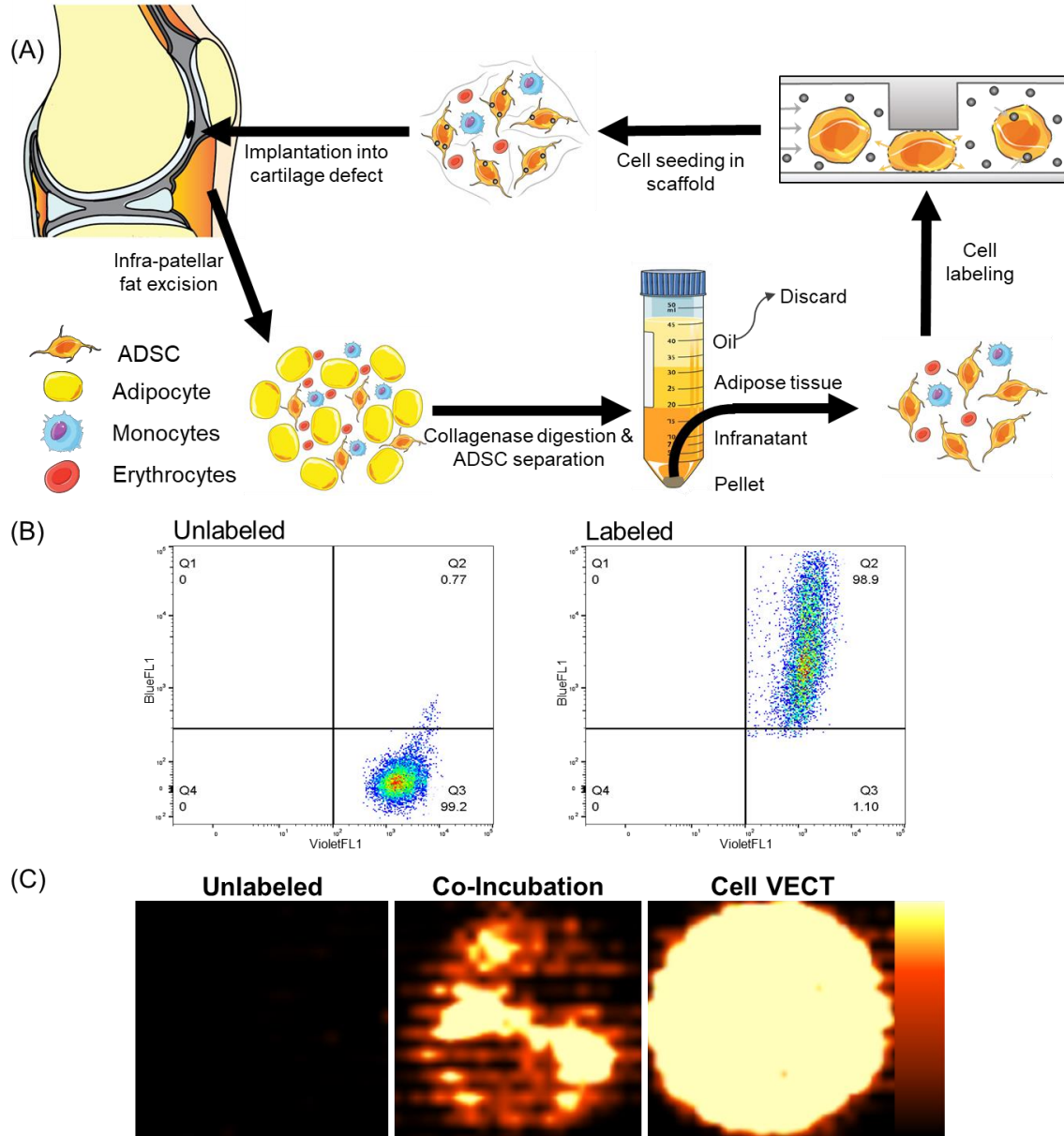
Figure S5. 2: Schematic and characterization of multimodal stem cell labeling. (A) A heterogeneous cell population containing ADSCs is harvested from the pre-patellar fat pad. ADSCs are concentrated and then undergo labeling with two different types of tracer molecules, ferumoxytol nanoparticles and FDG radiotracer, simultaneously by cell VECT before implantation into the cartilage defect. (B) Flow cytometry of ADSCs labeled with FITC-labeled ferumoxytol particles shows successful delivery to >95% of processed cells. (C) Delivery of FDG radiotracer to ADSCs using cell VECT is significantly higher than conventional co-incubation when characterized by *in vitro* PET imaging of plated cells. Cells were processed using microfluidic devices with a 9.6 μm compression gap, with 10 mg/mL ferumoxytol and 57 MBq/mL 18F-FDG.

CHAPTER 6.   CONCLUSIONS AND OUTLOOK

6.1   Summary of Major Findings

6.1.1   Aim 1: Characterizing governing parameters of cell VECT

By using microfluidics to precisely induce rapid, brief, large strain compressions, we elucidated the surprising phenomenon of temporary cell volume exchange that facilitates intracellular delivery of external macromolecules. We discovered a behavior wherein cells initially undergo sudden volume loss followed by fast volume recovery. We found that induced volume loss is greater for faster compressions caused by higher flow rates and larger strains imposed through smaller constrictions. We report the Ericksen number as a dimensionless parameterization of compression rate and cell viscoelastic properties that can predict the resulting cell volume loss. This relation may inform the implementation of cell VECT for a wide variety of human cell types. We also found that increased intracellular delivery required multiple ridges spaced such that there was sufficient time for cells to recover lost volume between each ridge. We used this effect of volume change and relaxation as a new approach to deliver molecules to cells. Specifically, rapid compression-driven volume loss worked in conjunction with cell relaxation to convectively drive volume and molecules into the cell interior.

The physical cause of this surprising cell behavior can be explained by considering the relevant forces imposed on the cell by the ridges. The sudden inertial compression under a ridge with stepwise profile is equivalent to a high velocity (~1 m/s) vertical impact on the cell to disrupt the membrane in a manner akin to a droplet splatter upon a surface.

The subsequent physical constriction of the cell under the ridge results in rapid transfer of momentum to the liquid of the cell interior to drive fluid volume out of the cell. The brief nature of this compression causes cells to relax on a rapid time scale to uptake volume after compression. The observed rapid recovery is consistent with rapid, poroelastic recovery behavior of the cytoplasm at short time scales (<0.5 s) after brief compression [1,2].

Overall, the phenomenon of cell VECT can be summarized into the following steps: (1) cell volume loss during rapid compression, (2) cell uptake of surrounding volume and target molecules during recovery, and (3) repetition of compressions for maximum intracellular delivery of target molecules. These steps are visualized and identified in Figure 6.1.
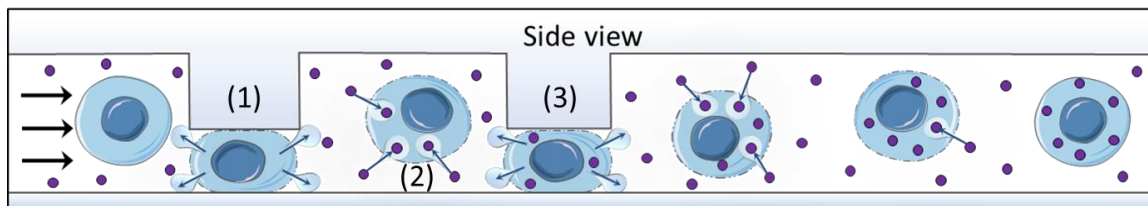
Figure 6.1: Visualized summary of the cell VECT process. The process of cell VECT can be broken down into the following steps: (1) cell volume loss during compression, (2) convective molecule uptake during volume recovery, and (3) repeated compressions for maximum delivery. The cell membrane will subsequently reseal and retain delivered cargo.

6.1.2 *Aim 2: Defining intracellular delivery capabilities and physiological effects on cells*

In this aim, we defined the characteristics and capabilities of intracellular macromolecule delivery using cell VECT. Cell VECT was shown to be distinct from

current diffusive mechanoporation platforms, both in mechanism and capability. Diffusive microfluidic mechanoporation methods used gradual constrictions to impart shear stress on cells in a manner that facilitates smooth cell flow and thus slower deformation [2-7]. The constriction creates a shear force on the cell membrane leading to membrane poration and extracellular molecular diffusion into the cell interior. While diffusion is a universal transport mechanism, it imposes constraints on delivery due to the inverse relationship between diffusivity and molecule size. Indeed, diffusive approaches to microfluidic mechanoporation have shown limited efficiency in the delivery of large macromolecules [8-13]. We characterized a convective intracellular delivery mechanism that is nonendosomal and independent of molecule size.

The purely mechanical, microfluidic approach avoids many of the prohibitive drawbacks and detrimental changes to cell physiology associated with using chemical, viral, or electrical processing [14-20]. This study finds that cell VECT causes minimal impact on nuclear envelop integrity and exchange of nuclear contents with the cytoplasm, which suggests that DNA damage does not occur. The ability of the cytoskeleton to regulate cell volume and retain solutes could explain the minimal impact of cell VECT on intracellular protein content despite the initial volume loss [21]. Long term cell viability and proliferation is also maintained, which supports the use of cell VECT in various useful applications in cell manufacturing.

6.1.3 Aim 3: Applications of cell VECT

In our studies, we found cell VECT utilizes an advection-dominated molecular driving mechanism to efficiently deliver a wide range of macromolecules to various types of human cells. The simplicity of use and successful proof of concept experiments in transfection and intracellular labeling demonstrate potential to overcome the most prohibitive challenges in intracellular delivery for cell engineering applications.

This work has validated cell VECT as a platform for intracellular labeling for cell analysis and tracking. Nonendosomal delivery of intracellular RNA probes enables real-time analysis of gene expression in living cells. Intracellular delivery of proteins facilitates NMR spectroscopy that elucidates intracellular protein modification and signaling pathways. Labeling of therapeutic stem cells with a combination of imaging contrast agents allows for multimodal imaging for long-term spaciotemporal tracking of therapy progression *in vivo*. Stem cell labeling for multimodal imaging can be done during the same surgery as the stem cell extraction and transplant.

The cell VECT platform can also be used to deliver reagents that modify cell gene expression, both temporarily and permanently. Delivery of non-integrating plasmid and mRNA demonstrated temporary expression of exogenous genes in cell lines and primary cells. Successful knockout of endogenous genes using CRISPR-Cas9 gene editing validated the application of cell VECT for permanent modification of gene expression. The results of cell VECT in cell labeling, analysis, and gene expression modification support the utility of this technology for useful applications in diagnostics and therapeutics.

6.2   Continuing Work

The contributions of this research have enabled a number of useful potential applications using cell VECT. As a continuation of this thesis work, multiple projects will further explore cell VECT in several applications of potential significance in research and clinical settings. The gene editing capability will be combined with viral transduction to prevent self-killing in CAR T-cells targeted at T-cell malignancies. A continuation of this research will investigate multiplexed gene editing in immunotherapeutic cells using cell VECT. Another project will explore the use of cell VECT for gene editing replacement of the endogenous TCR with an exogenous TCR. A continuing project will study gene editing of retinal progenitor cells by delivering very large plasmids using cell VECT.

6.2.1   Gene Knockout for CD5-targeting CAR T-cells

While CAR T-cell therapies have been proven to be highly effective in inducing remission in hematological cancers, the primary efficacy of CAR T-cell therapies has been in the treatment of B-cell malignancies [22-26]. The implementation of CAR T-cell therapies for the treatment of T-cell malignancies is complicated by the occurrence of self-killing, or fratricide, because a CAR construct targeted at T lymphoblasts will also direct cytotoxic activity against healthy T-cells and therapeutic CAR T-cells. T-cell acute lymphoblastic leukemia (T-ALL) accounts for ~20% of acute lymphoblastic leukemia and carries a poor prognosis, with a survival rate of <15% with conventional chemotherapy [27-30]. Only a minority of patients achieve remission and qualify for allogeneic hematopoietic stem cell transplantation (HSCT) [31], and even then the 3-year survival

rate after HSCT is ~50% [32]. Therefore, existing treatment methods for T-ALL would greatly benefit from the development of a viable CAR T-cell treatment option.

The CD5 surface marker is a relatively reliable surface marker for T-cell malignancies and has been shown to be an invaluable targeting gene against T-ALL [33-37]. However, CD5 is also expressed on healthy peripheral T-cells, thymocytes, and the B-1 subpopulation of B-cells. Preclinical studies of CD5-targeting CAR T-cells have shown cytotoxic activity directed against T-ALL cells, but also healthy cells and other therapeutic cells, and overall diminished efficacy. These findings suggest that T-ALL treatment using CD5-CAR T-cells requires knockout of the endogenous CD5 gene in the therapeutic cells to prevent fratricide and improve treatment efficacy [33,34].

An ongoing project in our lab combines non-viral CD5 knockout gene editing with viral expression of a CD5-CAR construct in primary T-cells. The T-cells are first processed with cell VECT to deliver a CRISPR Cas9 RNP construct for CD5 knockout. Processing with cell VECT enables permanent gene editing that maintains cell viability and proliferation for downstream processing with a lentiviral vector for transduction of the CD5-CAR gene. The therapeutic cells will be validated using *in vitro* cytotoxicity assays against T-ALL and in an *in vivo* T-cell leukemia xenograft mouse model. The sequential nonviral knockout and viral knock-in editing steps will result in a therapeutic CD5-targeting CAR T-cell population that is CD5-negative, preventing fratricide and improving treatment efficacy.

6.2.2 TCR Replacement via CRISPR Cas9

The development of non-viral, targeted gene editing techniques is a field of growing interest in the cell therapy space. The current standard method, viral transduction, suffers from high manufacture costs and persistent concerns over insertional mutagenesis due to the random nature of viral editing [15-18,38-40]. Furthermore, results have shown that targeting the insertion site of the CAR gene to the TRAC locus significantly improves the anti-tumor cytotoxic activity of CAR T-cells [41]. During the manufacture of TCR therapies, knockout of the endogenous TCR receptor genes is a necessary step to prevent the formation of unpredictable dimers between the exogenous TCR gene and the endogenous TCR [42]. Therefore, a continuing project in our lab seeks to utilize cell VECT for targeted knockout of the endogenous TRAC gene coupled with HDR-mediated knock-in of an exogenous TCR construct.

The overall goal of this project is to validate the application of cell VECT for targeted replacement of an endogenous gene with an exogenous therapeutic gene. Primary T-cells will be delivered with CRISPR-Cas9 RNP targeting the TRAC locus, along with a homology-directed repair (HDR) template encoding an exogenous TCR gene. This process should result in the knockout of the endogenous TRAC locus gene and insertion of the exogenous TCR gene at that site. While this project would specifically demonstrate applications for TCR therapy manufacturing, the results have strong implications for the use of cell VECT for any targeted gene replacement application, including the treatment of genetic disorders through the non-viral correction of faulty genes.

6.2.3 Multiplexed Gene Editing for Next Generation Cell Therapies

The next generation of cell-based immunotherapies require multiple gene edits to improve treatment safety and efficacy [30,43]. A major cause of disease relapse in cancer patients undergoing CAR T-cell therapy is a phenomenon called antigen escape, wherein a subpopulation of tumor cells that underexpress the targeted tumor antigen emerges, allowing the cancer to evade the CAR T therapy [44]. Therefore, next generation therapies aim to target multiple tumor antigens to prevent antigen escape. Furthermore, the overall trend of interest toward allogeneic, off-the-shelf cell therapies requires multiple gene edits to prevent graft-versus-host reactions. Specifically, inhibitory surface genes such as PD-1 are knocked out to ensure persistence of the therapeutic cells, while the endogenous TCR genes are knocked out to diminish graft-versus-host disease due to the allogeneic cells. Therefore, as new cell-based immunotherapies are developed, the demand for multiplexed gene editing techniques grows.

A continuing project in the Sulchek lab aims to utilize the ability of cell VECT to simultaneously deliver multiple cargoes in order to deliver multiple species of gene editing reagents for multiplexed gene editing. Primary T-cells will be processed with CRISPR Cas9 RNPs targeting PD-1 and both TCR genes (alpha and beta constant regions TRAC and TRBC). The ability to deliver multiple gene editing reagents without requiring additional processing steps allows this method to maintain high cell viability for downstream cell manufacturing processes.

6.2.4   Gene Engineering of Retinal Progenitor Cells using Large Plasmids

In addition to the cell immunotherapy projects previously described, we also aim to apply cell VECT to engineer stem cells for regenerative medicine. Gene engineering of stem cells is a promising strategy for treating permanent blindness caused by inherited degenerative retinal diseases. Since these inherited retinal diseases are usually caused by a single genetic defect, gene correction using CRISPR-Cas9 can potentially reverse disease effects and restore vision. The current standard strategy for correction of genetic defects in inherited retinal diseases is to use adeno-associated virus (AAV) to insert the functional gene into the genome of patient photoreceptor cells [45-48]. Implementing this gene correction process in patient-derived induced pluripotent stem cells (iPSCs) enables an autologous treatment option for patients who have already sustained significant loss of photoreceptor cells. However, almost 25% of inherited retinal diseases require the delivery of genes that are several times larger than the 5 kb packaging limit of AAVs [49]. An example of one such gene is USH2A, which has a coding length of approximately 15 kb. Mutations in the USH2A gene are associated with blindness as part of Usher syndrome.

Therefore, retinal therapeutics aimed at correcting blindness caused by USH2A defects would greatly benefit from an intracellular delivery method that can deliver very large genetic constructs. Preliminary experiments delivering large gene constructs (≥10 kb) show that cell VECT exceeds the transfection efficiency of lipofection, the current standard method for delivering plasmids that are too large for viruses to package. This ongoing project aims to optimize cell VECT delivery of large genetic constructs to produce gene corrected iPSCs. The focus will be on permanent correction of the USH2A gene by delivery of large plasmid constructs containing CRISPR-Cas9, the USH2A coding region, and an

antibiotic resistance selection gene. This project aims to utilize cell VECT's large cargo delivery capability to facilitate gene correction therapy in inherited diseases caused by defects in large genes.

6.3 Conclusions

In this thesis, we characterized the cell biomechanical phenomenon wherein rapid, high strain compressions cause cell volume loss and recovery. We found that this cell volume exchange caused extracellular molecules to be driven into the cell interior by convection. We refer to this process as cell VECT, cell volume exchange for convective transfer. We have determined the device and experiment parameters that govern cell VECT and provide basic understanding to mechanically induced cell volume exchange. We use these findings to inform the optimization of the microfluidic device design to improve intracellular delivery and throughput. We show convection to be a powerful driving mechanism for intracellular delivery of large macromolecules (>2 MDa), especially in comparison to diffusion alone. We also determine that cell VECT has minimal impact on nuclear envelop integrity, protein loss, and long term cell viability and proliferation. Cell VECT enables new applications for microfluidic molecular delivery, including high-throughput delivery of large macromolecules and particles for cell labeling, analysis, transfection, and gene editing. This work has elucidated a new cell phenomenon with great potential to serve as a nearly universal intracellular delivery platform for a variety of valuable clinical and research applications in biotechnology.

6.4 References

[1] Moeendarbary, E. *et al.* The cytoplasm of living cells behaves as a poroelastic material. *Nat. Mater.* **12**, 253-261, doi:http://www.nature.com/nmat/journal/v12/n3/abs/nmat3517.html#supplementary-information (2013).

[2] Tran-Son-Tay, R., Needham, D., Yeung, A. & Hochmuth, R. M. Time-dependent recovery of passive neutrophils after large deformation. *Biophys. J.* **60**, 856-866, doi:10.1016/S0006-3495(91)82119-1 (1991).

[3] Mokbel, M. *et al.* Numerical Simulation of Real-Time Deformability Cytometry To Extract Cell Mechanical Properties. *ACS Biomater. Sci. Eng.*, doi:10.1021/acsbiomaterials.6b00558 (2017).

[4] Guo, Q., Park, S. & Ma, H. Microfluidic micropipette aspiration for measuring the deformability of single cells. *Lab Chip.* **12**, 2687-2695, doi:10.1039/c2lc40205j (2012).

[5] Needham, D. & Hochmuth, R. M. Rapid flow of passive neutrophils into a 4 microns pipet and measurement of cytoplasmic viscosity. *J. Biomech. Eng.* **112**, 269-276 (1990).

[6] Zheng, Y., Nguyen, J., Wei, Y. & Sun, Y. Recent advances in microfluidic techniques for single-cell biophysical characterization. *Lab Chip.* **13**, 2464-2483, doi:10.1039/c3lc50355k (2013).

[7] Gabriele, S., Benoliel, A.-M., Bongrand, P. & Théodoly, O. Microfluidic Investigation Reveals Distinct Roles for Actin Cytoskeleton and Myosin II Activity in Capillary Leukocyte Trafficking. *Biophys. J.* **96**, 4308-4318, doi:http://dx.doi.org/10.1016/j.bpj.2009.02.037 (2009).

[8] Sharei, A. *et al.* Ex vivo cytosolic delivery of functional macromolecules to immune cells. *PLoS One.* **10**, e0118803, doi:10.1371/journal.pone.0118803 (2015).

[9] Szeto, G. L. *et al.* Microfluidic squeezing for intracellular antigen loading in polyclonal B-cells as cellular vaccines. *Sci. Rep.* **5**, 10276, doi:10.1038/srep10276 (2015).

[10] Sharei, A. *et al.* Plasma membrane recovery kinetics of a microfluidic intracellular delivery platform. *Integr. Biol.* **6**, 470-475, doi:10.1039/c3ib40215k (2014).

[11] Ding, X. *et al.* High-throughput nuclear delivery and rapid expression of DNA via mechanical and electrical cell-membrane disruption. *Nat. Biomed. Eng.* **1**, 0039, doi:10.1038/s41551-017-0039 http://www.nature.com/articles/s41551-017-0039#supplementary-information (2017).

[12]   Saung, M. T. *et al.* A Size-Selective Intracellular Delivery Platform. *Small.* doi:10.1002/smll.201601155 (2016).

[13]   Hallow, D. M. *et al.* Shear-induced intracellular loading of cells with molecules by controlled microfluidics. *Biotechnol. Bioeng.* **99**, 846-854, doi:10.1002/bit.21651 (2008).

[14]   Zorko, M. & Langel, Ü. Cell-penetrating peptides: mechanism and kinetics of cargo delivery. *Adv. Drug Delivery Rev.* **57**, 529-545, doi:http://dx.doi.org/10.1016/j.addr.2004.10.010 (2005).

[15]   Osumi, N. & Inoue, T. Gene Transfer into Cultured Mammalian Embryos by Electroporation. *Methods.* **24**, 35-42, doi:http://dx.doi.org/10.1006/meth.2001.1154 (2001).

[16]   Kim, T. K. & Eberwine, J. H. Mammalian cell transfection: the present and the future. *Anal. Bioanal. Chem.* **397**, 3173-3178, doi:10.1007/s00216-010-3821-6 (2010).

[17]   Meacham, J. M., Durvasula, K., Degertekin, F. L. & Fedorov, A. G. Physical methods for intracellular delivery: practical aspects from laboratory use to industrial-scale processing. *J. Lab Autom.* **19**, 1-18, doi:10.1177/2211068213494388 (2014).

[18]   Glover, D. J., Lipps, H. J. & Jans, D. A. Towards safe, non-viral therapeutic gene expression in humans. *Nat. Rev. Genet.* **6**, 299-310 (2005).

[19]   Joliot, A. & Prochiantz, A. Transduction peptides: from technology to physiology. *Nat. Cell Biol.* **6**, 189-196 (2004).

[20]   Boissel, L., Betancur, M., Wels, W. S., Tuncer, H. & Klingemann, H. Transfection with mRNA for CD19 specific chimeric antigen receptor restores NK cell mediated killing of CLL cells. *Leuk. Res.* **33**, 1255-1259, doi:10.1016/j.leukres.2008.11.024 (2009).

[21]   Sachs, F. & Sivaselvan, M. V. Cell volume control in three dimensions: Water movement without solute movement. *J. Gen. Physiol.* **145**, 373-380, doi:10.1085/jgp.201411297 (2015).

[22]   Maude, S. L. *et al.* Chimeric antigen receptor T cells for sustained remissions in leukemia. *N Engl J Med.* **371**, 1507-1517, doi:10.1056/NEJMoa1407222 (2014).

[23]   Davila, M. L. *et al.* Efficacy and toxicity management of 19-28z CAR T cell therapy in B cell acute lymphoblastic leukemia. *Sci Transl Med.* **6**, 224ra225, doi:10.1126/scitranslmed.3008226 (2014).

[24]   Lee, D. W. *et al.* T cells expressing CD19 chimeric antigen receptors for acute lymphoblastic leukaemia in children and young adults: a phase 1 dose-escalation trial. *Lancet.* **385**, 517-528, doi:10.1016/S0140-6736(14)61403-3 (2015).

[25]   Schubert, M. L. *et al.* Chimeric Antigen Receptor T Cell Therapy Targeting CD19-Positive Leukemia and Lymphoma in the Context of Stem Cell Transplantation. *Hum Gene Ther.* doi:10.1089/hum.2016.097 (2016).

[26]   Lim, W. A. & June, C. H. The Principles of Engineering Immune Cells to Treat Cancer. *Cell.* **168**, 724-740, doi:10.1016/j.cell.2017.01.016 (2017).

[27]   Henze, G. *et al.* Six-year experience with a comprehensive approach to the treatment of recurrent childhood acute lymphoblastic leukemia (ALL-REZ BFM 85). A relapse study of the BFM group. *Blood.* **78**, 1166-1172 (1991).

[28]   Einsiedel, H. G. *et al.* Long-term outcome in children with relapsed ALL by risk-stratified salvage therapy: results of trial acute lymphoblastic leukemia-relapse study of the Berlin-Frankfurt-Munster Group 87. *J Clin Oncol.* **23**, 7942-7950, doi:10.1200/JCO.2005.01.1031 (2005).

[29]   Reismuller, B. *et al.* Outcome of children and adolescents with a second or third relapse of acute lymphoblastic leukemia (ALL): a population-based analysis of the Austrian ALL-BFM (Berlin-Frankfurt-Munster) study group. *J Pediatr Hematol Oncol.* **35**, e200-204, doi:10.1097/MPH.0b013e318290c3d6 (2013).

[30]   Rasaiyaah, J., Georgiadis, C., Preece, R., Mock, U. & Qasim, W. TCRalphabeta/CD3 disruption enables CD3-specific antileukemic T cell immunotherapy. *JCI Insight.* **3**, doi:10.1172/jci.insight.99442 (2018).

[31]   Raetz, E. A. *et al.* Reinduction platform for children with first marrow relapse of acute lymphoblastic Leukemia: A Children's Oncology Group Study[corrected]. *J Clin Oncol.* **26**, 3971-3978, doi:10.1200/JCO.2008.16.1414 (2008).

[32]   Burke, M. J. *et al.* Transplant Outcomes for Children with T Cell Acute Lymphoblastic Leukemia in Second Remission: A Report from the Center for International Blood and Marrow Transplant Research. *Biol Blood Marrow Transplant.* **21**, 2154-2159, doi:10.1016/j.bbmt.2015.08.023 (2015).

[33]   Mamonkin, M., Rouce, R. H., Tashiro, H. & Brenner, M. K. A T-cell-directed chimeric antigen receptor for the selective treatment of T-cell malignancies. *Blood.* **126**, 983-992, doi:10.1182/blood-2015-02-629527 (2015).

[34]   Moot, R. *et al.* Genetic engineering of chimeric antigen receptors using lamprey derived variable lymphocyte receptors. *Mol Ther Oncolytics.* **3**, 16026, doi:10.1038/mto.2016.26 (2016).

[35]   Raikar, S. S. *et al.* Development of chimeric antigen receptors targeting T-cell malignancies using two structurally different anti-CD5 antigen binding domains in

NK and CRISPR-edited T cell lines. *OncoImmunology.* 00-00, doi:10.1080/2162402X.2017.1407898 (2017).

[36]   Chen, K. H. *et al.* Preclinical targeting of aggressive T-cell malignancies using anti-CD5 chimeric antigen receptor. *Leukemia.* **31**, 2151-2160, doi:10.1038/leu.2017.8 (2017).

[37]   Mamonkin, M. *et al.* Reversible Transgene Expression Reduces Fratricide and Permits 4-1BB Costimulation of CAR T Cells Directed to T-Cell Malignancies. *Cancer Immunol Res.* doi:10.1158/2326-6066.CIR-17-0126 (2017).

[38]   Yang, S., Rosenberg, S. A. & Morgan, R. A. Clinical-scale lentiviral vector transduction of PBL for TCR gene therapy and potential for expression in less-differentiated cells. *J. Immunother.* **31**, 830-839, doi:10.1097/CJI.0b013e31818817c5 (2008).

[39]   Dodo, K. *et al.* An efficient large-scale retroviral transduction method involving preloading the vector into a RetroNectin-coated bag with low-temperature shaking. *PLoS One.* **9**, e86275, doi:10.1371/journal.pone.0086275 (2014).

[40]   Zhao, Y. *et al.* Multiple injections of electroporated autologous T cells expressing a chimeric antigen receptor mediate regression of human disseminated tumor. *Cancer Res.* **70**, 9053-9061, doi:10.1158/0008-5472.CAN-10-2880 (2010).

[41]   Eyquem, J. *et al.* Targeting a CAR to the TRAC locus with CRISPR/Cas9 enhances tumour rejection. *Nature.* **543**, 113-117, doi:10.1038/nature21405 (2017).

[42]   Roth, T. L. *et al.* Reprogramming human T cell function and specificity with non-viral genome targeting. *Nature.* **559**, 405-409, doi:10.1038/s41586-018-0326-5 (2018).

[43]   Rupp, L. J. *et al.* CRISPR/Cas9-mediated PD-1 disruption enhances anti-tumor efficacy of human chimeric antigen receptor T cells. *Sci. Rep.* **7**, 737, doi:10.1038/s41598-017-00462-8 (2017).

[44]   Schultz, L. & Mackall, C. Driving CAR T cell translation forward. *Sci Transl Med.* **11**, doi:10.1126/scitranslmed.aaw2127 (2019).

[45]   Bainbridge, J. W. *et al.* Long-term effect of gene therapy on Leber's congenital amaurosis. *N Engl J Med.* **372**, 1887-1897, doi:10.1056/NEJMoa1414221 (2015).

[46]   Jacobson, S. G. *et al.* Gene therapy for leber congenital amaurosis caused by RPE65 mutations: safety and efficacy in 15 children and adults followed up to 3 years. *Arch Ophthalmol.* **130**, 9-24, doi:10.1001/archophthalmol.2011.298 (2012).

[47]   Russell, S. *et al.* Efficacy and safety of voretigene neparvovec (AAV2-hRPE65v2) in patients with RPE65-mediated inherited retinal dystrophy: a randomised,

controlled, open-label, phase 3 trial. *Lancet.* **390**, 849-860, doi:10.1016/S0140-6736(17)31868-8 (2017).

[48]   Testa, F. *et al.* Three-year follow-up after unilateral subretinal delivery of adeno-associated virus in patients with Leber congenital Amaurosis type 2. *Ophthalmology.* **120**, 1283-1291, doi:10.1016/j.ophtha.2012.11.048 (2013).

[49]   Stone, E. M. *et al.* Clinically Focused Molecular Investigation of 1000 Consecutive Families with Inherited Retinal Disease. *Ophthalmology.* **124**, 1314-1331, doi:10.1016/j.ophtha.2017.04.008 (2017).

APPENDIX A.

A.1 Protocols

A.1.1 Cell VECT Device Fabrication Protocol

Overview of Steps:

1. PDMS molding

2. Cleaning PDMS and glass slide

3. Bonding PDMS to glass slide

PDMS Molding

1. Thoroughly mix polydimethylsiloxane (PDMS) with crosslinker in 10:1 PDMS:crosslinker ratio.

2. Check silicon wafer mold for cleanliness.

   a. Clean with air gun for dust.

   b. Clean with IPA and DI water for smudges. Thoroughly dry the mold before use.

3. Place silicon wafer mold in baking dish, pour mixed PDMS and crosslinker on top.

4. Degas the PDMS in vacuum desiccator until all bubbles are removed.

5. Use enough PDMS such that the PDMS layer is at least ~5 mm thick over the surface of the wafer.

6. Bake PDMS in oven at 80°C for 1 hr.

7. After cooling, carefully release the PDMS from the wafer.

    a. Cut/pull the PDMS away from the edges of the baking dish.

    b. Gently remove the PDMS and wafer from the baking dish by lifting the PDMS equally from all sides.

        i. Use careful, gradual motions, as this is a step at which the wafer is more likely to break.

    c. Remove PDMS film from the back of the wafer.

    d. Gradually lift PDMS around the edge of the wafer until wafer is fully released.

        i. Peel PDMS off the entire perimeter, then gradually release the PDMS from the wafer equally around the perimeter, working your way in. Again, use careful, gradual motions, as this is a step at which the wafer is more likely to break.

Cleaning PDMS and Glass Slide

1. Cut devices out of PDMS.

    a. Cut in straight rectangles.

2. Punch holes at inlets and outlets using biopsy punches.

    a. Always keep PDMS pattern side up

    b. Place a soft surface underneath the PDMS to prevent dulling the biopsy punch. A spare slab of cured PDMS is suitable, or something similar.

    c. Hold biopsy punch from the back, push straight down, perpendicular to the PDMS surface, punch, pull straight out, do not twist.

d. Use 1 mm biopsy punch for inlets and outlets. This corresponds to a 18 gauge needle.

e. Observe that punches are clean and cylindrical. If punches are jagged, use a new punch.

3. Cover the PDMS devices, both sides, with Scotch tape, apply even pressure with thumb to remove dust. Keep taped until ready to bond.

a. Clean glass slides by taping with Scotch tape.

4. Check the quality of the devices before bonding.

a. Don't touch pattern, keep pattern side up at all times.

b. Move devices to Petri dish with pattern side up.

c. Observe all devices under microscope at 5x magnification, make sure entire pattern is free of dust, channels and ridges are intact, properly formed, and undamaged, then tape off the pattern surface until ready to bond.

Bonding PDMS to Glass Slide

1. Turn on Harrick Plasma Cleaner and leave on until after bonding process is complete, leave pump and RF knob off until ready to bond.

2. Put PDMS & glass slide face up on plasma bonder sample tray.

3. Plasma cleaner door knob: $\downarrow$ = closed, $\rightarrow$ = open, $\leftarrow$ = valve-controlled.

4. Turn valve 45 degrees from closed, leave at that setting.

5. Place plasma bonder sample tray with glass slide and PDMS into plasma bonder.

a. Set knob to closed ($\downarrow$ = closed).

b. Vacuum out the plasma chamber for 1 minute.

6. Turn RF to high, turn knob to valve-controlled ($\leftarrow$ = valve-controlled).

   a. Plasma should form immediately.

   b. Plasma color should be bright pink/purple.

   c. Blue plasma indicates not enough oxygen. Ensure that the valve is 45 degrees from closed to allow a small amount of oxygen into the channel.

   d. Dark purple plasma indicates insufficient vacuum. Ensure the valve is not too far open (more than 45 degrees from closed), or that the door is properly closed, and the doorknob is turned to valve-controlled ($\leftarrow$ = valve-controlled).

7. Immediately after 1 min plasma bonding:

   a. Turn RF off.

   b. Turn pump off.

   c. SLOWLY rotate knob to open ($\rightarrow$ = open). Repressurizing the chamber too quickly can cause samples to move around. Wait until hissing air stops before opening the door and removing the sample tray.

8. Immediately place PDMS, pattern side down, on glass slide, gently tap edges and sides of channel with tweezers to form fully bonded surface, no bubbles.

   a. Do not tap on top of the channels, can cause channels or ridges to bond to the glass slide.

9. Label slides with your initials, device specs, and date, transfer to 60-80°C oven for 1-2 hours.

10. Remove devices from oven and let cool to room temperature. A representative image of a properly bonded device is shown in Figure A. 1.

11. Observe all devices under microscope at 5x magnification, make sure entire pattern is free of dust and channels are properly bonded.

12. Store devices in closed containers, away from dust and contaminants.
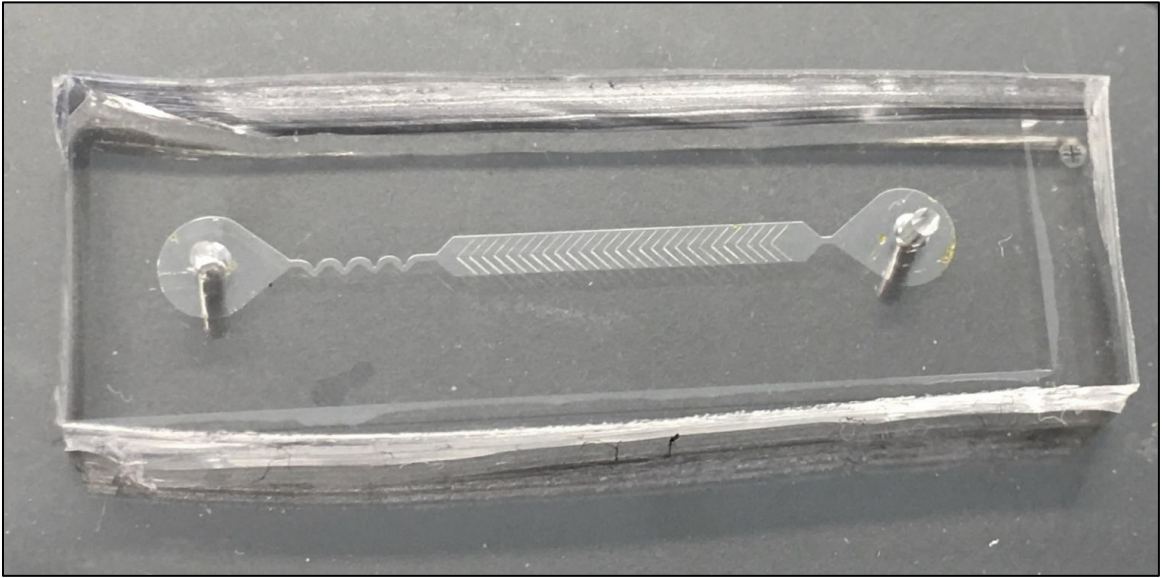
Figure A. 1: Bonded PDMS device. Example image of a PDMS device made with the standard device fabrication protocol. The device is PDMS throughout, bonded to a glass slide. A correctly bonded device will have fine channel features that are clearly defined and visible to the naked eye.

A.1.2   Cell VECT Glass-Reinforced Device Fabrication Protocol

Overview of Steps:

1. Apply thin PDMS layer to silicon mold

2. Place glass slides on thin PDMS layer

3. Pour and cure thick PDMS layer on top

Apply Thin PDMS Layer:

1. Thoroughly mix PDMS with crosslinker at 10:1 PDMS:crosslinker ratio.

2. Degas 10:1 PDMS in a vacuum desiccator.

8. Check silicon wafer mold for cleanliness.

 c. Clean with air gun for dust.

 d. Clean with IPA and DI water for smudges. Thoroughly dry the mold before use.

3. For a 100 mm diameter wafer mold, apply 4 mL 10:1 PDMS to the surface for a PDMS layer ~ 0.5 mm thick, tilt to coat the entire wafer surface evenly.

4. Cure the thin 10:1 PDMS layer in 80$^\text{o}$C oven until fully cured (~5-10 mins).

 a. Check that the thin PDMS layer is cured by gently tapping the layer over an empty part of the wafer with a pipet tip.

Place Glass Slides on Thin PDMS Layer:

1. Use a glass cutter to cut standard, 1 mm thick microscope slides.

 a. Fit the slide dimensions to fully cover the microfluidic channel, but not the inlets and outlets, approximately 4 mm by 10 mm.

b. Clean the cut glass with Scotch tape to remove glass fragments.

2. Coat one side of each glass slide with a very thin layer of uncured 10:1 PDMS.

3. Carefully place the glass slide PDMS-side down onto the cured thin PDMS layer on the wafer.

   a. Gently press on the slide to remove air bubbles.

   b. Make sure the glass slide does not cover the inlet or outlet regions.

4. Bake in 80°C oven until the glass slides are cured into place (~5-10 mins).

   a. Ensure the glass slides are cured into place by gently pushing the glass slides with a pipet tip.

   b. This prevents the glass slides from drifting out of place when the thick PDMS layer is poured on top.

Pour and Cure Thick PDMS Layer:

1. Pour 40 mL of premixed and degassed 10:1 PDMS on top of the cured thin PDMS layer and glass slides.

   a. Wafer should be in a container that is approximately the same size and shape as the wafer.

   b. Use a sufficient amount of 10:1 PDMS for this thick PDMS layer such that the overall PDMS layer is at least ~5 mm thick over the surface of the wafer.

   c. Fully degas the PDMS in a vacuum desiccator if necessary.

2. Cure in 80°C oven for 1 hour.

3. Allow to cool before gently releasing the PDMS from the wafer.

   a. Release the PDMS very slowly, taking extra care not to rip the thin PDMS layer off of the embedded glass slides.

4. Once released, tape the PDMS device features to prevent dust contamination.

5. Proceed to standard cleaning and bonding procedures described in Section A.1.1.

6. A complete glass-reinforced device should look like Figure A. 2.
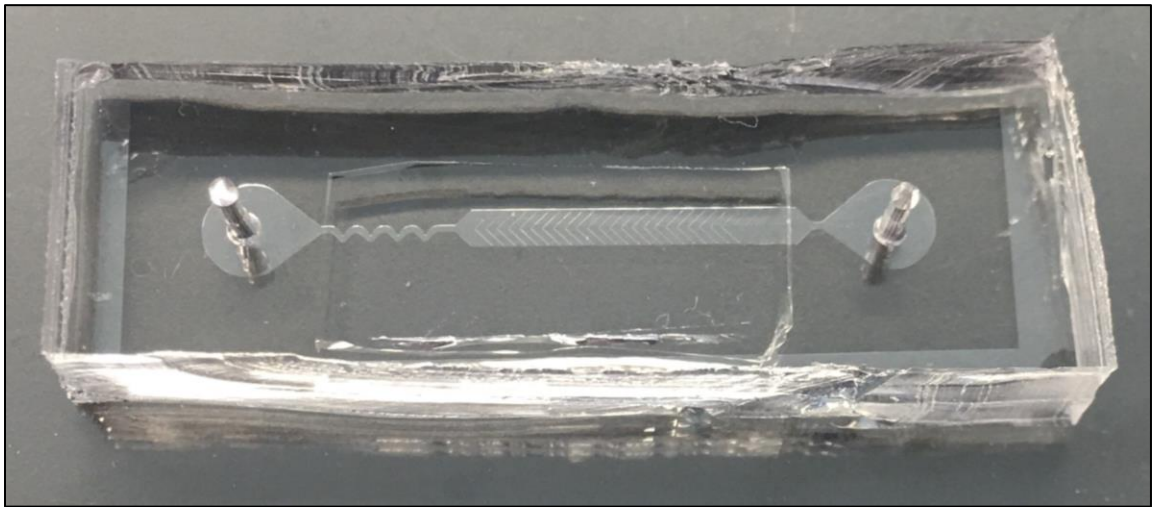
Figure A. 2: Glass-reinforced PDMS device. Example image of a PDMS device with glass reinforcement. A small glass slide has been cut to fit the device layout, so that it covers the channel and ridges without impinging on the inlet and outlet regions. The small glass slide is embedded inside the PDMS, just above the channel features. The device has been bonded to a glass slide.

Experiment Preparation (Complete before experiment)

1. Cell flow buffer recipe:

    a. 30 mL PBS (-/-) + 40 mg BSA + 1.6 mg EDTA (11 uL of 0.5M stock) + 10 mL Percoll.

    b. Filter the buffer with sterile filter (0.2 μm), store in fridge.

    c. Flow buffer is optional, can use PBS, media, Opti-MEM, etc.

2. Passivate devices and syringe/needle with 1% BSA in DI water (sterile filtered).

    a. Flush dust out of all needles and tubing using EtOH and DI water.

    b. To plug needles into the microfluidic chip, carefully align the needle with the opening and guide it into the punches using gentle pressure. Do not force the needle, as this can damage the PDMS punch.

    c. Flow 1% BSA through device using syringe, leave extra BSA in needle.

    d. If passivating devices overnight, store the devices in the fridge and cover the inlets and outlets with tape

    e. If using the devices the same day, passivate at room temperature for >20mins. Tape is not necessary, but leave a large droplet of 1% BSA at the outlets to prevent the channel from drying out.

    f. Prep at least twice as many devices as you will need in case of device unbonding or leaking.

Experiment Setup

1. Pump

    g. Set syringe diameter on pump (Harvard apparatus syringe selection guide).

    h. Program the syringe pump to the desired flow rate.

    i. Experiments that require tubing can sometimes result in cell loss due to cells settling at low points in the tubing. To prevent this, position the syringe pump above the device, and position the tubing so that it follows a consistent downward path toward the device, as pictured in Figure A. 3.
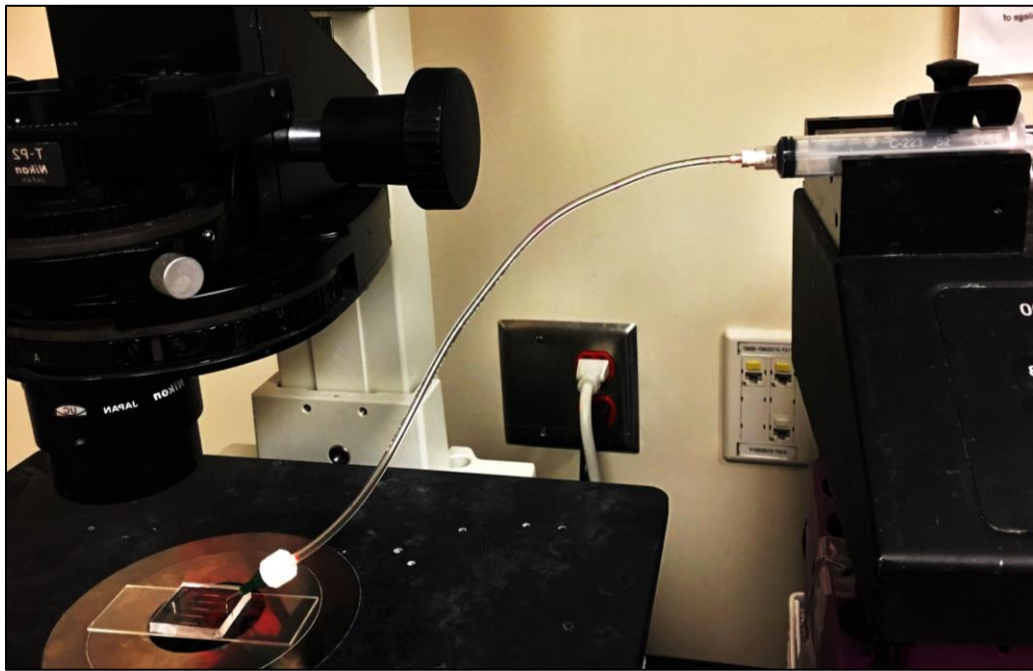
Figure A. 3: Syringe pump setup relative to microfluidic device. To prevent cell settling at low points in the tubing, elevate the syringe pump above the device. Position the tubing so that the path that the cells take from the syringe to the device is consistently downhill, so that there are no local low points at which cells can settle.

2. Microscope

    a. Place device on microscope stage to observe cell flow if desired.

    b. Make sure light is off throughout collection of photo-sensitive samples.

3. Prime the tubing and needles by flowing through 1% BSA or buffer until a liquid droplet forms at the tip of the needle, tapping to remove all bubbles.

4. Leave a large drop of 1% BSA at inlet so needle will have a liquid-liquid interface.

5. If necessary, flow additional 1% BSA or buffer through device immediately before use to remove all bubbles.

6. Prep buffer:

    a. Add 0.3 mg/mL FITC-dextran or other desired amounts or types of reagents directly to cell flow buffer.

7. Prep cells:

    a. Complete all other prep first to minimize time cells are out of culture.

    b. Thoroughly resuspend cells in cell flow buffer with molecules by pipetting repeatedly.

    c. Pass cell suspension through cell strainer (>2X larger than cell diameter)

    d. Dilute cells to proper concentration (~1-10 x 10^6 cells/mL buffer)

    e. To prevent cell viability loss during longer experiments (≥ 1 hour), store cells on ice until ready to use.

Experiment Run

1. Load cells into the syringe.

    a. Eject any remaining 1% BSA from syringe, tubing, and needle.

    b. Uptake cells into syringe and tap to remove all bubbles from syringe, tubing, and needle.

    c. For photosensitive experiments, cover the syringe and tubing with foil.

d. Load the syringe into the syringe pump.

e. To prevent cell viability loss during longer experiments (≥ 1 hour), tape a small cold pack onto the syringe.

2. Ensure needle is fully primed with cell solution, then attach to cell syringe inlet.

3. Keep samples on ice until experiment is complete.

4. If using a microscope, observe that cells are flowing through the microchannel without major clogs or bubbles.

a. For photosensitive experiments, turn off microscopy light during sample collection.

5. When experiment is fully operational, collect fluid from outlets using pipets.

a. Can save effort by plugging pipet tips into outlets, as shown in Figure A. 4.
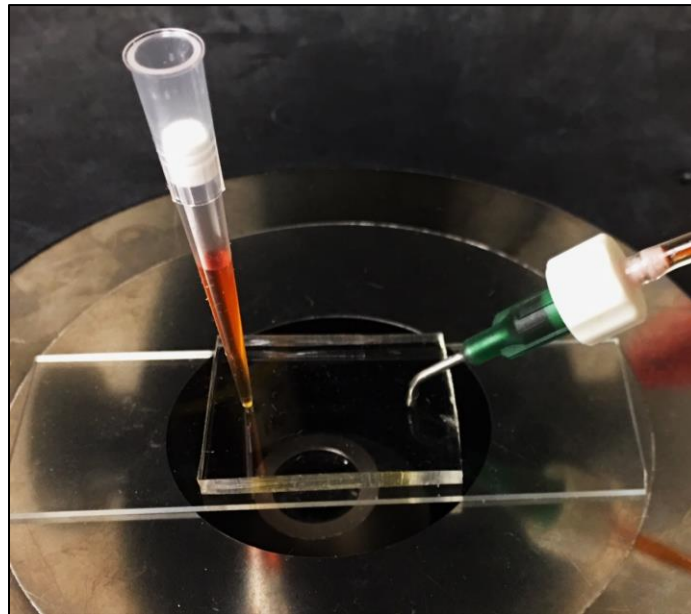
Figure A. 4: Microfluidic device setup on microscope stage. Typical setup image of a single-inlet, single-outlet microfluidic device on a microscope stage. The needle is attached to tubing and is plugged into the inlet. A pipet tip is plugged into the outlet to collect the sample (orange fluid).

A.1.4   Cell VECT Sterile Transfection Protocol

1. Autoclave microfluidic devices, needles, and syringes in sterilization pouches.

    a.   Allow to fully cool before use.

2. If working with nucleic acids that are sensitive to degradation, clean the BSC work surface with RNase AWAY decontamination reagent.

3. Use sterile syringe and needle to passivate devices with sterile 1% BSA in DI water.

    a.   Make sure syringe, needle, and device are free of bubbles.

    b.   Passivate at RT for >20 mins in BSC.

    c.   Flush devices with sterile PBS (-/-) after passivation, leaving a large droplet at the inlet to prevent the channel from drying out.

4. Plug sterile pipet tip into device outlet for sample collection.

5. Spin down cells and wash once with PBS (-/-).

6. Resuspend cells at $1\text{-}10\text{x}10^6$ cells/mL in serum-free media (Opti-MEM).

7. (Optional) pass cell suspension through a sterile cell strainer (>2X larger than cells) to remove aggregates.

8. Add transfection payload at desired concentration to cell-media suspension.

9. Load cells into sterile syringe with needle.

10. Prime the needle by gently pushing the syringe plunger until a very small droplet of cell suspension forms at the tip of the needle.

11. Plug the primed needle into the device inlet.

    a.   Guide the needle into the inlet punch using gentle pressure. Forcing the needle could damage the PDMS inlet punch,

b. The primed needle should form a liquid-liquid interface with the droplet at the inlet, which prevents air from entering the channel.

12. Flow cells through device using a syringe pump.

a. Syringe pump should be cleaned with ethanol, then placed in the BSC.

b. To minimize reagent waste and void volume in the setup, attach the needle directly to the syringe and plug the needle directly into the device inlet, as shown in Figure A. 5.

c. Cells will collect at the sterile pipette tip. A barrier pipette tip can be used for sample collection to minimize contamination.

Figure A. 5: Sterile microfluidic device setup in BSC. Example setup for sterile microfluidic device operation in a biosafety cabinet. This setup utilizes a needle attached directly to the syringe without tubing to minimize void volume and reagent waste. The device is elevated so that the needle can plug directly into the inlet without tubing. A barrier pipette tip is plugged into the outlet to collect the cell sample and minimize contamination risk.

13. Rest cells, undiluted, for 10 minutes after processing.

14. Gently plate cells in pre-warmed culture media at desired culture density.

A.2   Evolution of Device Design

Over the course of this thesis work, the cell VECT microfluidic device design has undergone several rounds of revisions that were informed by experimental findings. These changes were made to improve intracellular delivery efficacy, simplify device use and setup, and increase cell throughput. Numerous design changes have been made to various aspects of the device design, including the number of inlets, outlets, and channels, and the geometry of the channels and ridges. The device design initially used for cell VECT experiments had originally been developed for cell sorting based on mechanical properties [1-3]. This design had three inlets: one cell inlet flanked by two sheath inlets to focus the cell flow down the center of the microfluidic channel. The design had a single microfluidic channel and multiple outlets to facilitate fractionation of the inlet cell population into multiple outlet subpopulations (Figure A. 6A). The ridges had a diagonal orientation for directed cell deflection along the slant based on mechanical properties [1-3].

As a result of several device iterations, various device design changes have been made. To simplify device use and setup, the device design was modified to utilize only one inlet and one outlet. Removing the sheath inlets simplified device setup and reduced reagent waste, since the sheaths inlets needed to contain the same concentration of target molecules as the cell inlet. The sheath focusing was replaced by serpentine inlet channels designed to focus cell flow to the center of the ridged microchannel [4,5]. The ridges were modified from a diagonal geometry to chevrons that focus cells to the center of the ridge field to further facilitate cell processing through the ridges without sheath focusing. These changes helped to improve delivery efficiency. To increase cell throughput on a single microfluidic chip, a manifold with multiplexed channels was added, such that several

157

microfluidic processing channels could operate from a single cell inlet. This multiplexed

processing was facilitated by the removal of the multiple cell outlets. The overall product

of these design changes can be visualized in Figure A. 6B. These design changes have

increased the throughput of a single microfluidic chip from ~10^4 cells/min in the original

design to up to and exceeding 10^7 cells/min in the new manifold devices. The throughput

of a single chip can easily be increased further by multiplexing the device microchannels

in 2 dimensions, with an increased number of microchannels side-by-side, or in 3

dimensions by stacking multichannel devices on top of each other or creating 3-

dimensional multiplexed processing channels through injection molding. The

simplification of the microfluidic setup due to the removal of unnecessary inlets and outlets

is shown in Figure A. 6C,D.
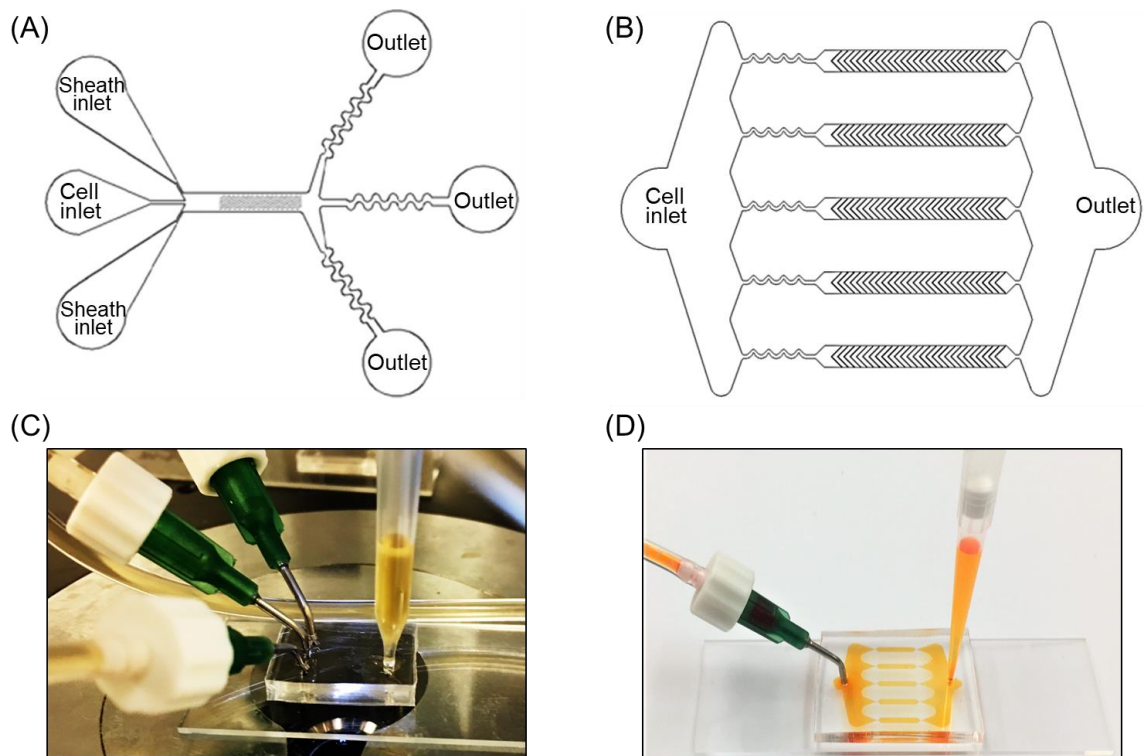
Figure A. 6: Evolution of a device. (A) Initial experiments were carried out on a microfluidic device originally designed for cell sorting. This design used multiple inlets

for sheath focusing and multiple outlets for cell fractionation. The device has a single processing channel with diagonal ridges. (B) An evolved device design exhibiting the results of several design revisions. The sheath focusing inlets were replaced with serpentine focusing channels and chevron focusing ridges. The multiple outlets were consolidated into a single outlet. The single inlet and outlet facilitates multiplexing of the channels for higher throughput. (C) Operation of the original design requries additional setup due to the multiple inlets and outlets. (D) The removal of unnecessary additional inlets and outlets simplifies the setup and operation of the new device design.

Many of the design changes were informed by experimental results that elucidated the mechanism and governing parameters of cell VECT delivery. Since faster cell compression was shown to increase cell volume loss and improve intracellular delivery, we increased the flow rates at which the devices are operated [7]. At high flow rates, the flexible PDMS microchannel can deform due to internal fluid pressure, which can change the channel height. We analyzed PDMS microchannel deformation using extra-fine microscope objective focusing on the beginning of the ridge field, where deformation would be highest [8,9]. Our microfluidic cell volume change experiments were conducted at flow rates in which deformation of the PDMS microchannel and ridges was not detectable (<1 μm). In order to maximize intracellular delivery through rapid compression, we utilize the devices at higher flow rates with the addition of glass slide reinforcement, which has been shown to significantly minimize pressure-induced PDMS microchannel deformation (Figure A. 7) [10,11]. At the highest operating flow rates in our glass-reinforced devices (800 μL/min) deformation of the PDMS microchannel and ridges was not detectable (<1 μm).

Since results showed that repeated compressions resulted in greater intracellular delivery, the number of ridges on subsequent device designs was increased to >22 to maximize delivery (Figure A. 7) [6]. We also increased the spacing between ridges to

facilitate cell relaxation between compressions, which was shown to increase delivery (Figure A. 7) [6]. Smaller compression ridge gaps were used to increase volume loss and improve delivery (Figure A. 7) [6]. The faster flow rates also enabled the devices to operate with a smaller compression ridge gap, ≤50% of cell diameter, without cells flowing around the ridges or clogging the ridges. However, we refrained from using ridge gap sizes <20% of cell diameter; we observed that cells that are rapidly forced through a compression ridge gap that is too small (<20% of cell diameter) had lowered viability. Some cells also undergo lysis at these extreme compression conditions, which can cause clogging of the ridges due to cell debris. The clogged channel lowers cell throughput, processing efficiency, and cell recovery. Therefore, to avoid these adverse impacts on cell processing, we used compression ridge gaps >25% of cell diameter. We also filter out potential clogging agents, such as dust and nonviable cell aggregates, using a cell strainer with pore diameter that is ~2X the size or greater than that of the average cell diameter. Overall, our device design and protocol changes were informed by experimental studies into the governing parameters of cell VECT in order to maximize delivery efficiency and throughput.
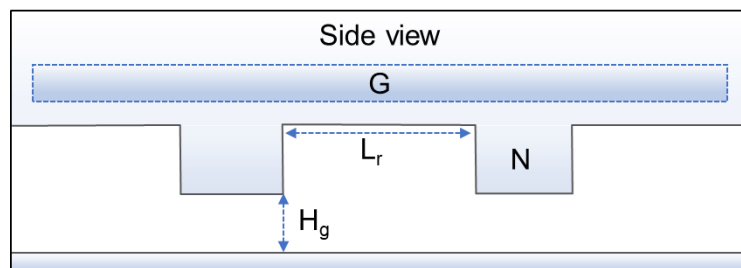

Figure A. 7: Schematic of device design features to improve intracellular delivery. The compression ridge gap height (H_g) is decreased to ≤50% of cell diameter. The distance between ridges (L_r) is increased to facilitate cell recovery between ridges. The number of ridges (N) is increased to > 22 to improve delivery. The presence of a glass slide (G) is added to facilitate higher flow rate, and therefore faster compression, without PDMS channel deformation.

Multiple design changes were developed in conjunction with the single-inlet device design in order to facilitate high cell processing efficiency. The single-inlet devices no longer have the sheath focusing flows from the sheath inlets, and therefore cell flow is not focused through the ridged microchannel (Figure A. 8A). Therefore, we introduced additional design features, serpentine focusing and smaller ridge gutters, to compensate for the lack of sheath focusing (Figure A. 8B). In the unfocused devices, we observed ~20% of cells flowing in the gutter region of the device (Figure A. 8C). The gutter region, the space at the outer edges of the microchannel past the ends of the ridges (shown in red in Figure A. 8C,D), is intended only to provide an escape mechanism for dead cells and cell aggregates that would normally clog the device, but in the unfocused devices result in a significant portion of viable cells flowing around the ridges without being processed. To mitigate this effect, we reduced the size of the gutters by half or more, and introduced a serpentine channel following the inlet that focuses the cell flow through the center of the microchannel [4,5]. These design features reduced the percent of cells in the ridge gutter by over half (Figure A. 8D). An overview of device design changes and the reasoning behind them is described in Table A. 1.
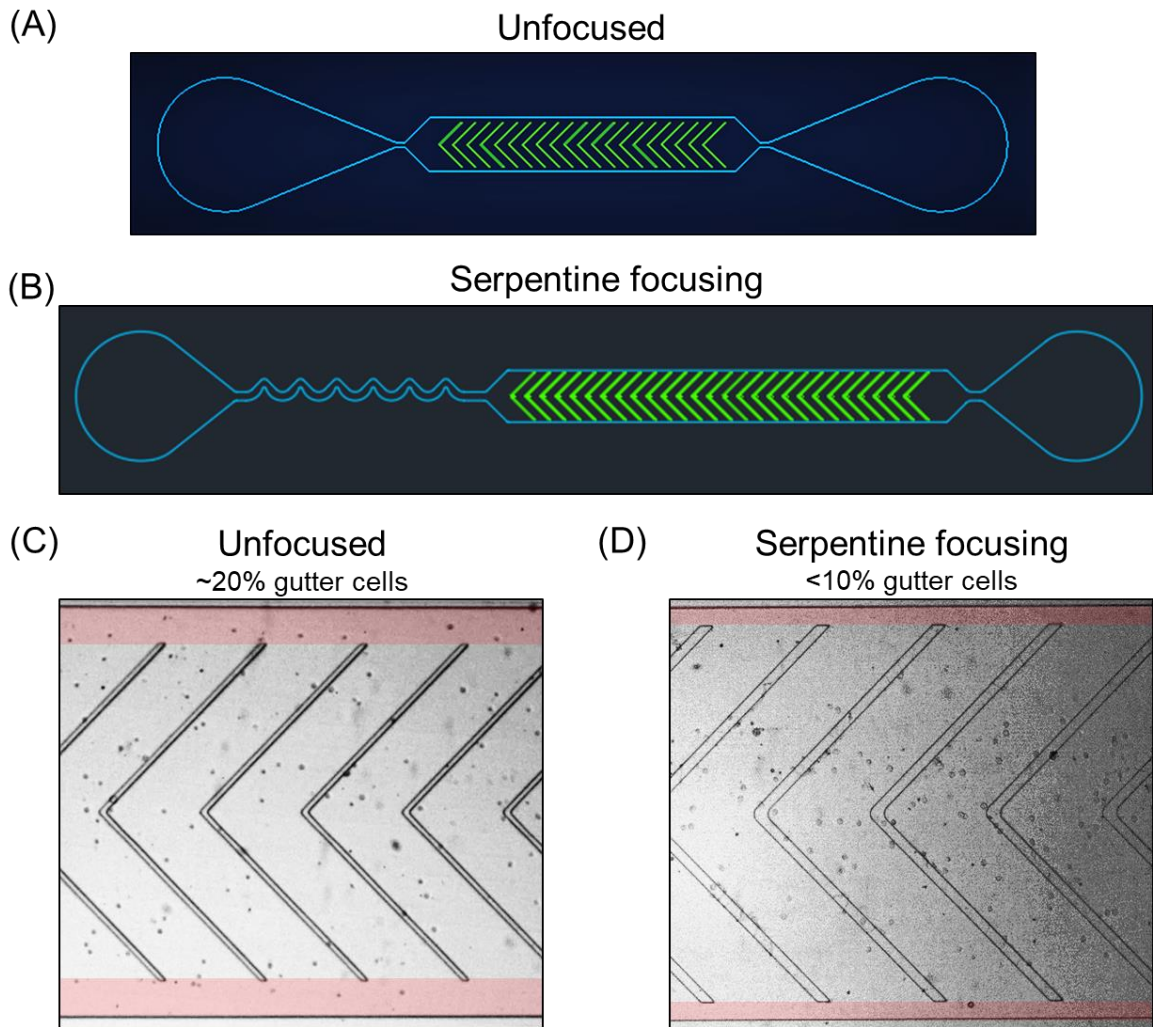
Figure A. 8: Device design features to minimize gutter cells. (A) Removal of the sheath inlets resulted in an unfocused, single-inlet device design. (B) Introducing a serpentine channel after the inlet allows for cell flow focusing in a single-inlet device. (C) In the unfocused device design, approximately 20% of cells go unprocessed by flowing around the ridges in the gutter region (red) of the microchannel. (D) In the serpentine focusing device with 50% smaller gutters, the percent of cells in the gutter region (red) is reduced by over half.

Original design	New design	Reason for change	Impact on processing
Sheath inlets	No sheaths, 1 inlet	Sheaths require more setup, waste reagents	80% reduction in reagent usage
Diagonal ridges	Chevron ridges	Chevron ridges focus cells to center of ridges without sheaths	Enables design to be used without sheaths
Non-serpentine inlets	Serpentine inlets	Focuses cell flow to center of channel before entering ridges	Enables design to be used without sheaths
1 channel	Multiple channels	Multiplexed channels increase throughput	>5-fold increase in throughput
Multiple outlets	1 outlet	Multiple outlets complicate collection step	More efficient cell collection, especially for multiple channels
PDMS device	Glass-reinforced PDMS	Enables faster flow rates without channel deformation	>4-fold increase in flow rate, throughput
Compression gap 40-80% of cell diameter	Compression gap ≤50% of cell diameter	Smaller compression gap results in greater volume change	Increased delivery with smaller gaps
Number of ridges: 7 – 27	Number of ridges: >22	More ridges results in more cell compressions	Devices have sufficient ridges to achieve maximum delivery
100 µm spacing between ridges	≥ 200 µm spacing between ridges	Increased cell recovery time between ridges	Cells recover volume between ridges even at high flow rate
Ridge gutter: 100 µm	Ridge gutter: 50 µm	Lower the number of unprocessed cells in the gutter	Cells in the gutter reduced from ~20% to <10%

Table A. 1: Summary of microfluidic design changes and rationales.

A.3 References

[1]   Wang, G. *et al.* Microfluidic cellular enrichment and separation through differences in viscoelastic deformation. *Lab Chip.* **15**, 532-540, doi:10.1039/c4lc01150c (2015).

[2]   Wang, G. *et al.* Stiffness dependent separation of cells in a microfluidic device. *PLoS One.* **8**, e75901, doi:10.1371/journal.pone.0075901 (2013).

[3]   Wang, G., Turbyfield, C., Crawford, K., Alexeev, A. & Sulchek, T. Cellular enrichment through microfluidic fractionation based on cell biomechanical properties. *Microfluid. Nanofluid.* **19**, 987-993, doi:10.1007/s10404-015-1608-y (2015).

[4]   Oakey, J. *et al.* Particle Focusing in Staged Inertial Microfluidic Devices for Flow Cytometry. *Anal Chem.* **82**, 3862-3867, doi:10.1021/ac100387b (2010).

[5]   Zhang, J., Li, W. H., Li, M., Alici, G. & Nguyen, N. T. Particle inertial focusing and its mechanism in a serpentine microchannel. *Microfluid. Nanofluid.* **17**, 305-316, doi:10.1007/s10404-013-1306-6 (2014).

[6]   Liu, A. *et al.* Microfluidic generation of transient cell volume exchange for convectively driven intracellular delivery of large macromolecules. *Mater. Today.* **21**, 703-712, doi:10.1016/j.mattod.2018.03.002 (2018).

[7]   Liu, A. *et al.* Cell Mechanical and Physiological Behavior in the Regime of Rapid Mechanical Compressions that Lead to Cell Volume Change. *Small.* e1903857, doi:10.1002/smll.201903857 (2019).

[8]   Hardy, B. S., Uechi, K., Zhen, J. & Pirouz Kavehpour, H. The deformation of flexible PDMS microchannels under a pressure driven flow. *Lab Chip.* **9**, 935-938, doi:10.1039/b813061b (2009).

[9]   Gervais, T., El-Ali, J., Gunther, A. & Jensen, K. F. Flow-induced deformation of shallow microfluidic channels. *Lab Chip.* **6**, 500-507, doi:10.1039/b513524a (2006).

[10]   Inglis, D. W. A method for reducing pressure-induced deformation in silicone microfluidics. *Biomicrofluidics.* **4**, doi:10.1063/1.3431715 (2010).

[11]   Plecis, A. & Chen, Y. Fabrication of microfluidic devices based on glass–PDMS–glass technology. *Microelectronic Engineering.* **84**, 1265-1269, doi:https://doi.org/10.1016/j.mee.2007.01.276 (2007).